UNIVERSITÀ DEGLI STUDI DI MILANO

DEPARTMENT OF PHYSICS

PHD SCHOOL IN
PHYSICS, ASTROPHYSICS AND APPLIED PHYSICS
CYCLE XXXIV

The study of the influence of the microenvironment of healthy and tumoral cells by Atomic Force Microscopy

Disciplinary Scientific Sector FIS/03

PhD Thesis of:
Hatice Holuigue

Director of the School: Prof. Matteo Paris
Supervisor of the Thesis: Prof. Alessandro Podestà
Co-Supervisor: Dr. Matteo Chighizola

A.Y. 2022-2023

External referees:

Dr. Ioanna Mela,
Department of Chemical Engineering and Biotechnology,
University of Cambridge, Cambridge, UK

Dr. Sebastien Janel,
Unit of Cellular Microbiology and Physics of Infection,
CNRS, Lille, France

Commission of the final examination:

Prof. Malgorzata Lekka,
Full Professor at the Department of Biophysical Microstructure at the Institute of Nuclear Physics, Polish Academy of Science (IFJ PAN, Kraków, Poland)

Prof. Felix Rico,
Associate Professor at Université Aix-Marseille and INSERM (Institut National de la Santé et de la Recherche Médicale), Force Microscopy Lab, Marseille, France

Internal Member:

Prof. Alessandro Podestà,
Professore associato presso il Dipartimento di Fisica “Aldo Pontremoli”,
Università degli Studi di Milano

Final examination:

Monday 13th March 2023
Dipartimento di Fisica, Università degli Studi di Milano
Milano, Italy

Phys2BioMed project has received funding from the European Union's Horizon 2020 research and innovation programme under the Marie Skłodowska-Curie grant agreement N° 812772.

Non est ad astra mollis e terris via
- Seneca

1. Introduction

1.1. Cells and their microenvironment

The cell is known as the fundamental unit of life, together with the extracellular matrix (ECM), they constitute together the tissues of our bodies, as shown in **Figure 1** [1]. ECM, a 3D highly dynamic network, is the scaffold of the cellular component of tissues, mainly composed of macromolecules such as proteoglycans and fibrous ones: collagen, elastin, fibronectin, and laminins [1–3]. The first one, collagen is the most abundant of these fibrous extracellular proteins in animal tissues, they bind to each other side by side creating long collagen fibrils. Fibronectin is a protein made of two dimers that bind to the cells' integrins mostly via their Arg-Gly-Asp RGD sequence. And finally, laminins, the major component of the basement membrane, are composed of three different chains α, β and γ, it has been proven to play a role in cell differentiation, migration, and adhesion [2,4–6]. The ECM is organ-specific and has a crucial role in many cellular processes including growth, migration, differentiation, survival, homeostasis, and morphogenesis [3,6,7].

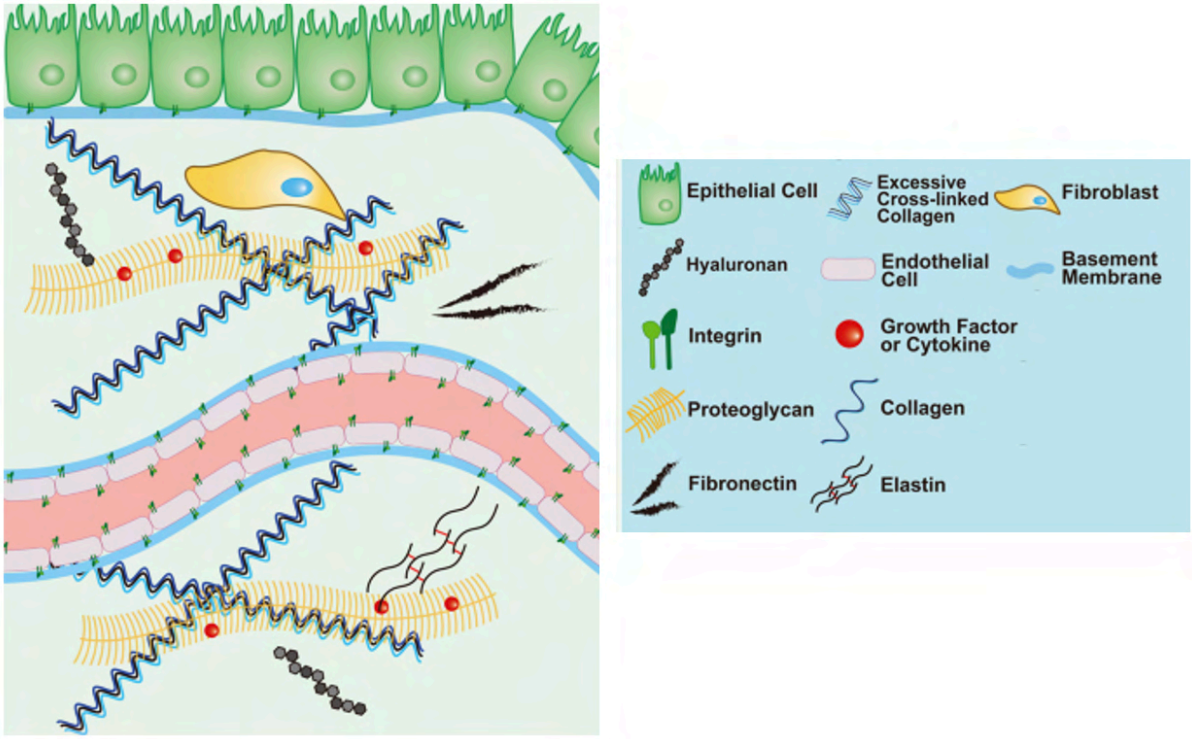

Figure 1. Schematic of the extracellular matrix and its components. Adapted from Huang et al.[8]

Cells are embedded into the ECM via their surface receptors considered as the primary transmembrane molecule [9], the integrins. Those integrins bind to the receptors of matrix proteins like fibronectin laminin and collagen [6,9] and are composed of α and β heterodimers; they are able to both transmit and detect changes in mechanical force on the ECM as they are connected directly to the cell's actin cytoskeleton [9,10]. The cytoskeleton is composed of three

sub-structures: the actin filaments (made of f-actin), the microtubules MT and the intermediate filaments, as presented in **Figure 2**.

It is then evident the role of integrins in the regulation of many vital functions of the cells such as cell spreading, growth, proliferation, and differentiation [9–11]. Every combination of α and β dimers of integrins specifically connects to an ECM protein [10,11], as presented in **Figure 3.**

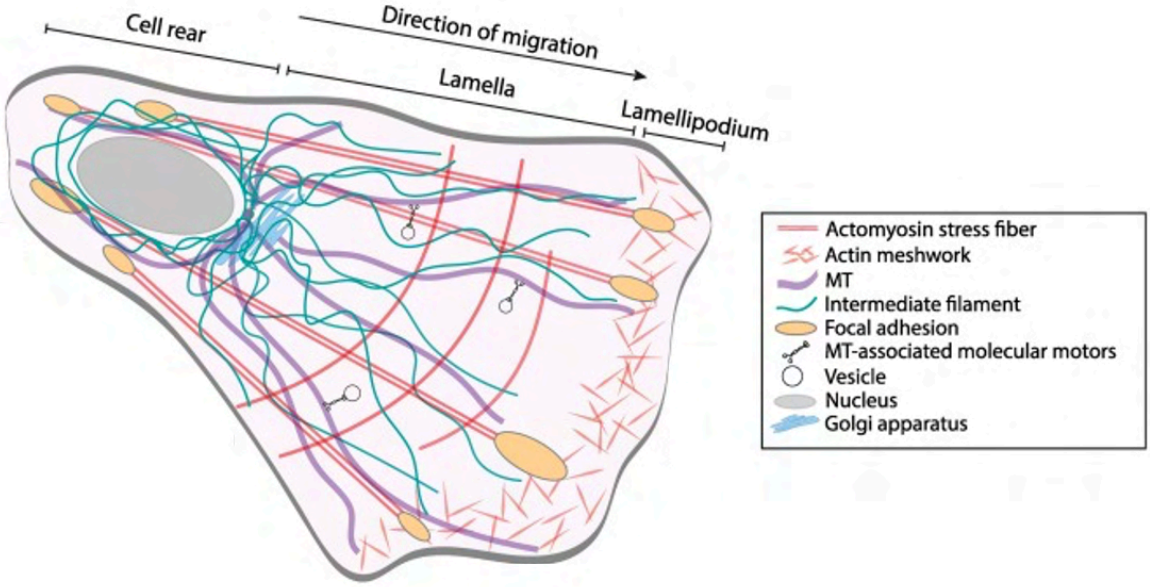

Figure 2. Representation of the cell's cytoskeleton, adapted from S. Seetharaman et al. 12

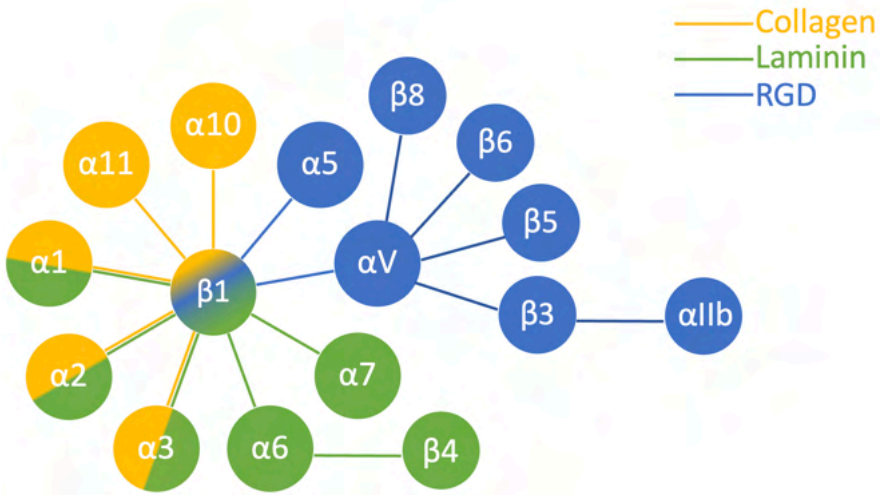

Figure 3. Scheme of the possible combination (represented by the line) between and α and β sub-units of the human integrins for laminin, collagen and RGD domains binding 11.

Cell's microenvironment not only consists of the extracellular matrix but include also neighbouring cells; the interaction of the cells with their peers contributes to a wide variety of processes: embryonic development, wound healing but also tumour progression and metastasis [1,13,14].

Cell junctions are regulated by cadherins, as presented in **Figure 4**, which link one cell to another via homophilic (same cells) or heterophilic binding (different cell, often weaker than

its counterpart). There is a huge variety of cadherins, the classical ones being E-cadherin, P-cadherin and N-cadherin [1]. Cadherin bonds are mainly mediated by linker proteins called catenin, who transmit signals to the cytoskeleton. E-cadherins, mostly present on epithelial-type cells, are the main molecules in charge of the maintenance of the epithelial differentiation and integrity of basal layers [13]. P-Cadherins are found in basal and lower layers of epithelium, while the N-Cadherins is in general specific to motile cells like neuronal and fibroblast [13].

There is a need to understand how cells communicate, understand, and process all the stimuli received from their microenvironment. It is through those connections, that the cells sense and respond in a comprehensive manner: this is mechanotransduction.

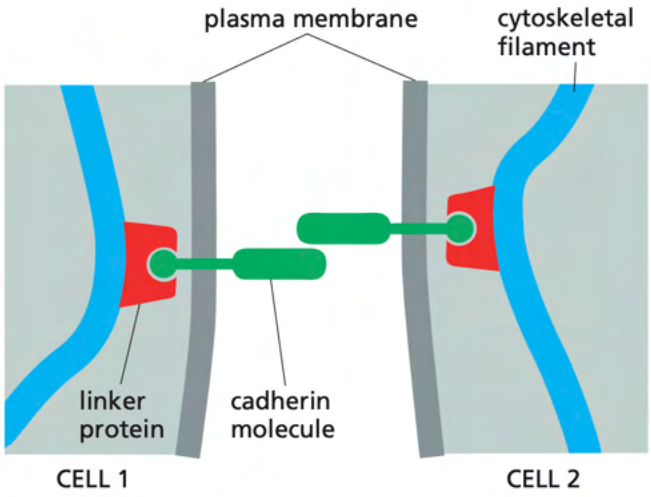

Figure 4. Schematic of cadherins binding between cells, adapted from Essential cell biology [1].

1.2. Mechanotransduction

Mechanobiology describes generally how molecules organize themselves in tissues and cells, generate or are being affected by external forces. They are interwoven and have an impact on one another[15]. Mechanotransduction is the particular process by which the physical (mostly mechanical) properties of the surrounding microenvironment are perceived by the cells and converted into mechanical, biochemical and/or electrochemical activity, inducing intracellular changes via the cytoskeleton remodelling and activation of signalling pathways [15–17].

At the base of the connection between the cell and the matrix, there is the activation of the integrins that happen during the binding of both FERM–domain protein talin and kindlin to the β subunit of the integrins. This binding induces a conformation change from closed-bent to active-open of the integrins [16,18], as presented in **Figure 5**. Integrins are then linked to the actin cytoskeleton of the cells via so-called adaptor proteins (i.e., talin and vinculin).

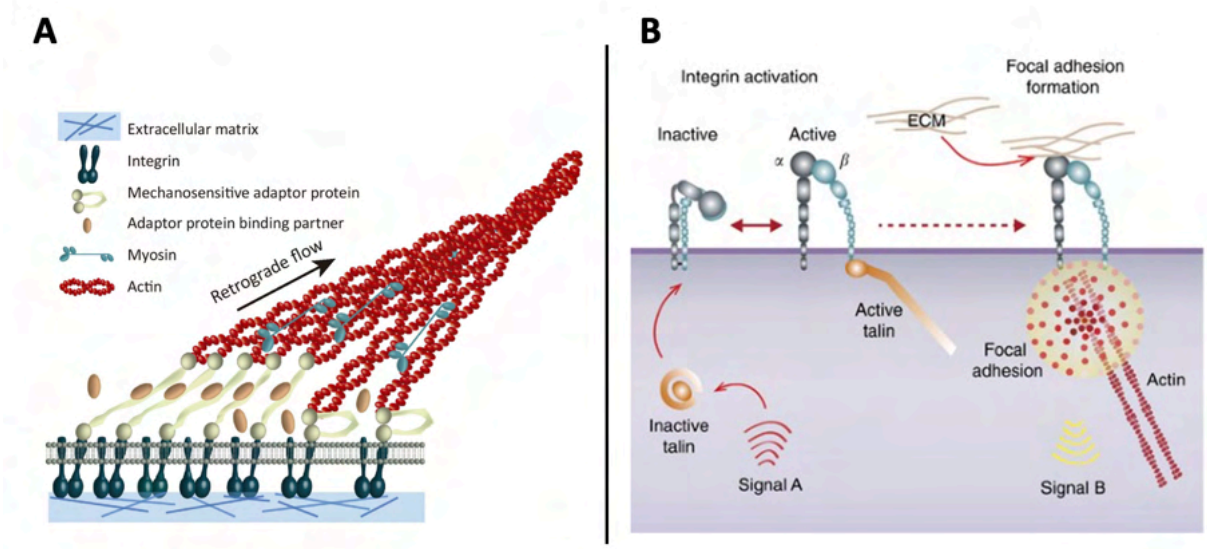

Figure 5. (A) Representation of the molecular clutch and retrograde flow, adapted from Elosegui et al. [19] . (B) Integrin activation process and focal adhesion formation: an internal signal A activates the integrin, to then form focal adhesion with ECM. The whole cell-ECM complex subsequently transmits direct signal, signal B, to the cell through its cytoskeleton. Adapted from Hamidi et al. [18].

The interconnected complex of matrix, integrins and actin filament drives the cells during its migration by actin polymerization and actomyosin contraction in a process called the "retrograde actin flow" (**Figure 5A**). This molecular clutch, representative of the ECM-cells' cytoskeleton system, is highly tuneable and dynamic, it senses the stiffness of the ECM and responds accordingly by converting the retrograde movement of the actin into a protrusive force [19].

The integrin adhesion complexes (IAC) are the connections for the detection of external mechanical stimuli; these integrin transmembrane complexes are the bridge between the ECM and the cytoskeleton. Different form of IAC exists: Nascent adhesion, which could then transform into focal adhesions (FA) via integrin clustering. Their attachment reinforcement is driven by the force of the molecular clutch in response to external stimuli [17,20], controlled for example by ECM rigidity (**Figure 6A**) or binding site densities [7,19] (**Figure 6B**). It has been demonstrated that a more rigid substrate induced stronger transmission forces and loading [19]. In the case of fibroblasts, FA can then further evolve into fibrillar adhesion and be able to remodel and synthesize the ECM. It is nowadays quite clear that integrin primary function of is to mediate mechanical signalling [9,21].

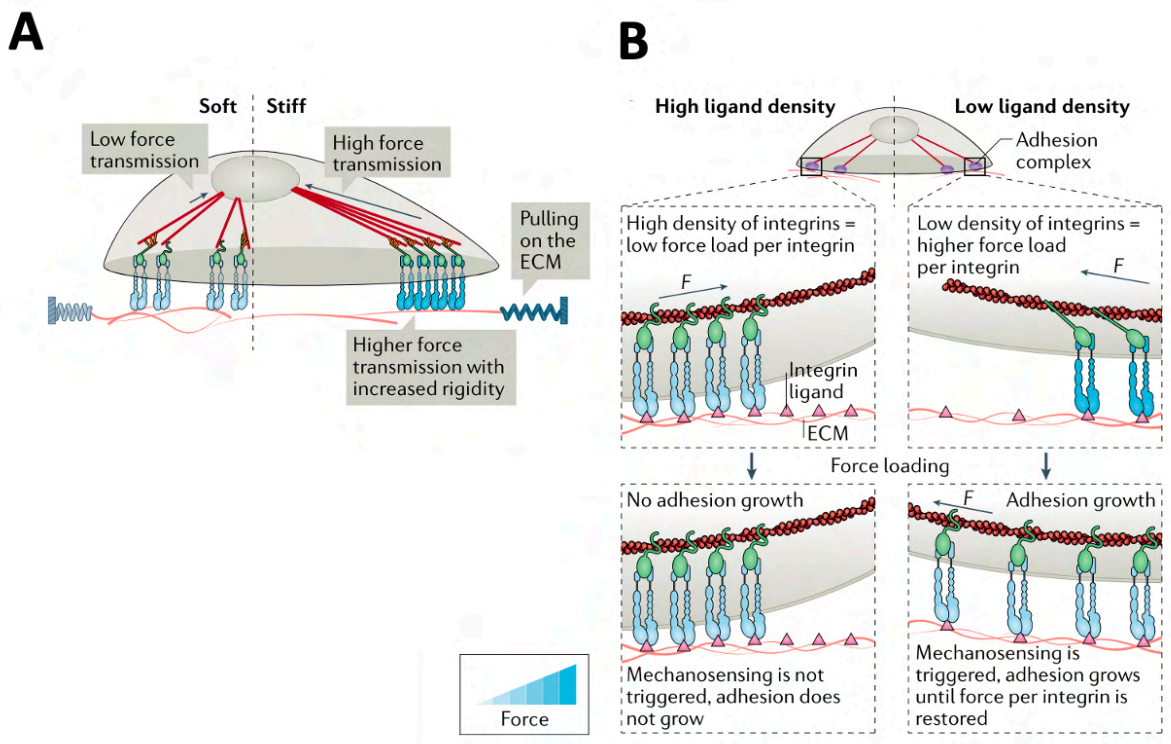

Figure 6. Response of the integrins to (A) the rigidity and (B) ligand density of the ECM. Adapted from Kechagia et al. [9].

Looking even closer at the cell-ECM interface, we can identify another role player: the glycocalyx, a surface brush layer attached to the cell's surface made of glycoproteins, proteoglycans, and polysaccharides [1,22]. The role of the glycocalyx in mechanotransduction is not well understood, nevertheless, it is considered a promoter of integrin clustering acting as a kinetic trap [23,24] (**Figure 7**). Glycocalyx have been used also both as a potential biomarker and therapeutic target in cancer; in fact, tumoral cells showed bulky glycocalyx' composition [25] compared to normal ones, indicating that glycocalyx composition could potentially favour metastatic spreading [26,27].

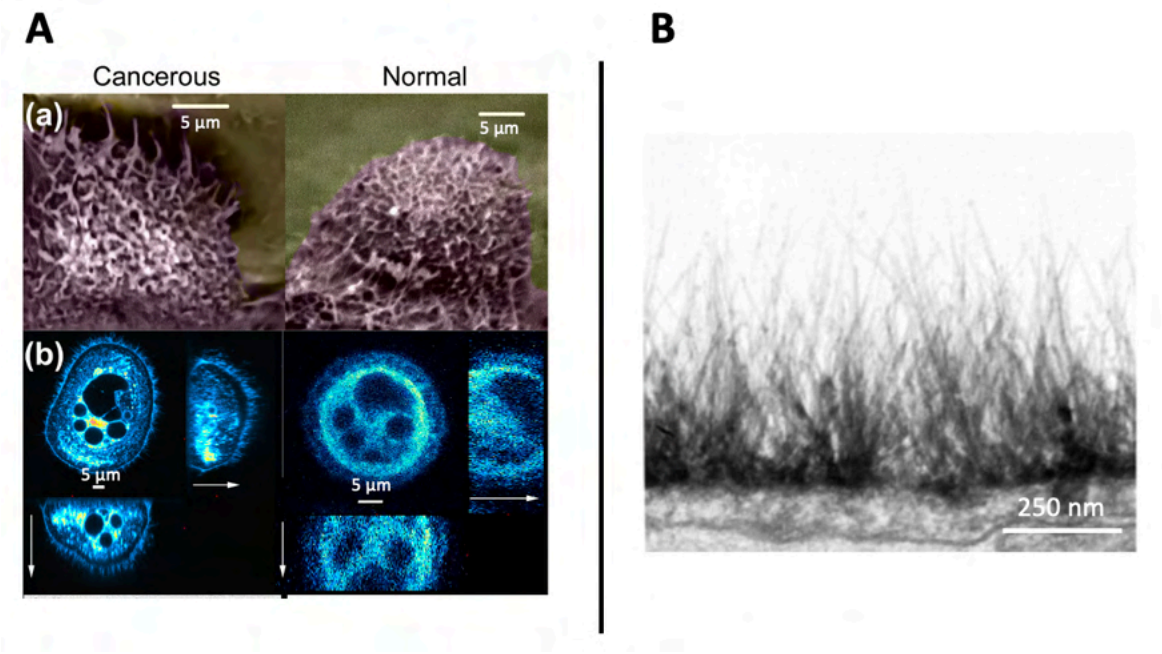

Figure 7. (A) Visualization of brush by scanning electron microscopy of (a) cancerous and normal cell. Colors are artificial. (b) Confocal images of the cells with their glycocalyx brush with their 3D cross-section. Adapted from Iyer et al. [25]. (B) Detailed of electron microscopic overview of the glycocalyx a rat left ventricular myocardia. Adapted from Van den Berg et al.[28].

Mechanotransduction allows us to appreciate the most prominent feature of the cell-ECM interaction i.e., it is reciprocal, one player influencing the other and vice versa. Therefore, more efforts are needed to understand their inter-communication and the study of each entity one by one but also of all entities as a whole. Alteration of ECM rigidity, and hence, mechanotransduction processes can be associated with physiological processes but also cancer, as described in the next section.

1.3. Cells-microenvironment interaction in cancer disease

Cancer, coming from ancient Greek karkínos (“crab”), is a generic term for a disease that describes the transformation of normal cells to tumoral cells that colonizes a secondary site and metastases.

Normal cells are regulated by a strict cell cycle that controls their proliferation, growth, and death. On the contrary tumoral cells are abnormal functioning cells, that have an altered mechanism through genome instability, acquiring resistance to apoptosis as well as uncontrolled proliferation [29–31]. Benign tumours are non-invasive, while malignancy characterizes the ones that break the basement membrane. Metastasis cells are involved in the spreading of tumours via migration and invasion of other tissues and organs (**Figure 8**) [31].

While in theory, the overall process of cancer is simple: initiation of the mutation, proliferation, survival, tissue invasion and metastasis, a deep understanding of the fine mechanisms remains challenging: in fact, cancer is nowadays the leading cause of death worldwide [32].

Into the defined hallmarks of cancer [29,30] the cell-microenvironment interaction represents a key element. As an example, during Epithelial to Mesenchymal Transition (EMT), cells become more mobile and as a primary tumour, invades adjacent tissues, colonizing secondary sites and forming metastases (**Figure 8**). This whole process is mainly induced by growth factors such as TGF-β1[33]. One of the most notable changes during that transition is in cell-cell junctions, the so-called "cadherins switch" [34]: the downregulation of E-cadherin function by TGF-β1 is compensated by the upregulation of the N-cadherins. The cadherin switch is an indicator of an ongoing EMT and development of various cancer [13,14,35–37], often associated with more aggressive and less differentiated cells that gain in migratory capacity, resistance to apoptosis, and invasiveness [38].

During the colonization of the second site, the reverse process is observed: Mesenchymal to Epithelial transition (MET) [39]. Those mechanisms require changes in the cells' interaction with their microenvironment [40,41], the affected proteins include cell adhesion molecules (CAMs) that regulate cell-cell communication via cadherins but also cell-ECM interaction with integrins [34].

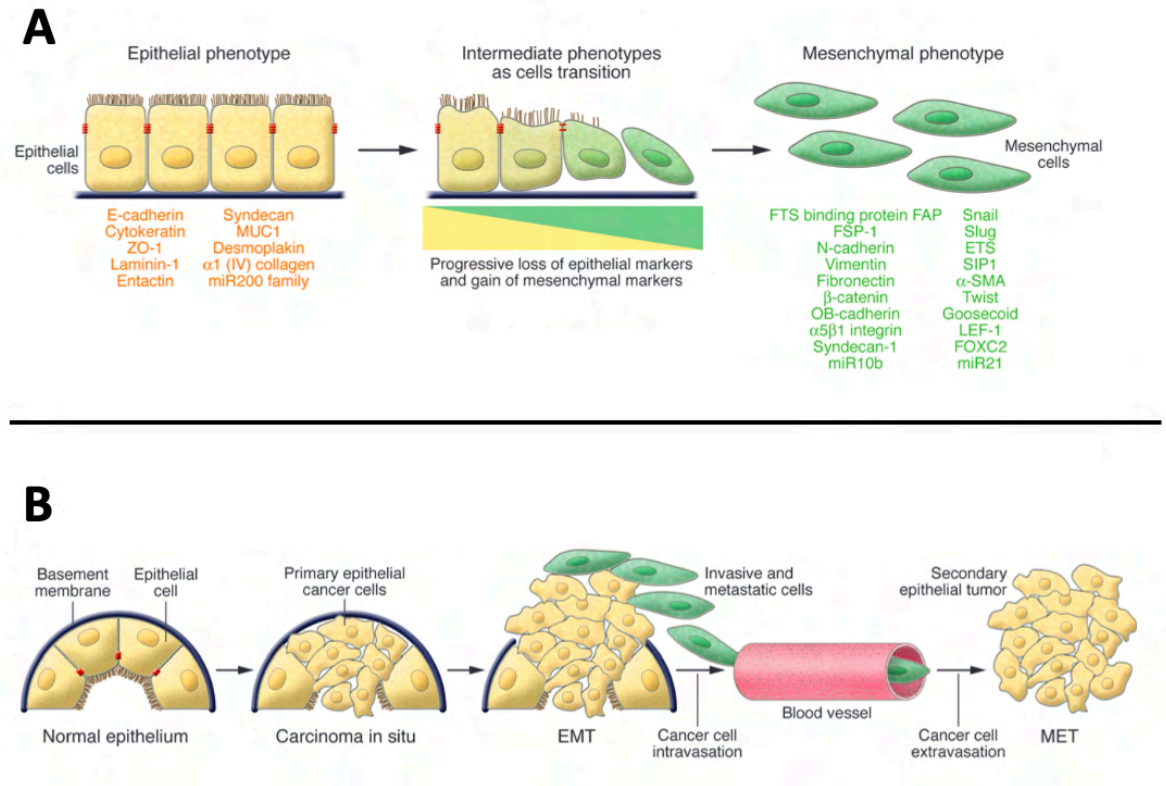

Figure 8. (A) Schematics of the Epithelial to Mesenchymal transition with their associated markers. (B) Schematic of the EMT and reversed process MET in the context of cancer invasion. Adapted from Kalluri et al. [39].

Metastatic cells have been generally characterized as softer than their healthy counterpart in most cancer [14,42,43] (**Figure 9A**), the reason for that deformability could be explained by the need of the metastatic cells during cancer progression to migrate through the basement membrane (both in EMT and MET) reorganizing their cytoskeleton [44,45] during extra and intravasation. The amount of actin has been related to cellular stiffness [46] and F-actin filaments and microtubules were found to be altered in more invasive cells [47]. At a cellular level, the glycocalyx has also been demonstrated to be affected by cancer: changes in its composition [25]

seem to be in favour of metastasis [26,27,48]. Targeting the glycocalyx to reduce cell migration and growth has been reported to have efficient and open potential for cancer biomarkers [24,48–51].

While the cells undergo internal changes during cancer progression, one cannot omit the niche of the cells: the extracellular matrix. The increase of specific collagen deposition during tumour formation induced by matrix crosslinking and ECM protein deposition [52–55] leads to stiffening [56–59] of the matrix. This process is called desmoplasia and is a direct response to tumour progression and metastasis. Among all the players of that (re)organization of the ECM we can identify the enzyme LOX [60] that by its upregulation, increases the collagen crosslinking by cancer-associated fibroblast CAFs [61]. CAFs oversee the remodelling and production of the matrix via matrix metalloproteinases (MMP), enzymes that degrade ECM by releasing growth factors and cytokines. High activity of MMPs has been correlated to tumour development [34,54,61,62]. In general, the matrix is found to be stiffer than its healthy counterpart, as presented in **Figure 9B**, for breast cancer [62,63], but also colon [64], peritoneum metastasis of colon cancer [65,66] and other cancers [67,68].

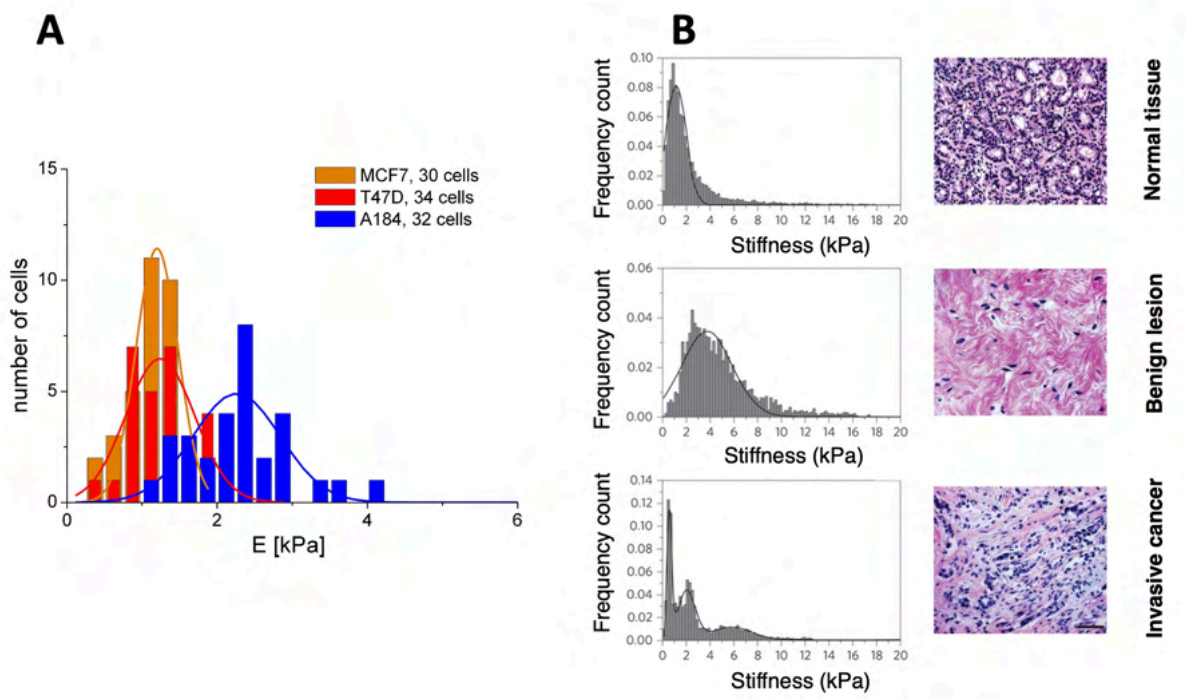

Figure 9. (A) The Young's modulus distributions with Gaussian fit for breast MCF7 and T47D cancer cell lines compared to normal breast 184A, adapted from Lekka et al.[45]. (B) Young's Modulus distribution for normal mammary gland tissue, benign lesion, and malignant tumour with their corresponding H&E-stained section, adapted from Plodinec et.al [63]. While cancer cells exhibit softer Young's Modulus in comparison to their normal counterpart, the breast cancer tissues get stiffer and show bimodal distribution with the invasiveness.

1.4. Bladder cancer and its mechanics

The bladder is composed of multiple layers, as shown in **Figure 10**. The first layer starting from the internal cavity is the mucosa, also called urothelium, principally made of epithelial cells. This is part of the organ in contact with urine. This internal part of the bladder is wrinkled, allowing the organ to undergo stretching while filled with urine and then emptied. It is followed by the submucosal (lamina propria), detrusor, and adventitia. We considered the muscle layers detrusor and adventitia part; the latest one constituting the external part of the bladder [69]. The decellularized ECM of the bladder is then mostly constituted by submucosal up to adventitia layers, since the urothelium, which is made of epithelial cells, is destroyed by the decellularization process.

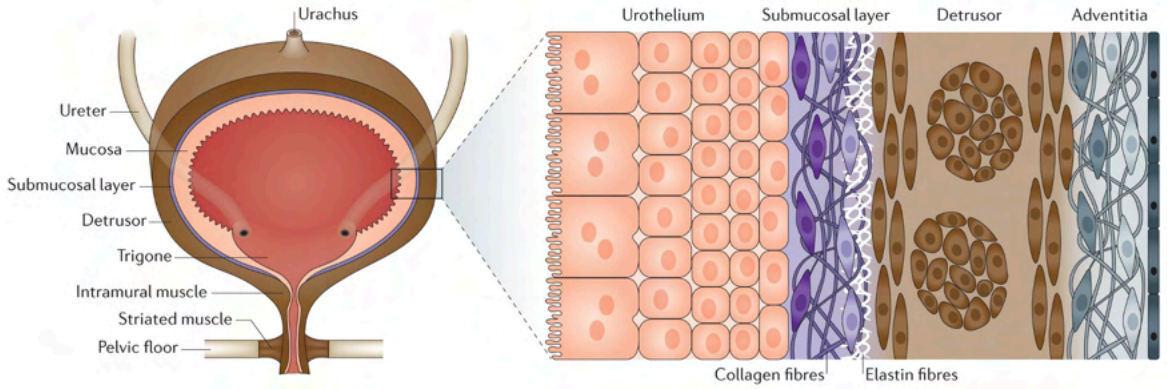

Figure 10. The bladder walls are composed of four layers: urothelium, submucosal, detrusor and the external surface, adventitia. Adapted from Ajalloueian et al.[69].

Bladder cancer, particularly urothelial carcinoma, is the most common urinary bladder cancer. There are two disease types: Non-Muscle Invasive (NMIBC) and Muscle Invasive (MIBC) bladder cancers, respectively, as presented in **Figure 11**. At diagnosis, 60% of cases are NMIBC. While the non-muscle invasive one requires trans-urethral resection of the bladder followed by chemotherapy as treatment, the other requires radical cystectomy (i.e., the removal of the whole organ). Bladder cancer is the 10th cancer in terms of new cases and the 13th in the number of deaths in 2020, according to the international agency for research in cancer [32,70]. The median age of patients detected with bladder cancer is 70 years, and it affects mostly male patients. The biggest risk factors of bladder cancer are environmental, such as exposure to carcinogenic molecules from contaminated water, as well as smoking [70].

There is currently a real need in the early diagnosis and disease monitoring of bladder cancer to provide personalized therapies to increase patients' longevity and reduce costs for the states. In both cancer types, a lifetime check is needed due to the possible relapse, making it one of the most expensive cancers to be treated.

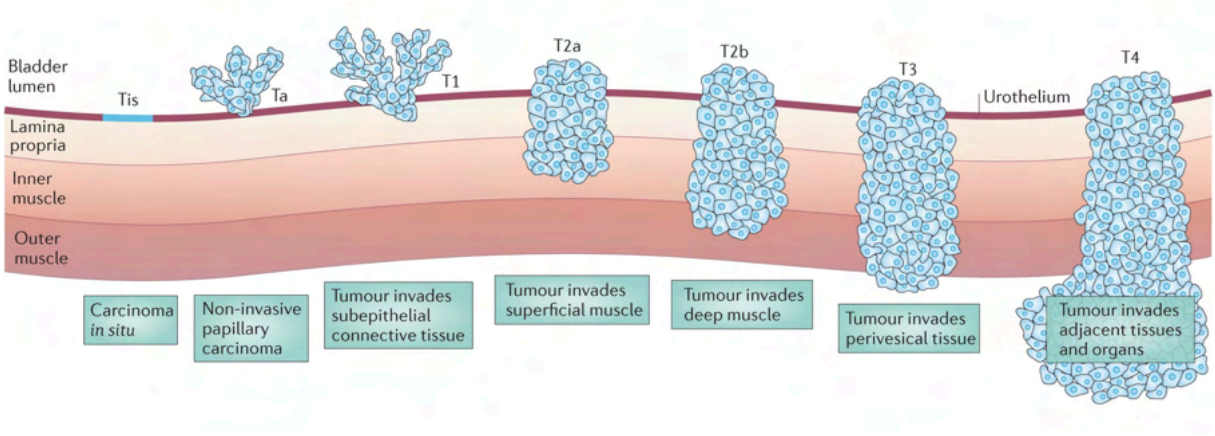

Figure 11. Stage of bladder cancer according to the Tumour-Node-Metastasis classification. Adapted from Knowles et al. 2015 [70]

At the cellular level, bladder cancer cells are showing the classical trend of cell softening during EMT. Many papers [42,43,71] characterized the mechanics of bladder cancer cells reporting evidence of the decrease of elasticity for the more metastatic cells, such as T24 used in that thesis. This trend has also been observed in many other cancers such as breast cancer [43,72,73]. The bladder tissues interestingly are not studied as much as its cells, most probably because of their huge mechanical flexibility due to the filling of the organ (from 9,6 kPa to 106,9 kPa with a 19-mmHg difference) [74].

Moreover, it has been observed that bladder matrix ultrastructure from MIBC patients was demonstrated denser and with a higher vascularization, with an increase of organization compared to their healthier conditions [75], also observed in colon cancer [64].

1.5. Atomic Force Microscopy for the study of biological interactions

Atomic Force Microscopy (AFM) is a branch of Scanning Probe Microscopy (SPM). The first member of the family, the Scanning Tunnelling Microscope STM was invented by Binnig et al. in 1982 [76] and awarded a Nobel Prize in 1986.

The system consists of a tip attached to an elastic cantilever that interacts with a surface while it is scanned across it or simply brought at a close distance (typically from 1 μm to contact). The interaction force causes the deflection of the cantilever, which is registered by an optical beam deflection (OBD) system based on a quadrant photodiode that reads the displacement of the spot of a laser reflected on the back of the cantilever [77–80] as shown in **Figure 12**.

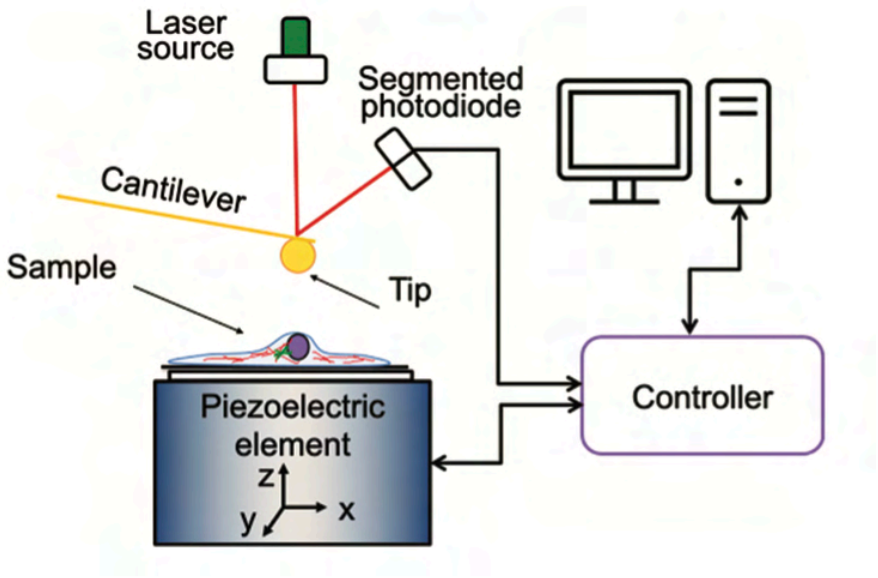

Figure 12. Schematic an atomic force microscope detection system including the optical beam deflection detection (OBD). Adapted from Ref. [77].

AFM can be used in different modes depending on the type of sample and measurement needed; it can be run both in air and liquid and in the case of biological sample measurement can be carried out also with temperature and CO_2 control [81,82] as shown in **Figure 14**.

Nanomechanical measurements by AFM consist of measuring the elastic deformation of the sample upon application of a controlled force [83,84]. The raw cantilever deflection vs displacement data are then properly rescaled into force vs indentation data in physical units and a suitable contact mechanics model is fitted to the force curves. To describe the working principles and the applications of AFM to characterize the statical mechanical properties of biological systems, from cells to tissues and ECMs, a recently published paper by Holuigue et al.[85] is reported at the end of this section. More specific methodological aspects are presented in the Material and Methods of each chapter of this thesis. Appendix A present the development of procedures to correct for the influence of a stiff substrate on the Young's modulus of elasticity of thin sample such as cells.

While the AFM is able, as discussed above, to test the mechanical properties of samples by nanoindentation measurements, it is also a reliable tool to sense weak forces related to biomolecular and adhesive processes. This particular application of AFM in the mechanobiology field is called force spectroscopy and includes, besides single molecule force spectroscopy, several types of cell-cell and single-cell force spectroscopies [86–88], which target specifically the study of cell-microenvironment interactions. AFM shows its versatility and value to perform mechanical investigations with a high spatial resolution (down to the nanoscale) and high force sensitivity (down to 10 pN), making it a reliable tool in quantitative biophysics [89].

In so-called Single Cell Force Spectroscopy (SCFS), among all potential configurations, we can point: cell-coated cantilever in contact with another cell (a single adherent cell or a cell within a confluent monolayer) to study cell-cell, cadherin-driven interactions (**Figure 13A**) [14,90,91] ; a cell-coated cantilever in contact with a functionalized substrate, decorated typically with adhesive motifs like fibronectin, collagen, vinculin, etc. to study cell-microenvironment

interactions [21,86,92,93] (**Figure 13B**). In single molecule force spectroscopy (SMFS), which is not considered in this study, the cantilever is typically functionalized by attaching single proteins and biomolecules and is brought to interact with a suitable substrate, where other biomolecules of counter molecules are present [87,88,94–96].

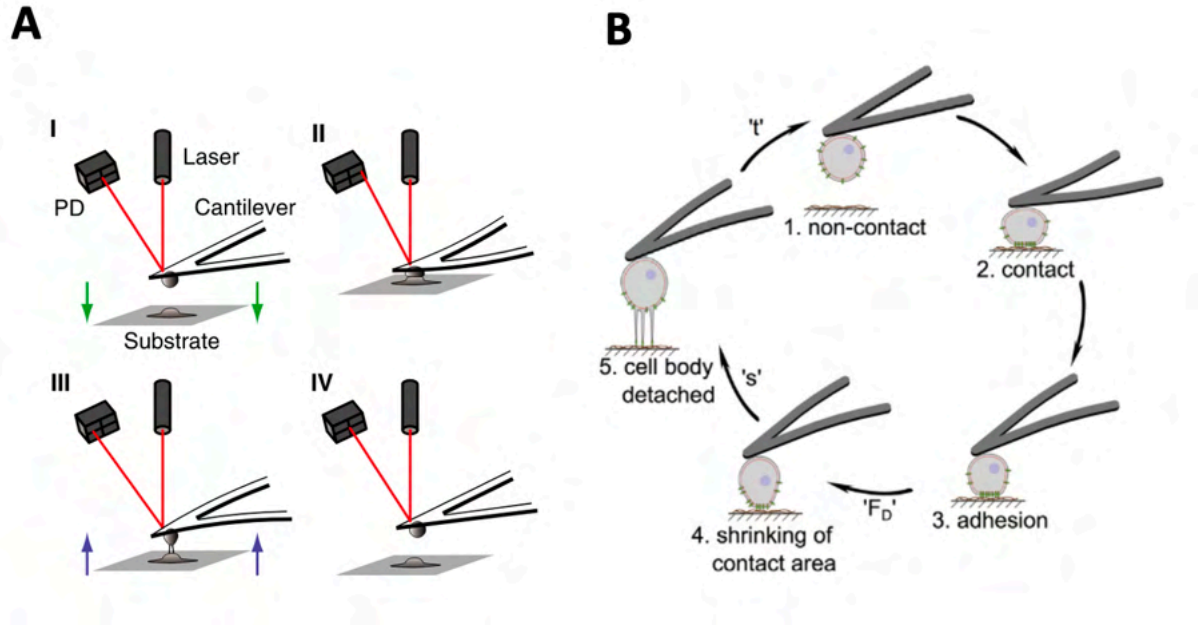

Figure 13. Scheme of Single Cell Force Spectroscopy. (A) A cell attached to a cantilever is brought into contact with another one for cell-cell measurements, adapted from Helenius et al. [91]. (B) A cell attached to the cantilever is entering in contact with a coated subs trate, adapted from Friedrichs et al.[97].

Other application of AFM includes the topographic imaging of biomolecules, cells, and tissues, a topic that we will not cover here [98–101]. AFM can also be combined with other complementary techniques, to implement correlative high-resolution microscopy, making it a very valuable tool for the investigation of biological systems[102]. To cite only a few techniques: electron microscopies [103,104], advanced fluorescence optical techniques [103,105–107], Raman [108,109] and Infrared [110] spectroscopy [83].

sensors

MDPI

Article

Force Sensing on Cells and Tissues by Atomic Force Microscopy

Hatice Holuigue [1], Ewelina Lorenc [1], Matteo Chighizola [1], Carsten Schulte [1], Luca Varinelli [2], Marcello Deraco [3], Marcello Guaglio [3], Manuela Gariboldi [2] and Alessandro Podestà [1,*]

[1] CIMAINA and Dipartimento di Fisica "Aldo Pontremoli", Università degli Studi di Milano, Via Celoria 16, 20133 Milan, Italy; hatice.holuigue@unimi.it (H.H.); ewelina.lorenc@unimi.it (E.L.); matteo.chighizola@unimi.it (M.C.); carsten.schulte@unimi.it (C.S.)
[2] Department of Research, Fondazione IRCCS Istituto Nazionale Tumori, Via G. Venezian 1, 20133 Milan, Italy; luca.varinelli@istitutotumori.mi.it (L.V.); manuela.gariboldi@istitutotumori.mi.it (M.G.)
[3] Peritoneal Surface Malignancies Unit, Colorectal Surgery, Fondazione IRCCS Istituto Nazionale Tumori, Via G. Venezian 1, 20133 Milan, Italy; marcello.deraco@istitutotumori.mi.it (M.D.); marcello.guaglio@istitutotumori.mi.it (M.G.)
* Correspondence: alessandro.podesta@mi.infn.it

Abstract: Biosensors are aimed at detecting tiny physical and chemical stimuli in biological systems. Physical forces are ubiquitous, being implied in all cellular processes, including cell adhesion, migration, and differentiation. Given the strong interplay between cells and their microenvironment, the extracellular matrix (ECM) and the structural and mechanical properties of the ECM play an important role in the transmission of external stimuli to single cells within the tissue. Vice versa, cells themselves also use self-generated forces to probe the biophysical properties of the ECM. ECM mechanics influence cell fate, regulate tissue development, and show peculiar features in health and disease conditions of living organisms. Force sensing in biological systems is therefore crucial to dissecting and understanding complex biological processes, such as mechanotransduction. Atomic Force Microscopy (AFM), which can both sense and apply forces at the nanoscale, with sub-nanonewton sensitivity, represents an enabling technology and a crucial experimental tool in biophysics and mechanobiology. In this work, we report on the application of AFM to the study of biomechanical fingerprints of different components of biological systems, such as the ECM, the whole cell, and cellular components, such as the nucleus, lamellipodia and the glycocalyx. We show that physical observables such as the (spatially resolved) Young's Modulus (YM) of elasticity of ECMs or cells, and the effective thickness and stiffness of the glycocalyx, can be quantitatively characterized by AFM. Their modification can be correlated to changes in the microenvironment, physio-pathological conditions, or gene regulation.

Keywords: Atomic Force Microscopy; colloidal probe; biosensors; glycocalyx; extracellular matrix; mechanobiology

check for updates

Citation: Holuigue, H.; Lorenc, E.; Chighizola, M.; Schulte, C.; Varinelli, L.; Deraco, M.; Guaglio, M.; Gariboldi, M.; Podestà, A. Force Sensing on Cells and Tissues by Atomic Force Microscopy. *Sensors* **2022**, *22*, 2197. https://doi.org/10.3390/s22062197

Academic Editors: Paolo Facci and Andrea Alessandrini

Received: 6 February 2022
Accepted: 9 March 2022
Published: 11 March 2022

1. Introduction

In recent years, there has been a growing interest in studying the physical properties of biological samples, such as tissues, single cells, and their microenvironment, to better understand how they change during the progression of diseases, such as cancer [1–3], and how they influence each other in their mutual interaction [4–11]. The extracellular matrix (ECM), which is a fundamental component of the cell microenvironment, is a ubiquitous acellulated component present in all tissues, comprising molecules that are secreted by cells and assembled to form specific insoluble components; the ECM plays a fundamental role as a scaffold for cell growth, in the regulation of cell-cell and cell-matrix signaling, also affecting cell mechanics mainly through the remodeling of the cytoskeleton, and determining cell fate [4,5,12–16]. There is a reciprocal interaction between the ECM and the cells, allowing the active modification of the ECM structure and composition, which

affects its mechanical properties as well [9,17–19]. An important physical layer is located between the cell membrane and the cell microenvironment: the glycocalyx, also known as the pericellular matrix. The glycocalyx is a surface brush layer that is present on every cell, and made of glycoproteins, proteoglycans and polysaccharides [16,20]. As the first contact interface between the cell and its microenvironment, the glycocalyx plays an important role in their mutual interactions [21]. The glycocalyx acts as a water reservoir, helps in the transport of metabolites and control of the signaling molecules [20,22], regulates integrin clustering and focal adhesion maturation [21,23–25]. The characterization of the glycocalyx thickness in relation to different pathological states of the cell would help to understand the communication between cells and the ECM [26]. More importantly, a link has been demonstrated between glycocalyx and cancer: tumoral cells tend to show a wider distribution of glycocalyx chain lengths compared to normal ones [27]; moreover, their bulky composition seems to favor the metastatic spread [28–30]. The physical characterization of glycocalyx has a good potential in cancer research, both as a cancer biomarker [20,25,27,30,31] and as a therapeutic target, since the reduction or degradation of the glycocalyx has been reported to reduce cell migration and suppress cell growth [32,33].

The study of the mechanical properties of cells and tissues in the context of health and disease implies the need for reliable instrumentation and methods. Atomic Force Microscopy (AFM), which is able to both sense and apply forces at the nanoscale, with sub-nanonewton sensitivity, represents an enabling technology and a crucial experimental tool in biophysics and biomechanics [34–37].

In AFM, an elastic cantilever with an intrinsic spring constant k in the range 0.05–50 N/m is used as both a force sensor and a force transducer (Figure 1A). The surface force F is applied on the cantilever, typically at its end, where a micro-tip with a radius of curvature of typically 2–100 nm is located. The force induces a vertical cantilever deflection $z = F/k_{eff}$, which is typically measured by an optical beam deflection apparatus [38–40] (Figure 1), or in some cases by an interferometer [41]. In the above equation, an effective spring constant k_{eff} is used, rather than the intrinsic one, to account for specific features of the loading configuration, such as the cantilever mounting angle θ (usually θ = 10°–15°), the tip height, the loading point position, etc. [42]. In the simplest case of a negligibly small tip at the very end of the cantilever, $k_{eff} = k/\cos^2(\theta)$.

A small spring constant provides high force sensitivity, meaning that a small force produces a large, easily measurable, deflection. A lower limit to the measurable deflection (and therefore to the measurable force) is set by the thermal noise z_{th} of the cantilever, which can be estimated from the equipartition theorem as $z_{th} = \sqrt{k_B T/k}$, with k_B and T being the Boltzmann constant and the absolute temperature, respectively [43,44]. The minimum, thermal noise, limited detectable force that can be measured dynamically with an instrumental bandwidth BW is $F_{th,min} = \sqrt{4k_B TbBW}$, where b is the damping coefficient (the proportionality factor between the tip velocity and the viscous force). Equivalently, since $b = k/(2\pi f_R Q)$, $F_{th,min} = \sqrt{2k_B TkBW/(\pi f_R Q)}$; Q and f_R being the quality factor and the resonance frequency of the cantilever, respectively; similar expressions for the minimum force gradients can be obtained [45,46].

Besides measuring the tip-sample interaction force with sub-nN sensitivity, AFM allows us to reconstruct the tip-sample distance corresponding to the force measurements, which translates into a sample deformation after contact is established [47]. The possibility of measuring force vs. distance, spatially resolved with nm resolution, assigns AFM a leading position as a force (bio) sensing technique. AFM is at present an enabling technology and a crucial experimental tool in biophysics and biomechanics, allowing both force spectroscopy and nanomechanical characterization of biologically relevant interfaces and systems.

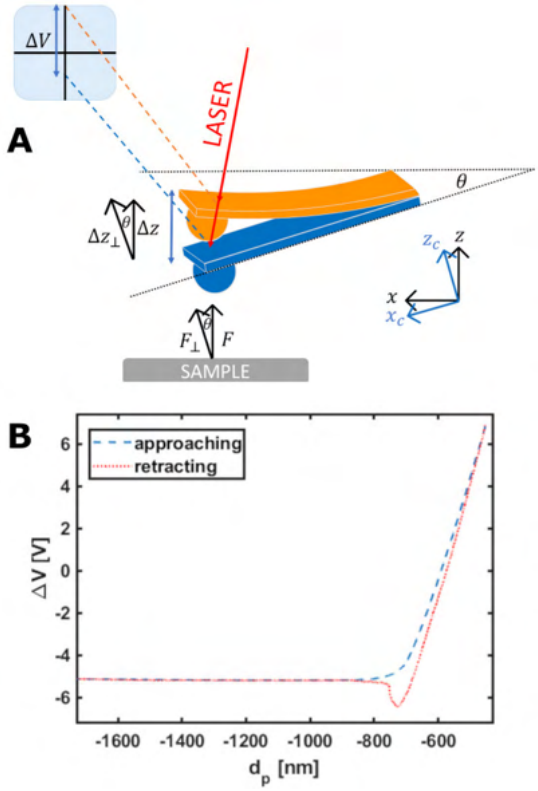

Figure 1. (**A**) Scheme of the optical beam deflection (OBD) system. The vertical displacement of the cantilever induced by the sensing of a force F perpendicular to the sample surface is detected on a segmented photodiode as a raw voltage signal ΔV. The cantilever is typically mounted at an angle θ with respect to the sample surface. (**B**) A raw force curve, representing the photodiode output ΔV as a function of the z-piezo displacement d_p. Both the approaching and retracting branches of the curve are shown.

In this work, we present an overview of how AFM can be used as an enabling force-sensing technology for the study of biological systems at different spatial and force scales. To this purpose, we report on the application of AFM to the study of biomechanical fingerprints of several components of biological systems, such as the ECM, the whole cell, and cellular components, such as the nucleus, lamellipodia and the glycocalyx. We show that physical observables such as the (spatially resolved) Young's Modulus of elasticity of ECMs or cells and the effective thickness and stiffness of the glycocalyx can be quantitatively characterized by AFM. In particular, we carried out three representative experiments from the microscale to the nanoscale: mechanics on healthy and neoplastic decellularized tissue from one patient with peritoneal metastasis; mechanics of three bladder cancer cell lines who are representative of the progression of urothelial bladder cancer; and eventually glycocalyx characterization of those cell lines. We demonstrate through these illustrative experiments the high sensitivity that can be achieved with AFM on detecting small changes in the biomechanical properties of biological samples, from single living cells and their biomolecular components to tissues; the modification of these biophysical observables can in turn be correlated to changes of the cell microenvironment, physio-pathological conditions of the tissue and related organs, or gene regulation phenomena.

2. Materials and Methods

2.1. Sample Preparation

2.1.1. Human Tissues

Peritoneal tissue was collected from one patient with peritoneal metastatic colorectal carcinoma (CRCPM) who underwent surgical resection at the Peritoneal Malignancies Unit of the IRCCS Foundation, Istituto Nazionale dei Tumori di Milano, Milan, Italy. The patient was staged according to the World Health Organization (WHO) classification. The study was approved by the Institutional review board (249/19) and was conducted in accordance with the Declaration of Helsinki, 2009. Written informed consent was acquired.

Omentum-derived CRCPM lesion and apparently normal tissue (>10 cm from the metastatic lesion) were harvested. Tissues were frozen in liquid nitrogen and used to develop the decellularized ECMs.

2.1.2. Decellularized Extracellular Matrices

Decellularized extracellular matrices were obtained from the omentum fold of human peritoneum from a patient with metastases derived from colorectal cancer. The decellularization was performed as in Genovese et al. [48]. The success of the decellularization procedure was already verified in the work from Varinelli et al. [49]. The ECM samples were embedded in optical cutting compound (OCT) and frozen in 2-propanol, then kept in a liquid nitrogen bath.

ECM slices of approximately 100 µm thickness were cut with a microtome (Leica) and attached to positively charged poly-L-lysine-coated glass coverslips (ThermoFisher Scientific, Waltham, MA, USA) exploiting the electrostatic interactions to improve the attachment. The samples were stored at -4 °C until AFM analysis.

2.1.3. Cells

Three commercial human bladder cancer cell lines of different grades (a marker of invasiveness), kindly provided by Dr. M. Alfano (San Raffaele Hospital, Milano), were used (see Table 1) [50,51]. The cell lines were cultured in RPMI medium containing 2 mM L-glutamine supplemented with 10% FBS, 1% penicillin/streptomycin, and 1% amphotericin and grown in an incubator at 37 °C and 5% CO_2 (Galaxy S, RS Biotech). All reagents and material were from Sigma-Aldrich (St. Louis, MO, USA) if not stated otherwise.

Table 1. Characteristics of the bladder cancer cell lines used in this work.

Cell Line	Specie/Organ	Morphology	Tumor
RT4	Human Bladder	Epithelial	Papilloma, transitional cell (Grade I)
RT112	Human Bladder	Epithelial	Papilloma, transitional cell (Grade II)
T24	Human Bladder	Epithelial	Carcinoma, transitional cell (Grade III)

For AFM measurements, the cells were plated the day before on glass bottom Petri dishes (⌀ 40 mm Willco Wells) coated with poly-L-lysine (0.1% w/v for 30 min at RT) to improve cell attachment, in the RPMI medium without phenol red, as it can cause damage to the AFM probe holder.

2.2. Histochemistry

Before histochemistry staining, ECM Formalin-Fixed Paraffin-Embedded (FFPE) sections were cut into slices and dewaxed in xylene, rehydrated through decreasing concentrations of ethanol, and washed with water. Slices were stained with van Gieson trichrome (Bio-Optica, Milan, Italy) following the manufacturers' instructions.

2.3. Force Sensing with the AFM

All the experiments have been performed using a Bioscope Catalyst AFM (Bruker) mounted on top of an inverted microscope optical microscope (Olympus X71, Tokyo, Japan).

The system was isolated from noise using an active antivibration base (DVIA-T45, Daeil Systems, Wonsam-myeon, South Korea) placed inside an acoustic enclosure (Schaefer, Vigilliano Biellese, Italy). Living cells were measured using a thermostatic fluid cell, with the temperature of the medium kept at 37 °C by a temperature controller (Lakeshore 331, OH, USA). The measurements on ECMs were performed at room temperature in a droplet of PBS confined on the glass slide using a hydrophobic pen.

Homemade colloidal probes were produced by attaching borosilicate glass or soda lime spheres to rectangular tipless cantilevers (NanoandMore TL-FM and MikroMasch HQ:CSC38/Tipless/No Al); both production of the probes and characterization of their radius were performed according to custom procedures [52]. Different sphere radii R and spring constants k of the probes were selected according to the needs of each experiment (Table 2).

Table 2. Radius and typical spring constant of the AFM probes used for every experiment.

Experiment	Colloidal Probe Radius (μm)	Spring Constant (N/m)
Mechanics of the ECM	20	5
Mechanics of cells	5	0.01
Glycocalyx characterization	5	0.01

The raw output on an AFM force measurement consists of the raw deflection signal ΔV of the cantilever, measured by the optical beam deflection (OBD) system in volts, as a function of the z-piezo displacement d_p, in nm units (Figure 1A,B). Depending on the AFM system, the z-piezo can displace either the probe or the sample.

Exploiting two calibration parameters, the effective spring constant k_{eff} (N/m) and the deflection sensitivity S (or inverse optical lever sensitivity invOLS, in units of nm/V), the raw deflection ΔV can be transformed into the cantilever deflection z, in nm, and the latter deflection can then be transformed into a force, in nN:

$$z = S\,\Delta V \tag{1}$$

$$F = k_{eff}\,z = k_{eff}\,S\,\Delta V \tag{2}$$

The tip-sample distance d can be calculated as:

$$d = d_p + z - d_0 \tag{3}$$

In Equation (3), d_p decreases as the tip gets closer to the sample surface, and z is positive when the cantilever is deflected upwards, under the action of a repulsive force, and negative in the opposite case. The parameter d_0 represents the location along the $d_p + z$ axis where the tip-sample distance is zero. The identification of d_0 is easy when the tip is ramped against a stiff substrate, since all data points belonging to the contact region of the force vs. $d_p + z$ distance curve must collapse along a vertical line, whose corresponding mean abscissa value is d_0. On deformable surfaces, d_0 is typically obtained through a fit of a suitable contact mechanics model (typically the Hertz model [53–55]) to the F vs. $d_p + z$ curve [56].

The cantilever spring constant has been calibrated using the thermal noise method [43,44], and fine corrections were applied to account for geometrical and dimensional issues [42,57]. The deflection sensitivity S of these probes was calculated according to different procedures: either as the inverse of the slope of the raw deflection ΔV vs. z-piezo displacement d_p curve (Figure 1B) acquired on a stiff substrate [47], or via the SNAP method [58], assuming a previously accurately calibrated intrinsic spring constant as reference.

After identification of d_0 and proper translation of the distance axis, negative distances correspond to deformations, i.e., indentations of the deformable sample. In nanomechanical tests, the negative semiaxis is the relevant one, and an indentation axis δ can be defined as: $\delta = -d$, for $d < 0$.

Processing of the data was carried out using custom routines written in a Matlab environment (Mathworks, Natick, MA, USA).

The precise alignment of AFM and optical images was possible using the Bruker MIRO software and allowed us to choose the regions of interest for ECMs and cells. For the ECMs, the regions for measurements were chosen based on the evaluation of optical images; thanks to the reduced thickness of the slices and their consequent transparency, it was possible to select regions with moderate roughness and better structural integrity.

Indentation of Living Cells and ECMs by AFM

- Cells

For the mechanical characterization of cells, the Hertz model was applied [53–55]. To extract the value of the Young's Modulus (YM) E, which is the proportionality constant (within the limits of linear elastic response) of stress σ (force per unit area, in Pa) and strain ε (relative deformation): $E = \sigma/\varepsilon$. The YM is an intrinsic elastic property of a material and provides a measure of sample rigidity. According to the Hertz model for a parabolic indenter, the force vs. indentation relation is:

$$F = \frac{4}{3}\frac{E}{1-\nu^2}R^{\frac{1}{2}}\delta^{\frac{3}{2}} \quad (4)$$

which is accurate as long as the indentation δ is small compared to the radius R. In Equation (4), ν is the Poisson's coefficient, which is typically assumed to be equal to 0.5 for incompressible materials.

When indenting compliant thin cells (typically a few microns tall at their maximum height, i.e., above their nucleus), the finite-thickness effect must be taken into account. This effect is related to the influence of the stiff glass substrate underneath the cells, which confines the strain and stress fields and makes the elastic cell response stiffer, i.e., the measured Young's Modulus larger [55,59–62]. The finite-thickness correction depends on the ratio χ of the contact radius $a = \sqrt{R\delta}$ to the sample thickness h (and not trivially on the ratio δ/h):

$$\chi = \frac{\sqrt{R\delta}}{h} \quad (5)$$

Notably, AFM provides the unique capability of measuring simultaneously both the height and elastic properties of a sample (combining topographic and mechanical imaging [55]), therefore allowing us to implement point by point corrections that depend on ratios like the one reported in Equation (5) as for the present work.

A polynomial correction factor Δ(χ) can be applied to the Hertz equation (Equation (4)), under the hypothesis that cells are partially bound to the substrate, and this allows us to extract correct YM values irrespective of the local thickness of the sample. Following Dimitriadis et al.'s work [55,59]:

$$\Delta(\chi) = 1{+}1.009\chi + 1.032\chi^2 + 0.578\chi^3 + 0.051\chi^4 \quad (6)$$

Introducing the rescaled force $F'(\delta) = F(\delta)/\Delta(\chi(\delta))$, Equation (4) can be replaced by the formally similar Equation (7):

$$F' = \frac{4}{3}\frac{E}{1-\nu^2}R^{\frac{1}{2}}\delta^{\frac{3}{2}} \quad (7)$$

For the evaluation of the Young's Modulus of single and clustered cells, at least 10 cells, each from three to five Petri dishes, were measured. For each measurement, FCs on both the substrate and the cells were acquired with a minimum of 10 FCs on the surrounding substrate and 100 FCs on the cell; this allowed us to calculate the local height of each single cell [55]. For full mapping of single cells/clusters, FCs were collected on a grid spanning an area of up to 100 μm × 100 μm around the cells, including both cells and substrate. Each FC contained 8192 points, with ramp length l = 15 μm, maximum load Fmax = 5–10 nN, ramp

frequency f = 1 Hz. The probe radius was R = 5.7 µm or R = 6.4 µm. Typically, indentation up to 2 µm was achieved.

We created masks based on the obtained topographic maps to select force curves belonging to distinct regions: the nuclear region and its complement, which is the union of cell perinuclear and peripheral regions [55,62].

The same data were used for both mechanical analysis of cells and glycocalyx characterization. The first 10% of the indentation range after the contact point is usually attributed to the contribution of the glycocalyx [21,27,31,63,64]. The YM of the cells was extracted by fitting the Hertz model to the FCs in a suitable sub-interval of the remaining 10–90% indentation, typically identified as the range where the value of E does not change with indentation (Figure 2).

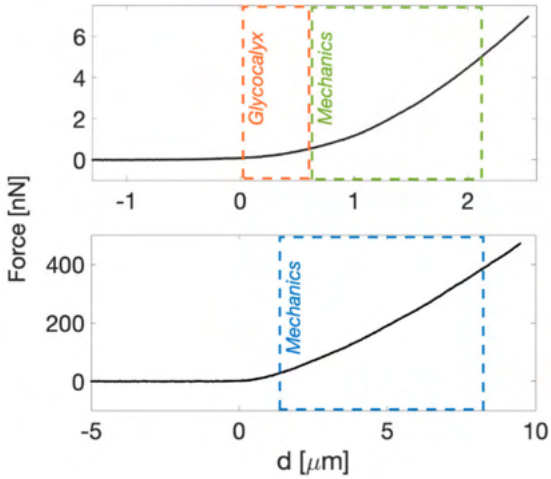

Figure 2. Typical approaching force curve on top of a cell (**top**) and ECM (**bottom**). The indentation range for model fitting is highlighted; on cells, we used typically [0–10%] for the glycocalyx and [10–80%] for the YM, while on ECMs we used [20–80%] for the Young's Modulus.

- Glycocalyx thickness

The glycocalyx characterization was performed following the soft brush model implemented by Sokolov et al. [27,31,65,66]. The separation H between the tip and the cell membrane can be expressed as (Figure 3A):

$$H = d_p - d_0 + \delta + z \quad (8)$$

where d_0 is the position of the non-deformed cell membrane (the contact point referred to Hertzian indentation), d_p is the relative z-piezo position, and δ and z are indentation and cantilever deflection, respectively, as previously defined.

The indentation δ in Equation (8) is calculated using the standard Hertz model (Equation (4)). When the glycocalyx is completely compressed (which typically occurs well before cell indentation is significant), H is negligibly small; it follows that if one plots the force as a function of H, the force points related to the Hertzian indentation of the cell collapse along a vertical line at $H \cong 0$. This can be seen in Figure 3B, where the force for $H > 0$ can be identified with $F_{glycocalyx}$, the force exerted by the glycocalyx. The latter force can be modeled as [65]:

$$F_{glycocalyx} = 100\, k_B T\, R\, N^{3/2}\, L \exp(-2\pi H/L) \quad (9)$$

where L and N are the effective thickness and the grafting density of the pericellular brush, respectively.

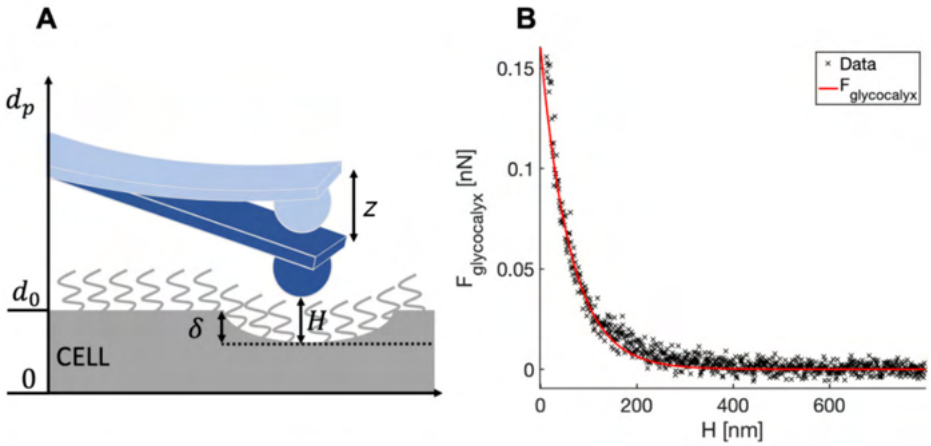

Figure 3. (**A**) Schematics of the distances used to determine the tip-cell membrane distance H (Equation (8)). (**B**) A typical force curve showing the force exerted by the glycocalyx as a function of the tip-cell membrane distance (the red continuous curve is the fit by Equation (9)).

- ECM

The mechanical properties of ECMs were studied by collecting sets of typically 15 × 15 force curves (force volumes, FV) in different macroscopically separated regions of the sample. Each selected region was typically as large as 115 µm × 115 µm. Each FC contained 8192 points, with ramp length L = 15 µm, maximum load Fmax = 800–1500 nN, ramp frequency f = 1 Hz and R = 12.8 µm. Typical maximum indentation was 5–9 µm. For each patient condition, 2000–5000 FCs were obtained.

The value of the YM of elasticity of ECM was extracted as described previously for cells. The Hertz model was fitted to the [20–80%] indentation range of the FCs (Figure 2) without the finite-thickness correction (given the large thickness of the slices, $\chi \leq 0.1$). On tissues and ECMs, the first 20% of the FCs is typically neglected, due to the contribution of superficial non-crosslinked fibers, surface roughness -related issues, etc. [5].

2.4. Statistics

For both cells and ECM, the mean median value $\bar{E}_{med}$ of the Young's Modulus E (or the mean values of other observables) has been evaluated for each tested condition, averaging over cells or measured ECM samples. The associated errors were calculated adding in quadrature to the standard deviation of the mean $\sigma_{\bar{E}_{med}}$ an instrumental error of 3%, calculated through a Monte Carlo simulation, as described in [55,67], based on the uncertainties in the calibration parameters (5% for the deflection sensitivity S, 10% for the spring constant k).

The assessment of the statistical significance of the differences among the tested conditions was carried out using the two-tailed *t*-test. A *p*-value < 0.05 was considered statistically significant.

For the glycocalyx analysis, the length L of the glycocalyx for each force curve located on the nucleus was extracted, by fitting Equation (9) to the data, and the histograms of the logarithmic values were reported. Median values were calculated.

3. Results

3.1. AFM at the Microscale: Mechanical Properties of ECMs

In this experiment, we carried out mechanical measurements on healthy and neoplastic decellularized extracellular matrices coming from the same patient affected by CRCPM. We measured YM values of the samples at deep indentation with a focus on their distribution.

The production of custom colloidal probes allows us to tune both the spring constant k of the cantilever and the sphere radius R, to match the typical length scale of tissues and ECMs, which is approximately 10–50 μm (cf. Material and Methods)

Exploiting the large colloidal probe radius allows us to effectively average local nanoscale heterogeneities due to the fine structure of the ECM, while capturing the overall mesoscopic mechanical response of the sample. To this purpose, it is important to achieve reasonably large (in absolute terms) indentations (5–9 μm, compared to the 100–200 μm thickness of the samples). In these operative conditions, finite-thickness effects are negligible, and we are confident to test the bulk sample properties, as in a 3D structure, and not only those of a surface layer, which in similar samples can be different from the bulk. The measured mechanical response therefore reflects the collective contribution of all components of the ECM, organized in micrometer-sized structural and functional domains [5,17,68–72]. Small colloidal probes, and to a larger extent sharp pyramidal tips, would permit a greater spatial resolution, but the mechanical output would be more scattered and less representative of the overall properties of the ECM [55].

In Figure 4A, we show the distribution of the logarithmic YM values from each FC taken on ECM samples. The fact that log YM values are approximately normally distributed suggests that the distribution of YM is lognormal, as it is typically observed [73].

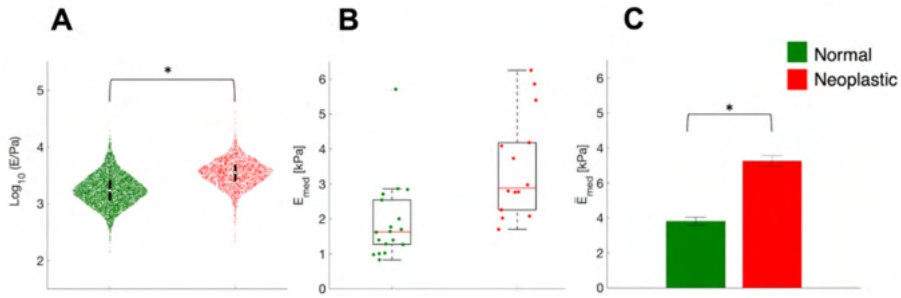

Figure 4. The stiffening of ECM in CRCPM samples. (**A**) Logarithmic values of the YM and their distribution in normal and neoplastic ECM samples obtained from one patient. Violin plots were plotted collecting YM values from all single FCs. Violin plots suggest that the distribution of local YM values is approximately lognormal. The circle and the black bars represent the median and the interval between 25th and 75th percentiles. (**B**) Comparison of median YM values E_{med} from each force volume in linear scale for normal and neoplastic samples from one patient. The red line represents the median value, the box encloses the interval between 25th and 75th percentiles of the sample. Whiskers go from the upper and lower limits of the interquartile range to the furthest observations, within 1.5× the interquartile range; data points beyond this limit are considered outliers. (**C**) Comparison of the mean median YM values for the two conditions tested. In (A, C), * means $p < 0.05$.

During cancer progression, the neoplastic ECM becomes stiffer; indeed, the logarithmic YM distribution appears rigidly shifted to higher values (higher median value), while the logarithmic standard deviation is approximately preserved among normal and neoplastic conditions (Figure 4A). In Figure 4B, we show the distribution of the median YM values measured in different locations (FV) and slices of ECM are reported. Neoplastic-derived samples showed a significant increase in stiffness, and this result was in line with data already published [1,2,9,74–76]; this stiffening during cancer progression is related to an outcome of the tumor microenvironment remodeling and changes in the ECM composition and structure, including aggregation and realignment of ECM components, mediated by tumoral cells [9]. Reorganization of the matrix through cancer progression is also a parameter that can be seen optically, with classical staining of the ECM (Figure 5). The neoplastic ECM shows collagen accumulation (Figure 5B), while the healthy counterpart shows organized collagen fibers (Figure 5A).

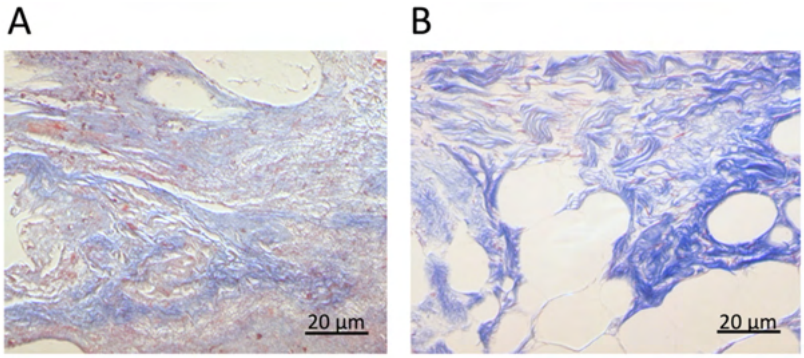

Figure 5. Collagen of ECM of healthy (**A**) and tumoral region (**B**) stained with van Gieson trichrome.

3.2. Mechanics of Cell, down to Cellular Components

Using AFM, it is also possible to sense small mechanical changes in single cells related to different physio-pathological conditions; using colloidal probes, the spatial resolution can be good enough to discriminate among single cell components, such as nuclear and perinuclear regions and lamellipodia [55], while sharp tips allow us to discriminate fine cellular structures as small as single actin fibers [77].

We performed AFM nanoindentation on three bladder cancer-derived cell lines, RT4, RT112, and T24, with different degrees of invasiveness (Table 1), and compared their median YM values.

From the force vs. distance curves, we reconstructed three-dimensional cell morphologies and the mechanical maps, as described in [55]. All FCs, and consequently all maps, have been corrected for the contribution of the finite-thickness of the sample, as explained in the Methods.

Mapping both topography and YM and comparing with the optical image (Figure 6) allowed us to decouple the contributions of the nuclear regions and the other regions of the cells in the same cluster. Examples of the distributions and median values of the YM extracted from different parts of the cell body (e.g., nuclear vs. perinuclear and peripheral regions, or lamellipodia) are shown in Figures 7 and 8.

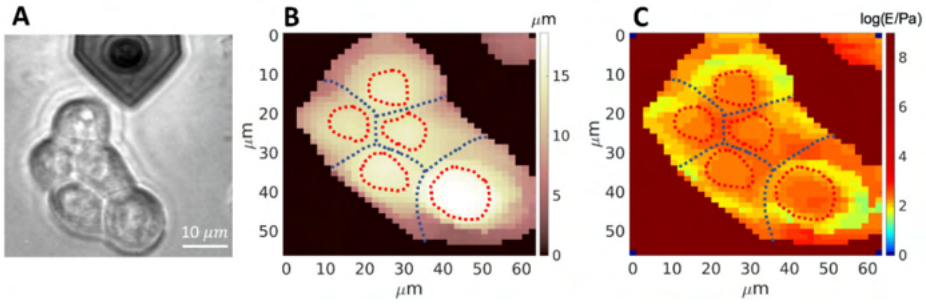

Figure 6. Representative images for the combined topographical and mechanical analysis of cell clusters. Optical image of a cell cluster from the RT112 cell line (**A**); topographic map (**B**), and Young's modulus map (**C**) in logarithmic scale, of the same cluster shown in (**A**).

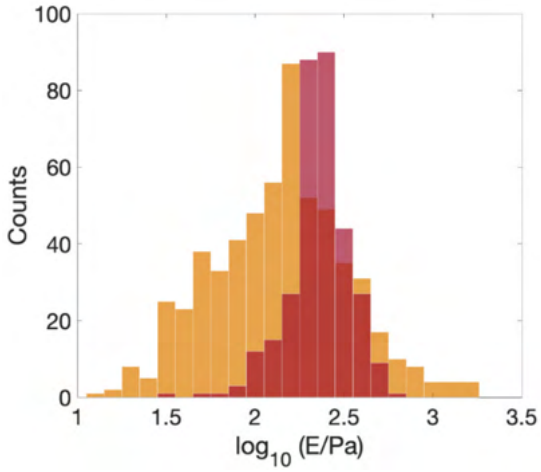

Figure 7. Histograms of the YM from the perinuclear and peripheral region of an RT112 cell (orange), and from the nuclear region (red).

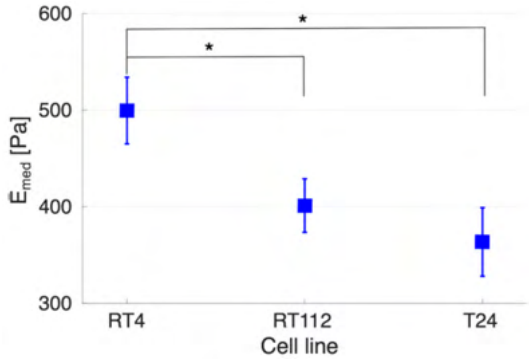

Figure 8. The Young's modulus (whole cell) measured by AFM for bladder cancer cells RT4, RT112, and T24, with increasing grades of invasiveness (left to right). * Means $p < 0.05$.

As shown in Figure 8, the higher degree of invasiveness of cells (from RT4 to T24) correlates to a decrease in the YM (whole-cell value); this is consistent with previously published data [78]. The reported differences in YM between cell lines RT4 and RT112 and between RT4 and T24 were found to be significant, while this was not the case between RT112 and T24.

We observed a wider distribution of the YM values in the perinuclear and peripheral regions of the cells, compared to the nuclear region (Figure 7). In the perinuclear and peripheral regions, both softer and stiffer areas coexist, as shown in Figure 6C; the higher Young's Modulus values are found at the cell-cell boundaries, where adherent junctions are present. The nuclear region exhibits a narrower distribution of YM values (Figure 7) and is stiffer than the perinuclear region, as reported previously [19,79].

It is well known that during embryonic and cancer development, cells exhibit a softening that can favor extravasating through the blood capillaries, allowing the attachment to a secondary site, favoring the metastatic spread in cancer [80]. The softening of the neoplastic cells has already been reported in breast and bladder cancer models [80–83]. It was reported that RT112 cells possess both mesenchymal and epithelial phenotypes as they are an intermediate cell line for those states [11,84]. In our case, this correlates with the intermediate YM values observed for these cells compared to RT4 and T24.

3.3. Down to the Nanoscale: Characterization of the Glycocalyx

As previously described, AFM is capable of sensing the mechanical resistance to compression of tissue components such as cells and ECM; it is possible to go further down along the size and force scales, characterizing even smaller and more delicate structures such as the pericellular matrix, a sugar-rich coat, called glycocalyx.

Many models have been developed for the data analysis and the characterization of the glycocalyx and similar brushes [27,85]. Here, we followed the protocol developed by Sokolov et al. [21,27,31,66], which is based on decoupling the deformation of the ultrasoft glycocalyx layer on top of the soft cell, within the acquired FCs. We applied this model to the FCs collected for the nanomechanical measurement of bladder cancer cells, to prove the feasibility of extracting more information from the same data set (see Section 2).

To better appreciate the subtle differences between the three cell lines RT4, RT112, and T24, we considered the distribution of the glycocalyx thickness values extracted from the single FCs in log scale (Figure 9). There are differences in the distributions of L values in the three cases. Compared to the intermediate grade of invasiveness (RT112), the less and most invasive cells (RT4 and T24, respectively) possess a broader distribution of brush lengths, with tails extending towards longer and shorter lengths, respectively; the median values of the glycocalyx thickness therefore tends to decrease going toward a higher degree of invasiveness, from L = 730 nm (RT4 and RT112) to L = 652 nm (T24). Nevertheless, the distribution seems to possess different modes (highlighted by the dotted vertical lines in Figure 9), and one can see that the relative importance of higher-thickness modes increases for more invasive cells, which are also characterized by the more asymmetric brush length distribution, as it was observed for tumoral cells [25,30]. These data suggest that beside the mere thickness/length of the brush, also the change of other glycocalyx physical properties such as the stiffness, the effective graft density, and degree of crosslinking should be quantitatively characterized since they are likely correlated to the transformation of a tissue from a normal to neoplastic condition.

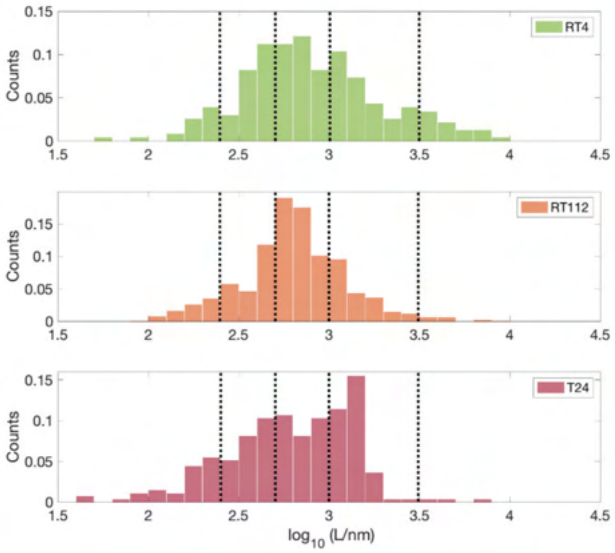

Figure 9. Distribution of the lengths of the glycocalyx brush (extracted according to Equation (9) from single FCs) for the three cell lines RT4, RT112, and T24. Vertical dotted lines are a guide for the eye in the tentative identification of the main modes of the distributions.

4. Conclusions

In this paper, we discussed the capability of the AFM as a reliable force sensor for the study of biological systems. The representative results presented here demonstrate the possibility of using AFM nanomechanical measurements to characterize physical modifications related to specific physio-pathological conditions of cells and tissues.

As demonstrated in this work, as well as in many others [36,86–89], AFM can be used to test biological samples at several different scales, in terms of dimensions and forces, from large, rough, and relatively stiff ECMs and tissues, passing through smaller and soft cells, to extremely compliant pericellular brushes. Here, in particular, we reported on the capabilities of the instrument to characterize the mechanical differences of urothelium bladder cancer cells and the different organization of their glycocalyx brushes using the same mechanical data sets. At a larger scale, the stiffening of human-derived ECM during the progression of colorectal carcinoma could be detected.

The crosstalk between cells and their microenvironment is complex and challenging to quantitatively assess; the reliability of AFM also stands in its flexibility of measurements, which is demonstrated by the capability of AFM to both sense and apply forces in aqueous physiological conditions with controlled temperature, as well as by the possibility of resolving the measurements not only spatially, but also in the time and frequency domains; this makes the tracking by AFM of dynamic biological processes possible, including monitoring cell mechanical changes through cytoskeleton rearrangement, for example, due to drug actions or genetic modifications [77,90].

AFM and AFM-inspired instruments will likely play an increasingly important role in establishing experimental approaches for the mechanical phenotyping of cells and tissues in health and disease conditions, with the potential to develop effective early diagnostic tools based on biomechanical measurements.

Author Contributions: Conceptualization, A.P. and M.G. (Manuela Gariboldi); Methodology—Cell culture and preparation, H.H. and C.S.; Methodology—ECM preparation, E.L., L.V., M.G.1, M.D. and M.G. (Marcello Guaglio); Methodology—Mechanics of ECM, E.L. and M.C.; Methodology—Mechanics of cells and glycocalyx characterization, H.H. and M.C.; Original draft writing, H.H., E.L., M.C. and A.P.; Draft reviewing and editing: H.H., E.L., M.C., C.S. and A.P.; Data curation and analysis: H.H., E.L., M.C. and A.P.; Supervision, M.G. (Manuela Gariboldi), L.V., M.C. and A.P.; Resources, funding and project administration, A.P., M.G. (Manuela Gariboldi) and M.D. All authors have read and agreed to the published version of the manuscript.

Funding: This research was funded by the European Union's Horizon 2020 research and innovation program under the Marie Skłodowska-Curie grant agreement No. 812772, project Phys2Biomed, and under FET Open grant agreement No. 801126, project EDIT. We acknowledge the support of Istituto Nazionale dei Tumori (5‰ fund).

Institutional Review Board Statement: The study was conducted according to the guidelines of the Declaration of Helsinki 2009 and approved by the Institutional Review Board (249/19). Written informed consent was acquired.

Informed Consent Statement: Informed consent was obtained from all subjects involved in the study.

Data Availability Statement: The data presented in this study are available on reasonable request from the corresponding author.

Acknowledgments: We thank Massimo Alfano (San Raffaele Hospital, Milano) for kindly providing the bladder cancer cell lines used in this study. We thank the patients who participated in the study. This research was funded by the European Union's Horizon 2020 research and innovation program under the Marie Skłodowska-Curie grant agreement No. 812772, project Phys2Biomed, and under FET Open grant agreement No. 801126, project EDIT. We acknowledge the support of Istituto Nazionale dei Tumori (funds obtained through an Italian law that allows taxpayers to allocate 0.5 percent of their tax to a research institution of their choice).

Conflicts of Interest: The authors declare no conflict of interest.

References

1. Frantz, C.; Stewart, K.M.; Weaver, V.M. The Extracellular Matrix at a Glance. *J. Cell Sci.* **2010**, *123*, 4195–4200. [CrossRef] [PubMed]
2. Cox, T.R. The Matrix in Cancer. *Nat. Rev. Cancer* **2021**, *21*, 217–238. [CrossRef] [PubMed]
3. Winkler, J.; Abisoye-Ogunniyan, A.; Metcalf, K.J.; Werb, Z. Concepts of Extracellular Matrix Remodelling in Tumour Progression and Metastasis. *Nat. Commun.* **2020**, *11*, 5120. [CrossRef] [PubMed]
4. Engler, A.J.; Sen, S.; Sweeney, H.L.; Discher, D.E. Matrix Elasticity Directs Stem Cell Lineage Specification. *Cell* **2006**, *126*, 677–689. [CrossRef] [PubMed]
5. Nebuloni, M.; Albarello, L.; Andolfo, A.; Magagnotti, C.; Genovese, L.; Locatelli, I.; Tonon, G.; Longhi, E.; Zerbi, P.; Allevi, R.; et al. Insight on Colorectal Carcinoma Infiltration by Studying Perilesional Extracellular Matrix. *Sci. Rep.* **2016**, *6*, 22522. [CrossRef]
6. Lu, P.; Weaver, V.M.; Werb, Z. The Extracellular Matrix: A Dynamic Niche in Cancer Progression. *J. Cell Biol.* **2012**, *196*, 395–406. [CrossRef]
7. Babu, P.K.V.; Radmacher, M. Mechanics of Brain Tissues Studied by Atomic Force Microscopy: A Perspective. *Front. Neurosci.* **2019**, *13*, 600. [CrossRef]
8. Muiznieks, L.D.; Keeley, F.W. Molecular Assembly and Mechanical Properties of the Extracellular Matrix: A Fibrous Protein Perspective. *Biochim. Biophys. Acta Mol. Basis Dis.* **2013**, *1832*, 866–875. [CrossRef]
9. Najafi, M.; Farhood, B.; Mortezaee, K. Extracellular Matrix (ECM) Stiffness and Degradation as Cancer Drivers. *J. Cell. Biochem.* **2019**, *120*, 2782–2790. [CrossRef]
10. Oxnard, G.R. The Cellular Origins of Drug Resistance in Cancer. *Nat. Med.* **2016**, *22*, 232–234. [CrossRef]
11. Giroldi, L.A.; Bringuier, P.-P.; Shimazui, T.; Jansen, K.; Schalken, J.A. Changes in Cadherins-Catenin Complexes in the Progression of Human Bladder Carcinoma. *J. Cancer* **1999**, *82*, 70–76. [CrossRef]
12. Yeh, Y.-T.; Hur, S.S.; Chang, J.; Wang, K.-C.; Chiu, J.-J.; Li, Y.-S.; Chien, S. Matrix Stiffness Regulates Endothelial Cell Proliferation through Septin 9. *PLoS ONE* **2012**, *7*, e46889. [CrossRef] [PubMed]
13. Jaalouk, D.E.; Lammerding, J. Mechanotransduction Gone Awry. *Nat. Rev. Mol. Cell Biol.* **2009**, *10*, 63–73. [CrossRef] [PubMed]
14. Bissell, M.J.; Hines, W.C. Why Don't We Get More Cancer? A Proposed Role of the Microenvironment in Restraining Cancer Progression. *Nat. Med.* **2011**, *17*, 320–329. [CrossRef] [PubMed]
15. Chaudhuri, O.; Koshy, S.T.; Branco Da Cunha, C.; Shin, J.W.; Verbeke, C.S.; Allison, K.H.; Mooney, D.J. Extracellular Matrix Stiffness and Composition Jointly Regulate the Induction of Malignant Phenotypes in Mammary Epithelium. *Nat. Mater.* **2014**, *13*, 970–978. [CrossRef] [PubMed]
16. Alberts, B. *Essential Cell Biology*, 2nd ed.; Garland Science Pub.: New York, NY, USA, 1998; Volume 51, ISBN 9780815334804.
17. Lansky, Z.; Mutsafi, Y.; Houben, L.; Ilani, T.; Armony, G.; Wolf, S.G.; Fass, D. 3D Mapping of Native Extracellular Matrix Reveals Cellular Responses to the Microenvironment. *J. Struct. Biol. X* **2019**, *1*, 100002. [CrossRef]
18. Alcaraz, J.; Otero, J.; Jorba, I.; Navajas, D. Bidirectional Mechanobiology between Cells and Their Local Extracellular Matrix Probed by Atomic Force Microscopy. *Semin. Cell Dev. Biol.* **2018**, *73*, 71–81. [CrossRef]
19. Liu, H.; Wen, J.; Xiao, Y.; Liu, J.; Hopyan, S.; Radisic, M.; Simmons, C.A.; Sun, Y. In Situ Mechanical Characterization of the Cell Nucleus by Atomic Force Microscopy. *ACS Nano* **2014**, *8*, 3821–3828. [CrossRef]
20. Gao, L.; Lipowsky, H.H. Composition of the Endothelial Glycocalyx and Its Relation to Its Thickness and Diffusion of Small Solutes. *Microvasc. Res.* **2010**, *80*, 394–401. [CrossRef]
21. Chighizola, F.M.; Dini, T.; Marcotti, S.; Urso, M.D.; Piazzoni, C.; Borghi, F.; Previdi, A.; Ceriani, L.; Folliero, C.; Stramer, B.; et al. The glycocalyx affects the mechanotransductive perception of the topographical microenvironment. *bioRxiv* **2022**. [CrossRef]
22. Fu, B.M.; Tarbell, J.M. Mechano-Sensing and Transduction by Endothelial Surface Glycocalyx: Composition, Structure, and Function. *Wiley Interdiscip. Rev. Syst. Biol. Med.* **2013**, *5*, 381–390. [CrossRef] [PubMed]
23. Kechagia, J.Z.; Ivaska, J.; Roca-Cusachs, P. Integrins as Biomechanical Sensors of the Microenvironment. *Nat. Rev. Mol. Cell Biol.* **2019**, *20*, 457–473. [CrossRef] [PubMed]
24. Paszek, M.J.; Boettiger, D.; Weaver, V.M.; Hammer, D.A. Integrin Clustering Is Driven by Mechanical Resistance from the Glycocalyx and the Substrate. *PLoS Comput. Biol.* **2009**, *5*, e1000604. [CrossRef]
25. Paszek, M.J.; Dufort, C.C.; Rossier, O.; Bainer, R.; Mouw, J.K.; Godula, K.; Hudak, J.E.; Lakins, J.N.; Wijekoon, A.C.; Cassereau, L.; et al. The Cancer Glycocalyx Mechanically Primes Integrin-Mediated Growth and Survival. *Nature* **2014**, *511*, 319–325. [CrossRef] [PubMed]
26. Cosgun, Z.C.; Fels, B.; Kusche-Vihrog, K. Nanomechanics of the Endothelial Glycocalyx: From Structure to Function. *Am. J. Pathol.* **2020**, *190*, 732–741. [CrossRef] [PubMed]
27. Iyer, S.; Gaikwad, R.M.; Subba-Rao, V.; Woodworth, C.D.; Sokolov, I. Atomic Force Microscopy Detects Differences in the Surface Brush of Normal and Cancerous Cells. *Nat. Nanotechnol.* **2009**, *4*, 389–393. [CrossRef] [PubMed]
28. Schmidt, S.; Weigelin, B.; te Riet, J.; te Boekhorst, V.; te Lindert, M.; Wijers-Rouw, M.; Lelli, B.; Rognoni, L.; Krause-Vortmeyer, M.; Messent, A.; et al. Glycocalyx-Mediated Cell Adhesion and Migration. *bioRxiv* **2022**. [CrossRef]
29. Kuo, J.C.-H.; Gandhi, J.G.; Zia, R.N.; Paszek, M.J. Physical Biology of the Cancer Cell Glycocalyx. *Nat. Phys.* **2018**, *14*, 658–669. [CrossRef]
30. Buffone, A.; Weaver, V.M. Don't Sugarcoat It: How Glycocalyx Composition Influences Cancer Progression. *J. Cell Biol.* **2020**, *219*. [CrossRef]

31. Sokolov, I.; Iyer, S.; Subba-Rao, V.; Gaikwad, R.M.; Woodworth, C.D. Detection of Surface Brush on Biological Cells in Vitro with Atomic Force Microscopy. *Appl. Phys. Lett.* **2007**, *91*, 023902. [CrossRef]
32. Tarbell, J.M.; Cancel, L.M. The Glycocalyx and Its Significance in Human Medicine. *J. Intern. Med.* **2016**, *280*, 97–113. [CrossRef] [PubMed]
33. Mitchell, M.J.; King, M.R. Physical Biology in Cancer. 3. The Role of Cell Glycocalyx in Vascular Transport of Circulating Tumor Cells. *Am. J. Physiol. Cell Physiol.* **2014**, *306*, C89–C97. [CrossRef] [PubMed]
34. Qi, S.; Yi, C.; Yang, M. Biosensors Using Atomic Force Microscopes. In *Encyclopedia of Microfluidics and Nanofluidics*; Springer US: Boston, MA, USA, 2008; pp. 106–114.
35. Zhou, G.; Zhang, B.; Tang, G.; Yu, X.F.; Galluzzi, M. Cells Nanomechanics by Atomic Force Microscopy: Focus on Interactions at Nanoscale. *Adv. Phys. X* **2021**, *6*, 1866668. [CrossRef]
36. Alessandrini, A.; Facci, P. AFM: A Versatile Tool in Biophysics. *Meas. Sci. Technol.* **2005**, *16*, R65–R92. [CrossRef]
37. Müller, D.J.; Dumitru, A.C.; lo Giudice, C.; Gaub, H.E.; Hinterdorfer, P.; Hummer, G.; de Yoreo, J.J.; Dufrêne, Y.F.; Alsteens, D. Atomic Force Microscopy-Based Force Spectroscopy and Multiparametric Imaging of Biomolecular and Cellular Systems. *Chem. Rev.* **2021**, *121*, 11701–11725. [CrossRef]
38. Alexander, S.; Hellemans, L.; Marti, O.; Schneir, J.; Elings, V.; Hansma, P.K.; Longmire, M.; Gurley, J. An Atomic-resolution Atomic-force Microscope Implemented Using an Optical Lever. *J. Appl. Phys.* **1998**, *65*, 164–167. [CrossRef]
39. Meyer, G.; Amer, N.M. Optical-Beam-Deflection Atomic Force Microscopy: The NaCl (001) Surface. *Appl. Phys. Lett.* **1990**, *56*, 2100–2101. [CrossRef]
40. Putman, C.A.J.; de Grooth, B.G.; van Hulst, N.F.; Greve, J. A Theoretical Comparison between Interferometric and Optical Beam Deflection Technique for the Measurement of Cantilever Displacement in AFM. *Ultramicroscopy* **1992**, *42*, 1509–1513. [CrossRef]
41. Erlandsson, R.; McClelland, G.M.; Mate, C.M.; Chiang, S. Atomic Force Microscopy Using Optical Interferometry. *J. Vac. Sci. Technol. A Vac. Surf. Film.* **1988**, *6*, 266–270. [CrossRef]
42. Chighizola, M.; Puricelli, L.; Bellon, L.; Podestà, A. Large Colloidal Probes for Atomic Force Microscopy: Fabrication and Calibration Issues. *J. Mol. Recognit.* **2021**, *34*, e2879. [CrossRef]
43. Butt, H.J.; Jaschke, M. Calculation of Thermal Noise in Atomic Force Microscopy. *Nanotechnology* **1995**, *6*, 1. [CrossRef]
44. Hutter, J.L.; Bechhoefer, J. Calibration of Atomic-Force Microscope Tips. *Rev. Sci. Instrum.* **1993**, *64*, 1868–1873. [CrossRef]
45. Viani, M.B.; Schäffer, T.E.; Chand, A.; Rief, M.; Gaub, H.E.; Hansma, P.K. Small Cantilevers for Force Spectroscopy of Single Molecules. *J. Appl. Phys.* **1999**, *86*, 2258–2262. [CrossRef]
46. Smith, D.P.E. Limits of Force Microscopy. *Rev. Sci. Instrum.* **1995**, *66*, 3191–3195. [CrossRef]
47. Butt, H.J.; Cappella, B.; Kappl, M. Force Measurements with the Atomic Force Microscope: Technique, Interpretation and Applications. *Surf. Sci. Rep.* **2005**, *59*, 1–152. [CrossRef]
48. Genovese, L.; Zawada, L.; Tosoni, A.; Ferri, A.; Zerbi, P.; Allevi, R.; Nebuloni, M.; Alfano, M. Cellular Localization, Invasion, and Turnover Are Differently Influenced by Healthy and Tumor-Derived Extracellular Matrix. *Tissue Eng. Part A* **2014**, *20*, 2005–2018. [CrossRef]
49. Varinelli, L.; Guaglio, M.; Brich, S.; Zanutto, S.; Belfiore, A.; Zanardi, F.; Iannelli, F.; Oldani, A.; Costa, E.; Chighizola, M.; et al. Decellularized Normal and Tumor Extracellular Matrix as Scaffold for Cancer Organoid Cultures of Colorectal Peritoneal Metastases. *bioRxiv* **2021**. [CrossRef]
50. Franks, L.M.; Rigby, C.; Nelson-Rees, W.A. HeLa Cells and RT4 Cells. *Science* **1975**, *188*, 168. [CrossRef]
51. Bubeník, J.; Barešová, M.; Viklický, V.; Jakoubková, J.; Sainerová, H.; Donner, J. Established Cell Line of Urinary Bladder Carcinoma (T24) Containing Tumour-specific Antigen. *Int. J. Cancer* **1973**, *11*, 765–773. [CrossRef]
52. Indrieri, M.; Podestà, A.; Bongiorno, G.; Marchesi, D.; Milani, P. Adhesive-Free Colloidal Probes for Nanoscale Force Measurements: Production and Characterization. *Rev. Sci. Instrum.* **2011**, *82*, 023708. [CrossRef]
53. Kontomaris, S.-V. The Hertz Model in AFM Nanoindentation Experiments: Applications in Biological Samples and Biomaterials. *Micro Nanosyst.* **2018**, *10*, 11–22. [CrossRef]
54. Hertz, H. Ueber Die Berührung Fester Elastischer Körper. *J. Fur Die Reine Angew. Math.* **1881**, *1881*, 156–171. [CrossRef]
55. Puricelli, L.; Galluzzi, M.; Schulte, C.; Podestà, A.; Milani, P. Nanomechanical and Topographical Imaging of Living Cells by Atomic Force Microscopy with Colloidal Probes. *Rev. Sci. Instrum.* **2015**, *86*, 33705. [CrossRef] [PubMed]
56. Gavara, N. Combined Strategies for Optimal Detection of the Contact Point in AFM Force-Indentation Curves Obtained on Thin Samples and Adherent Cells. *Sci. Rep.* **2016**, *6*, 1–13. [CrossRef] [PubMed]
57. Laurent, J.; Steinberger, A.; Bellon, L. Functionalized AFM Probes for Force Spectroscopy: Eigenmode Shapes and Stiffness Calibration through Thermal Noise Measurements. *Nanotechnology* **2013**, *24*, 225504. [CrossRef] [PubMed]
58. Schillers, H.; Rianna, C.; Schäpe, J.; Luque, T.; Doschke, H.; Wälte, M.; Uriarte, J.J.; Campillo, N.; Michanetzis, G.P.A.; Bobrowska, J.; et al. Standardized Nanomechanical Atomic Force Microscopy Procedure (SNAP) for Measuring Soft and Biological Samples. *Sci. Rep.* **2017**, *7*, 5117. [CrossRef]
59. Dimitriadis, E.K.; Horkay, F.; Maresca, J.; Kachar, B.; Chadwick, R.S. Determination of Elastic Moduli of Thin Layers of Soft Material Using the Atomic Force Microscope. *Biophys. J.* **2002**, *82*, 2798–2810. [CrossRef]

60. Garcia, P.D.; Garcia, R. Determination of the Elastic Moduli of a Single Cell Cultured on a Rigid Support by Force Microscopy. *Biophys. J.* **2018**, *114*, 2923–2932. [CrossRef]
61. Gavara, N.; Chadwick, R.S. Determination of the Elastic Moduli of Thin Samples and Adherent Cells Using Conical Atomic Force Microscope Tips. *Nat. Nanotechnol.* **2012**, *7*, 733–736. [CrossRef]
62. Kubiak, A.; Chighizola, M.; Schulte, C.; Bryniarska, N.; Wesolowska, J.; Pudelek, M.; Lasota, M.; Ryszawy, D.; Basta-Kaim, A.; Laidler, P.; et al. Stiffening of DU145 Prostate Cancer Cells Driven by Actin Filaments-Microtubule Crosstalk Conferring Resistance to Microtubule-Targeting Drugs. *Nanoscale* **2021**, *13*, 6212–6226. [CrossRef]
63. Giergiel, M.; Malek-Zietek, K.E.; Konior, J.; Targosz-Korecka, M. Endothelial Glycocalyx Detection and Characterization by Means of Atomic Force Spectroscopy: Comparison of Various Data Analysis Approaches. *Micron* **2021**, *151*, 103153. [CrossRef] [PubMed]
64. Dokukin, M.; Ablaeva, Y.; Kalaparthi, V.; Seluanov, A.; Gorbunova, V.; Sokolov, I. Pericellular Brush and Mechanics of Guinea Pig Fibroblast Cells Studied with AFM. *Biophys. J.* **2016**, *111*, 236–246. [CrossRef] [PubMed]
65. Dokukin, M.E.; Kuroki, H.; Minko, S.; Sokolov, I. AFM Study of Polymer Brush Grafted to Deformable Surfaces: Quantitative Properties of the Brush and Substrate Mechanics. *Macromolecules* **2017**, *50*, 275–282. [CrossRef]
66. Sokolov, I.; Dokukin, M.E.; Guz, N.V. Method for Quantitative Measurements of the Elastic Modulus of Biological Cells in AFM Indentation Experiments. *Methods* **2013**, *60*, 202–213. [CrossRef]
67. Alper, J.S.; Gelb, R.I. Standard Errors and Confidence Intervals in Nonlinear Regression: Comparison of Monte Carlo and Parametric Statistics. *J. Phys. Chem.* **1990**, *94*, 4747–4751. [CrossRef]
68. Viji Babu, P.K.; Rianna, C.; Mirastschijski, U.; Radmacher, M. Nano-Mechanical Mapping of Interdependent Cell and ECM Mechanics by AFM Force Spectroscopy. *Sci. Rep.* **2019**, *9*, 1–19. [CrossRef]
69. Jorba, I.; Beltrán, G.; Falcones, B.; Suki, B.; Farré, R.; García-Aznar, J.M.; Navajas, D. Nonlinear Elasticity of the Lung Extracellular Microenvironment Is Regulated by Macroscale Tissue Strain. *Acta Biomater.* **2019**, *92*, 265–276. [CrossRef]
70. Jorba, I.; Uriarte, J.J.; Campillo, N.; Farré, R.; Navajas, D. Probing Micromechanical Properties of the Extracellular Matrix of Soft Tissues by Atomic Force Microscopy. *J. Cell. Physiol.* **2017**, *232*, 19–26. [CrossRef]
71. Luque, T.; Melo, E.; Garreta, E.; Cortiella, J.; Nichols, J.; Farré, R.; Navajas, D. Local Micromechanical Properties of Decellularized Lung Scaffolds Measured with Atomic Force Microscopy. *Acta Biomater.* **2013**, *9*, 6852–6859. [CrossRef]
72. Liu, F.; Mih, J.D.; Shea, B.S.; Kho, A.T.; Sharif, A.S.; Tager, A.M.; Tschumperlin, D.J. Feedback Amplification of Fibrosis through Matrix Stiffening and COX-2 Suppression. *J. Cell Biol.* **2010**, *190*, 693–706. [CrossRef]
73. Limpert, E.; Stahel, W.A. Problems with Using the Normal Distribution—and Ways to Improve Quality and Efficiency of Data Analysis. *PLoS ONE* **2011**, *6*, e21403. [CrossRef] [PubMed]
74. Deville, S.S.; Cordes, N. The Extracellular, Cellular, and Nuclear Stiffness, a Trinity in the Cancer Resistome—A Review. *Front. Oncol.* **2019**, *9*, 1376. [CrossRef] [PubMed]
75. Grasset, E.M.; Bertero, T.; Bozec, A.; Friard, J.; Bourget, I.; Pisano, S.; Lecacheur, M.; Maiel, M.; Bailleux, C.; Emelyanov, A.; et al. Matrix Stiffening and EGFR Cooperate to Promote the Collective Invasion of Cancer Cells. *Cancer Res.* **2018**, *78*, 5229–5242. [CrossRef] [PubMed]
76. Handorf, A.M.; Zhou, Y.; Halanski, M.A.; Li, W.J. Tissue Stiffness Dictates Development, Homeostasis, and Disease Progression. *Organogenesis* **2015**, *11*, 1–15. [CrossRef] [PubMed]
77. Rotsch, C.; Radmacher, M. Drug-Induced Changes of Cytoskeletal Structure and Mechanics in Fibroblasts: An Atomic Force Microscopy Study. *Biophys. J.* **2000**, *78*, 520–535. [CrossRef]
78. Liu, H.; Tan, Q.; Geddie, W.R.; Jewett, M.A.S.; Phillips, N.; Ke, D.; Simmons, C.A.; Sun, Y. Biophysical Characterization of Bladder Cancer Cells with Different Metastatic Potential. *Cell Biochem. Biophys.* **2014**, *68*, 241–246. [CrossRef]
79. Tang, G.; Galluzzi, M.; Zhang, B.; Shen, Y.-L.L.; Stadler, F.J. Biomechanical Heterogeneity of Living Cells: Comparison between Atomic Force Microscopy and Finite Element Simulation. *Langmuir* **2019**, *35*, 7578–7587. [CrossRef]
80. Ramos, J.R.; Pabijan, J.; Garcia, R.; Lekka, M. The Softening of Human Bladder Cancer Cells Happens at an Early Stage of the Malignancy Process. *Beilstein J. Nanotechnol.* **2014**, *5*, 447–457. [CrossRef]
81. Xu, W.; Mezencev, R.; Kim, B.; Wang, L.; McDonald, J.; Sulchek, T. Cell Stiffness Is a Biomarker of the Metastatic Potential of Ovarian Cancer Cells. *PLoS ONE* **2012**, *7*, 46609. [CrossRef]
82. Cross, S.E.; Jin, Y.S.; Rao, J.; Gimzewski, J.K. Nanomechanical Analysis of Cells from Cancer Patients. *Nat. Nanotechnol.* **2007**, *2*, 780–783. [CrossRef]
83. Plodinec, M.; Loparic, M.; Monnier, C.A.; Obermann, E.C.; Zanetti-Dallenbach, R.; Oertle, P.; Hyotyla, J.T.; Aebi, U.; Bentires-Alj, M.; Lim, R.Y.H.; et al. The Nanomechanical Signature of Breast Cancer. *Nat. Nanotechnol.* **2012**, *7*, 757–765. [CrossRef] [PubMed]
84. Mialhe, A.; Levacher, G.; Champelovier, P.; Martel, V.; Serres, M.; Knudsen, K.; Seigneurin, D. Expression of E-, P-, N-Cadherins and Catenins in Human Bladder Carcinoma Cell Lines. *J. Urol.* **2000**, *164*, 826–835. [CrossRef]
85. Oberleithner, H.; Peters, W.; Kusche-Vihrog, K.; Korte, S.; Schillers, H.; Kliche, K.; Oberleithner, K. Salt Overload Damages the Glycocalyx Sodium Barrier of Vascular Endothelium. *Pflug. Arch. Eur. J. Physiol.* **2011**, *462*, 519–528. [CrossRef] [PubMed]
86. Gould, S.A.C.; Drake, B.; Prater, C.B.; Weisenhorn, A.L.; Manne, S.; Kelderman, G.L.; Butt, H.J.; Hansma, H.; Hansma, P.K.; Magonov, S.; et al. The Atomic Force Microscope: A Tool for Science and Industry. *Ultramicroscopy* **1990**, *33*, 93–98. [CrossRef]
87. Müller, D.J.; Dufrêne, Y.F. Atomic Force Microscopy as a Multifunctional Molecular Toolbox in Nanobiotechnology. *Nanosci. Technol. A Collect. Rev. Nat. J.* **2008**, *3*, 261–269. [CrossRef]

88. Krieg, M.; Fläschner, G.; Alsteens, D.; Gaub, B.M.; Roos, W.H.; Wuite, G.J.L.; Gaub, H.E.; Gerber, C.; Dufrêne, Y.F.; Müller, D.J. Atomic Force Microscopy-Based Mechanobiology. *Nat. Rev. Phys.* **2019**, *1*, 41–57. [CrossRef]
89. Li, M.; Dang, D.; Liu, L.; Xi, N.; Wang, Y. Atomic Force Microscopy in Characterizing Cell Mechanics for Biomedical Applications: A Review. *IEEE Trans. Nanobioscience* **2017**, *16*, 523–540. [CrossRef]
90. Lamontagne, C.-A.; Cuerrier, C.M.; Grandbois, M. AFM as a Tool to Probe and Manipulate Cellular Processes. *Pflügers Arch. Eur. J. Physiol.* **2008**, *456*, 61–70. [CrossRef]

1.6. PhD project and objectives of the thesis

This thesis project has been carried out within a Marie-Skłodowska Curie ITN project called Phys2BioMed, which focuses on providing advanced and innovative tools for early diagnosis by means of Atomic Force Microscopy AFM and correlative techniques. As it is proven that in the context of cancer the mechanical properties of the biological samples, such as cells or tissues, are giving insight into many physiological and pathological processes [43], the project aimed at looking for mechanical fingerprints of diseases.

As presented above, the inter-relation of cells with their microenvironment in healthy or tumoral conditions is complex and its study is difficult. Atomic Force Microscopy was demonstrated to be, in combination with other techniques, a valuable technique for the investigation of the physical properties of cells and biological systems.

The main aim of this thesis is the study of the interaction and mutual influences of cells and their microenvironment, both in healthy and tumoral conditions, employing of Atomic Force Microscopy. We focused on adhesion force spectroscopy by AFM as the main experimental approach to unravel the integrin-related adhesive mechanisms that characterize the cell-ECM interaction. This work has been carried out in collaboration with clinical partners (Ospedale San Raffaele, OSR, Milano, Dr. Alfano Massimo, and Istituto Europeo di Oncologia, IEO, Milano, Dr. Giuseppe Diaferia), who provided both samples and models for the analysis and appropriate methodology to develop our force spectroscopy approach, besides fundamental expertise in cellular biology and medicine. This work has benefited from continuous discussion and collaboration with partners of the Phys2BioMed network, in particular during scientific secondments in the laboratories of prof. M. Radmacher lab, Institute of Biophysics, University of Bremen, Bremen, Germany, and of Prof. C. Franz, NanoLSI, University of Kanazawa, Kanazawa, Japan, for cell-cell force spectroscopy experiments, and Dr. B. Walter, VMicro SAS, Lille, France, for AFM cantilever calibration.

As the target of our study, we concentrated mostly on bladder cancer with the use of cell models and decellularized matrices from the murine bladder (produced at OSR).

The main objectives of this thesis work are:

- The development of a method for AFM force spectroscopy to move the research of cell-microenvironment interaction one step closer to physiological conditions, by the attachment of native ECM directly to AFM probes. Our goal is to develop a tool for personalized medicine that can potentially use in clinics for early diagnosis. We aim at elaborating a reproducible, reliable and straightforward procedure that would operate with direct sample, ECM and/or cells, from patient. This development may open new possibilities for using AFM for biosensing.

- The functionalisation of custom colloidal probes with ECM proteins to have insights into the change of integrin-related adhesion between cells and the matrix in the particular context of bladder carcinoma evolution, for the promotion of epithelial to mesenchymal transition.

- The improvement of calibration of AFM cantilevers by comparison of three main methods: AFM thermal noise, Sader, and Laser Doppler vibrometer. The aim is to

evaluate a robust protocol in the order to use the AFM for the characterisation of cell-microenvironment interactions in the most reliable and reproducible way.

- The contribution of the network activities within the project Phys2BioMed in which we aimed at standardising mechanical measurements of pancreatic cells PANC-1 and of bladder cancer tissues. Our objective was also the development of a new protocol for faster acquisition and analysis of data.

- Finally, as the cell microenvironment not only consists of the extracellular matrix but also other cells, we will investigate the cadherin switch in the framework of bladder carcinoma, with two extreme grades of invasiveness cells.

1.7. Thesis outline

The Introduction presents the topic of the cell and the microenvironment interactions in the context of both health and disease. It also presents an overview of the applications of AFM in the field of nanomechanics supported by original results, on cells and tissues, in the form of a paper recently published in Sensor journal by H. Holuigue et al.[85]

Chapter 1 reports on improving the calibration procedures of tipless AFM cantilevers and custom colloidal probes in the scope of using them for Adhesion Force Spectroscopy experiments. For those experiments, the calibration of the force sensor is a key aspect to perform reliable and reproducible measurements.

In Chapter 2, the results of a force spectroscopy study of the interaction of bladder cancer cells with bladder ECM are presented. This work is based on the functionalization of custom colloidal probes with two types of ECM proteins (laminin and fibronectin).

Chapter 3 represents the core of my research and reports on the development and application of novel native ECM probes to study cell-microenvironment interaction using AFM in adhesion force spectroscopy mode.

Conclusion and perspectives briefly summarize the obtained results and discuss potential improvements and future experiments.

In Appendix A, the bottom effect correction method in the study of cell mechanics is presented as well as the development of an improved approach for its implementation in the context of confluent monolayers of cells, where the reference substrate is not available in the maps.

Appendix B describes some preliminary results in the study of cell-cell interactions among bladder cancer cells through cell-cell force spectroscopy. This work was done in collaboration with both the University of Bremen, Institute of Biophysics, Germany (Prof. M. Radmacher) and NanoLSI, University of Kanazawa, Japan (Prof. C. Franz).

2. General Material and Methods

2.1. Atomic force microscopy equipment

Experiments at the University of Milan have been performed using a Bioscope Catalyst AFM (Bruker) (**Figure 14**), mounted on top of an inverted optical microscope (Olympus X71). The whole system was isolated from the noise using an anti-vibration active base (DVIA-T45, Daeil Systems) and an acoustic box (Schaefer, Italy).

The precise alignment of AFM and optical images were possible using the Bruker MIRO software, allowing choosing the regions of interest for both matrices and cells. For living cells' measurements, cells were kept in a petri dish with phenol red-free medium at 37°C in a perfusion stage incubator governed by a temperature controller (Lakeshore 331). Measurements on ECMs were performed at room temperature in a droplet of PBS confined on the glass slide within a circle of hydrophobic ink drawn using a hydrophobic pen (Sigma).

Experiments performed at the University of Kanazawa were performed with a CellHesion 200 (Bruker) module allowing a z-range of 100µm installed on a Nanowizard II AFM (JPK) equipped with a BioCell (Bruker) heating stage (**Figure 15**).

Experiments performed at the University of Bremen were performed with an MFP-3D-Bio AFM (Asylum Research). Measurements on living cells were performed at room temperature in a petri-dish couple to a homemade setup for CO_2 addition during measurements (5% of CO_2).

Appendix A presents cell-cell experiments performed with two different AFM setups: the Nanowizard II (JPK) and MFP-3D-Bio AFM (Asylum Research). Principally temperature control was preferred while performing biological experiments, nevertheless, some cells such as T24 (bladder cancer, grade 3) were found to be quite resistant while performing AFM without control of temperature.

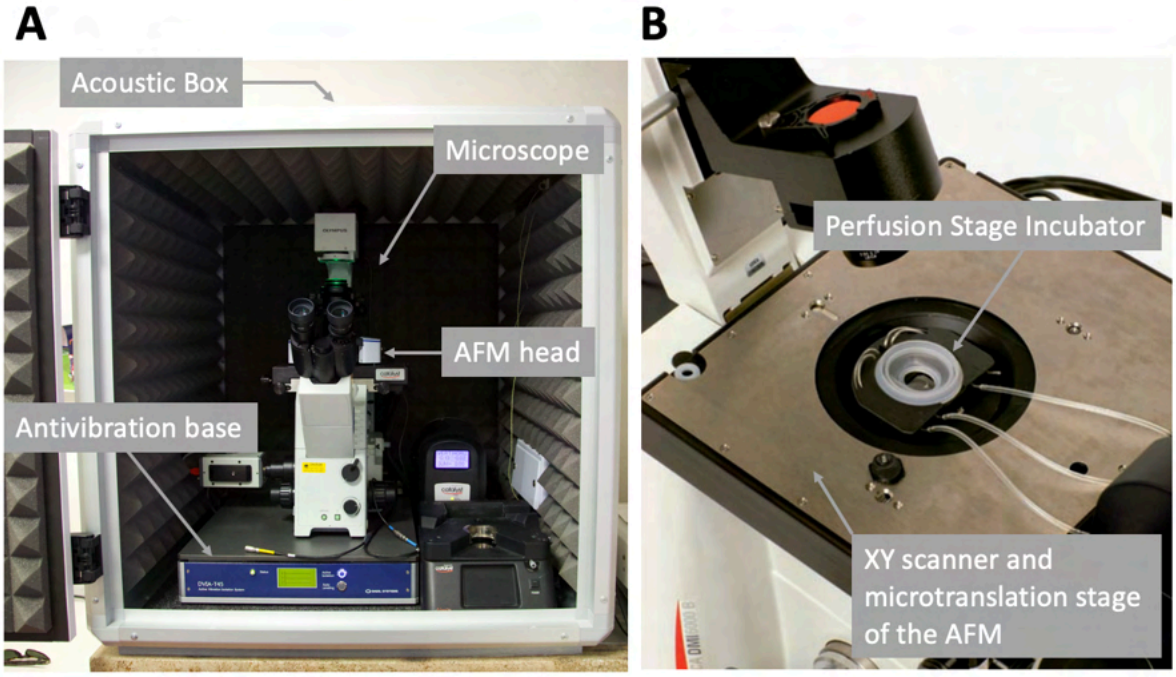

Figure 14. (A) Picture of the AFM setup. Catalyst AFM with its optical microscope and antivibration base inside the acoustic box, and (B) Perfusion stage incubator on the XY scanner and microtranslation stage of the AFM.

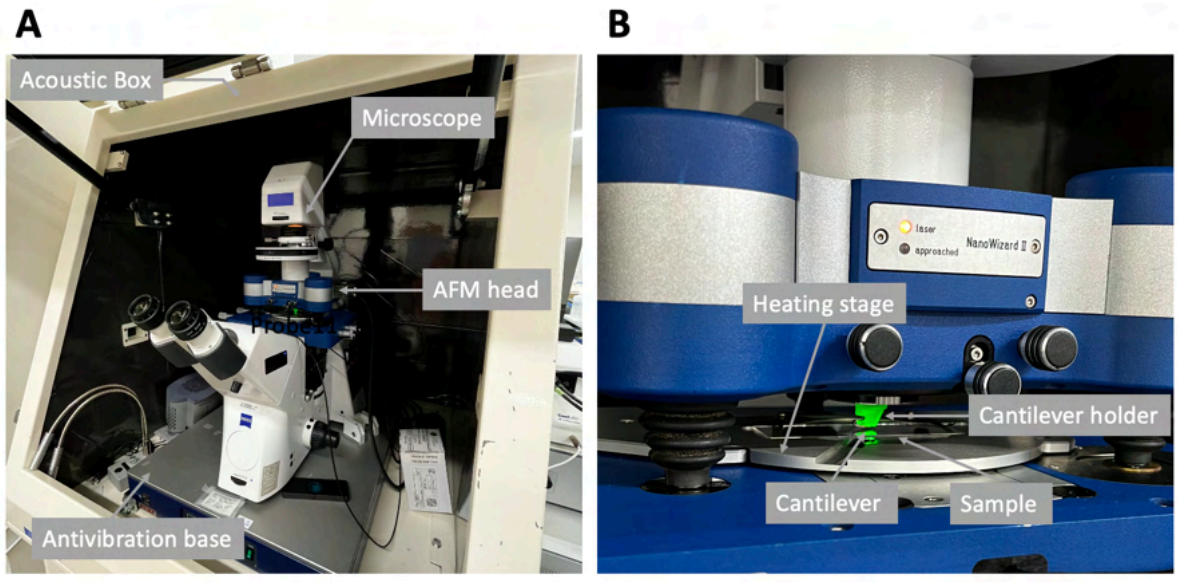

Figure 15. (A) Picture of the AFM setup at NanoLSI, Kanazawa, Japan. Nanowizard II AFM with its optical microscope and antivibration base inside the acoustic box, and (B) close-up of the AFM head with CellHesion module on top of a sample placed on a glass slide with the heating stage.

2.1.1. Production and calibration of colloidal probes

Homemade colloidal probes (CPs), as presented in **Figure 16**, were produced by attaching borosilicate glass spheres to non-coated tipless cantilevers (MikroMasch HQ:CSC38/Tipless/NoAl or NanoandMore TL-FM), following the protocol developed by Indrieri

et al. [111,112]. Glass beads placed on gold-coated glass slides (to minimize capillary adhesion) were captured using the AFM XYZ microtranslation stage and the optical microscope (**Figure 14**) at the end of tipless cantilevers, previously dipped in Vaseline for easier capture. The newly created cantilever-microsphere assemblies are then placed in an oven at 780°C, the softening temperature of borosilicate glass, to allow the firm covalent attachment of the sphere to the cantilever.

One of the main advantages of CPs is their larger contact area that induces less stress and strain compared to sharp tips, making it advantageous in the case of studying biological samples like cells and tissues. Their well-defined and characterized geometry contributes to a clear application of the analytical model of a sphere indentation on a flat surface. Providing a higher signal-to-noise ratio, CPs are widely used for adhesion force spectroscopy experiments[21,105,113,114] also, for their easy functionalization and cleaning[115]. Regarding the drawbacks of those probes, while their radius can be easily characterized by reversed AFM[111], this additional spherical mass can induce modification of the dynamic of the cantilever and reduce the accuracy of the spring constant calibration[112]. With larger probes comes the need for bottom-effect correction, the CPs sense the effect of the hard substrate underneath during the indentation of thin and soft samples, such as biological ones [116–118]. Both of those aspects are discussed in Chapter 1 and Appendix A respectively.

The calibration of the spring constant of the AFM probes has been performed using the thermal noise method based on the equipartition of energy [119–121]. Special corrections and procedures for the calibration of the colloidal probes, in particular, to account for geometrical and dimensional issues, have been considered, as described in Ref. [112]. Details on the calibration of the AFM probes are provided in Chapter 1.

The deflection sensitivity S (or inverted optical lever sensitivity, invOLS) of the probes was calculated as the inverse of the slope of the raw deflection ΔV (in Volts) vs. z-piezo displacement (in nm) curve acquired on a stiff substrate [100]. The SNAP method was performed before every experiment for the recalculation of the new sensitivity, assuming a previously accurately calibrated value (considered as a reference) of the spring constant and sensitivity [122]. Indeed, the measurements of S for CPs can be affected by the loading configuration of the probes: the loading is applied on the tip apex and not the cantilever geometrical end, generating torque and influencing the sensitivity value. The implementation of the SNAP method before every experiment allows for the reduction of the variability of measurements and increased their reproducibility.

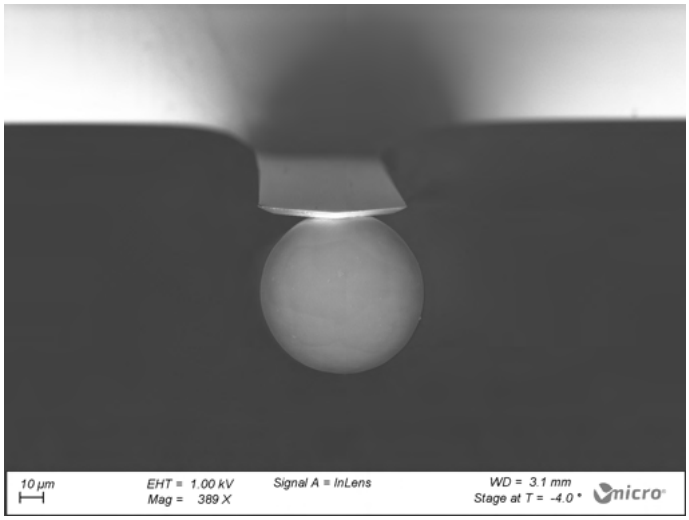

Figure 16. Front view of a custom-made colloidal probe with Scanning Electron Microscopy. Image acquired in collaboration with VMicro SAS (Lille, France).

The cleaning of the probes was performed with Oxygen Plasma (80W, 2min) before functionalization, Helizyme for organic debris in between the experiments, and Piranha solution (3:1 v/v H_2SO_4:H_2O_2 80°C for 30 minutes) for deeper cleaning of organic debris. All those processes are commonly used in the AFM community [123].

2.1.2. Functionalization of AFM probes

Any functionalization of the AFM probes was performed on a clean cantilever (CPs or tipless); for this, we used oxygen plasma (Diener electronic) at 80W for 2 minutes to restore -OH groups [124]. Functionalisation with ECM proteins such as fibronectin and laminin was performed using a first coating of 3-aminopropyl triethoxysilane, (APTES) by mean of 3 minutes vapor deposition in static N_2 from a reservoir [125–127], followed by glutaraldehyde (GAH) for 2h, and the protein deposition for 1h following previously established protocols [128–130]. The cantilevers were stored in PBS and used the same or the next day for experiments.

For cell-cell force spectroscopy, a cell was directly attached to the cantilever using Concanavalin A as adhesive [91]. This procedure is described in detail in Appendix B. Concanavalin-probes could be stored in PBS at 4°C for a couple of days but were rather used directly after functionalisation.

The production of native ECM probes with the functionalisation of the probe with APTES and Genipin is described in detail in Chapter 3.

APTES, Concanavalin A, glutaraldehyde, and Genipin were purchased from Sigma. Genipin was diluted in 1,5% (v/v) in PBS, Concanavalin A at 2mg/ml, and glutaraldehyde at 2,5% in PBS (v/v). Fibronectin and Laminin were both used at 0,5µl/ml.

2.1.3. Force spectroscopy and nanomechanical measurements

For details on the use of AFM as a force sensor and for indentation measurements the reader is addressed to the paper by Holuigue et al. 2022 reported at the end of the Introduction of this thesis [85] .

Both force spectroscopy and nanomechanical AFM experiments are based on the acquisition and analysis of force curves FC as displayed in **Figure 17**. The raw FCs consist of the recording of the raw deflection signal from the photodetector (in Volts units) as a function of the z-piezo displacement (in nm); raw FCs have been rescaled into force in nN vs indentation or tip-sample distance in µm using the measured calibration factors (deflection sensitivity S and spring constant k_{eff}), according to the standard procedure [83].

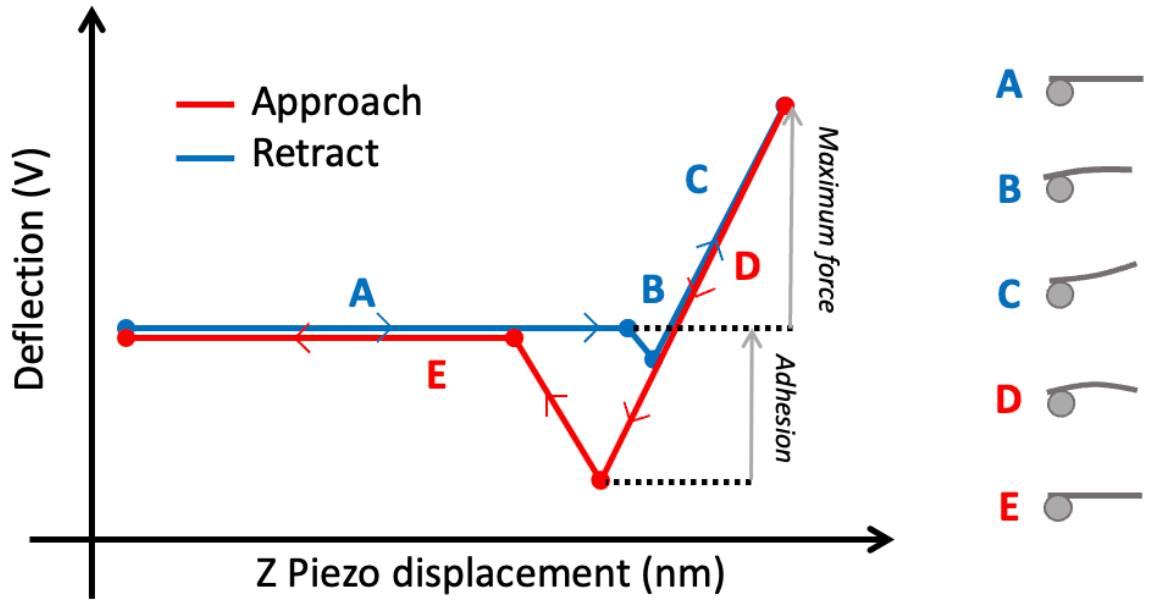

Figure 17. Schematic of a standard force curve approach (blue) and retract (red) during force spectroscopy measurements.

Both approaching and retracting parts of a rescaled FC provides information about the sample. Nanoindentation analysis exploits the contact portion of the approaching part, from the initial contact point to the maximum indentation, at maximum force. The mechanical characterization is typically done by determining the Young's modulus (YM) of elasticity E of the sample, i.e., the proportionality factor between stress σ (in Pa) and strain ε: $E = \frac{\sigma}{\varepsilon}$, through the fit of the Hertz model to the experimental force (F) vs indentation (δ) curve [131–134]:

$$F = \frac{4}{3}\frac{E}{1-\nu^2}R^{\frac{1}{2}}\delta^{\frac{3}{2}} \quad (1)$$

In Eq. 1 R is the tip radius and v is the Poisson's coefficient, which is typically approximated at 0,5 for incompressible materials like cells and is defined as the ratio of transversal to longitudinal relative deformations [131].

Eq. 1, originally developed for parabolic indenters, is accurate for spherical tips as long as the indentation δ is small compared to the radius R, $\delta \ll R$.

Exploiting the retraction portion of the force curve, and focusing on the region of pull-off, we can study adhesive events, as long as the tip detaches from the sample [86,91,113,135] . Details on

adhesion force spectroscopy methodology can be found in the Introduction and on the preprint of the paper by H. Holuigue et al, 2022, reported in Chapter 3.

2.1.4. Data analysis

Processing of the data was carried out using custom routines written in Matlab (Mathworks) if not stated otherwise. Detail procedure for data averaging and error estimation is reported in specific Material and Methods of each chapter.

2.2. Cell cultures

Four commercial cell lines, three from human bladder cancer of different grades (a marker of invasiveness) and one from tumoral rat bladder, were kindly provided by Dr. M. Alfano (San Raffaele Hospital, Milano) and used in this work, as described in **Table 1** and presented in **Figure 18**.

The cell lines were cultured in RPMI medium containing 2 mM L-glutamine supplemented with 10% FBS, 1% penicillin/streptomycin, and 1% amphotericin and grown in a CO_2 incubator at 37 °C with 5% CO_2 (Galaxy S, RS Biotech). All reagents and materials were from Sigma-Aldrich (St. Louis, MO, USA).

Cell line	Species/Organ	Morphology	Tumour
RT4	Human bladder	Epithelial	Papilloma, transitional cell (Grade I)
RT112	Human bladder	Epithelial	Papilloma, transitional cell (Grade II)
T24	Human bladder	Epithelial	Carcinoma, transitional cell (Grade III)
AY27	Rat bladder	Epithelial	Carcinoma, transitional cell

Table 1: Description of the cell lines used in this work, with indication of their species, morphology, and tumour.

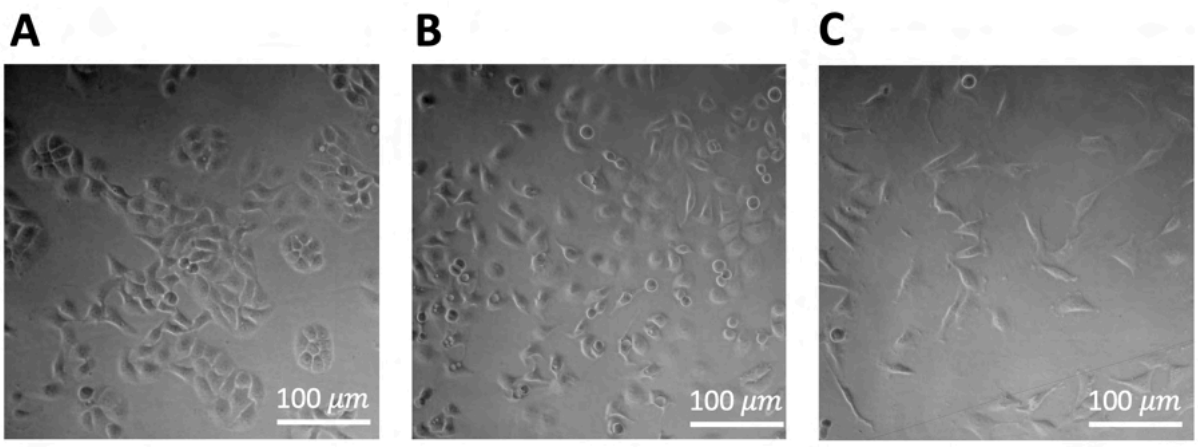

Figure 18. Optical images of (A) RT4, (B) RT112 and (C) T24 cell lines.

For AFM measurements, the cells were plated the day before on glass bottom Petri dishes (Ø 40 mm Willco Wells) coated with poly-L-lysine (0.1% w/v for 30 min at RT) to improve cell attachment and sterilized with UV radiation. Cells were plated in the RPMI medium without phenol red as it can use damage to the AFM liquid tip holder of the Catalyst AFM. Indeed, the use of phenol-red has been correlated with the etching of the resin surrounding the tip holder. Cells were kept overnight in the incubator and used the next day for AFM experiments.

2.3. Decellularized extracellular matrix

Decellularized extracellular matrices from healthy rats were produced at Ospedale San Raffaele, Milano, under the guidance of Dr. Alfano. The decellularization was performed according to the protocol of Genovese et al.[55], validated for bladder [136] (**Figure 19**).

The ECM samples were embedded in optimal cutting temperature (OCT) compound, frozen in dry ice, and kept at -80°C. ECM slices of 10 μm and 50 μm thickness were cut with a cryostat and attached to classical microscope glass slides (for laser microdissection) and super-frost glass slides (for mechanical measurements). The complete protocol for the preparation of ECM for mechanical measurements or laser microdissection is described in Chapter 3.

Laser micro-dissected slides were stored at -4°C and OCT embedded sections were kept at a temperature of -20°C prior to AFM measurements.

All procedures and studies involving mice were approved by the Institutional Animal Care and Use Committee of San Raffaele Scientific Institute and performed according to the prescribed guidelines (IACUC, approval number 942). Adult (9-10 weeks old) female Fischer rats were from Charles River Laboratories, Italy.

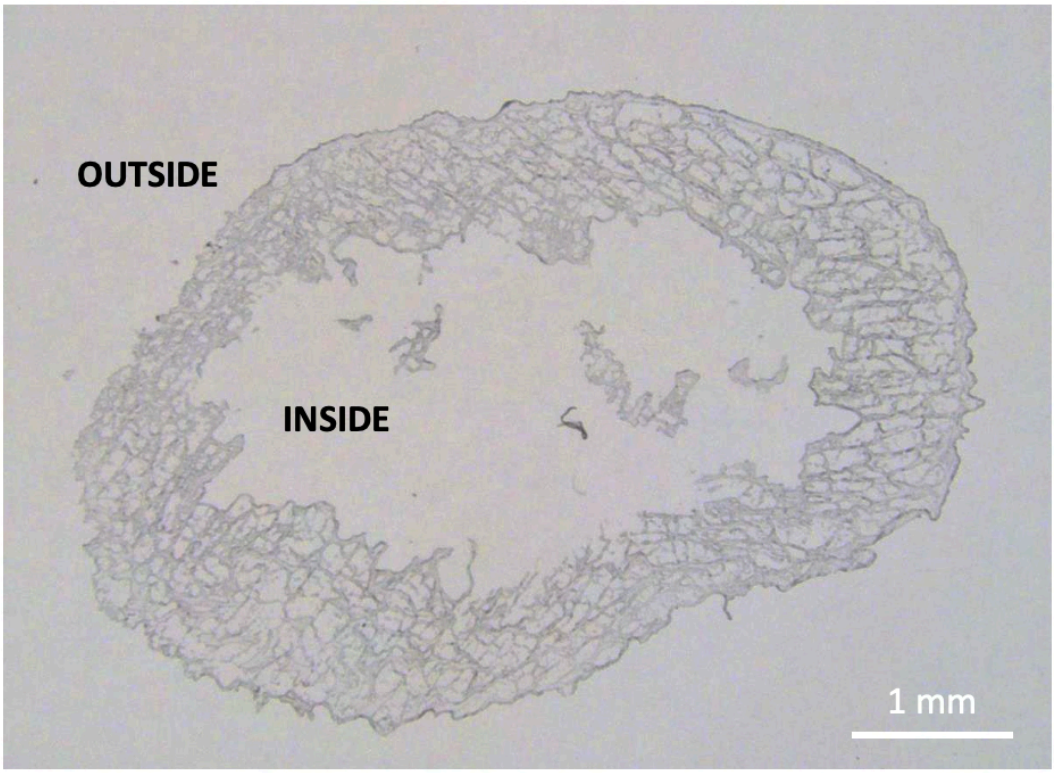

Figure 19. Optical image of a decellularized rat bladder. The inner cavity (where urine is present) and the outer region of the bladder are indicated.

3. Chapter 1

Calibration methods of AFM cantilevers for force spectroscopy measurements

The reliability of AFM data resides in a good calibration of the instrument. The correct calibration of the instrument is consequently crucial for the detection of tiny forces of the order of tenth of piconewton, such as those in the cell-microenvironment: in fact, miscalibration can directly induce misinterpretation of data. In the scope of this thesis, I dedicated part of my time to the comparison and amelioration of the calibration methods in order to collect reliable data while performing adhesion force spectroscopy experiments. While the calibration of commercial cantilevers is widely discussed [82,119,137–140], colloidal probes, even commercial ones, require particular attention [111,112,138,141–147]; in the context of this thesis, both types have been used.

The most common calibration methods exploit the Brownian fluctuations of a cantilever (typically collected through the optical beam detection system (OBD) of the AFM [79,148,149]) to extract a thermal noise spectrum of the cantilever.

One such method is based on the equipartition theorem [78,112,119], which related the mean quadratic oscillation of the cantilever at equilibrium at a given temperature to its spring constant; this is the most widely used method, usually simply called the thermal noise method, and it is usually implemented within the AFM software, although it can also be implemented through external acquisition and processing of the deflection signal. This method requires the implementation of several corrections, accounting for the tilt of the cantilever and the non-ideal (i.e., non-perfectly rectangular) geometry of the cantilever, and also for the influence of an added mass of the tip (or the non-uniform mass distribution along the cantilever axis) that could induce incorrect estimation of the spring constant [112]. This method necessitates the calibration of the sensitivity, a conversion factor for the OBD method that rescales the voltage into deflection. This parameter is not always simple and accurate to evaluate; its calibration requires the registration of FCs on clean and hard substrates, not always possible in the case of biological experiments (Otherwise, a contactless method can be performed if the spring constant is precisely known [150]). CPs calibration of sensitivity could also be critical due to the loading point of the probe, which might induce strong torque effects [112].

Sader's method is also based on the acquisition of a thermal spectrum of the cantilever oscillations but exploits the study of the dynamics of the oscillating body in a viscous fluid (typically, air). This method requires the measurement of a few parameters related to the cantilever oscillation (first normal mode): the cantilever quality factor Q, and the resonance frequency f_0. Initially, the method also required the knowledge of the in-plane geometry and dimension of the cantilever, but in its latest implementation (the Global Calibration Initiative based on an online platform: https://sadermethod.org/ [151]) the request for the geometrical information has been relaxed since it is possible to select the cantilever type and model directly from a database. The internal calibration parameters necessary to implement the Sader method are therefore statistically evaluated based on the contribution of several

scientists worldwide. A great advantage of the Sader approach with respect to the standard thermal noise method based on equipartition and the use of the OBD is that the deflection sensitivity is not required to calibrate the deflection axis. Sader method has been proven to be in good agreement with the standard thermal noise method [152,153]

Finally, as suggested in many articles, interferometry-based systems [154] and especially Laser Doppler Vibrometer (LDV) [140,142,153] are powerful tools to perform calibration of AFM cantilevers and are nowadays considered as gold standard. As the measurement of the deflection is direct, there is no need for calibrating the deflection sensitivity; consequently, the calibration of the spring constant is more reliable.

This work presents the comparison of three calibration methods: standard thermal noise, Sader's, and LDV for tipless cantilevers and colloidal probes, with the objective of developing a reliable calibration procedure for applications in cell-microenvironment research. The experiments have been performed at VMicro (Lille, France) in collaboration with Dr. Benjamin Walter, during a secondment, as part of the project Phys2BioMed.

3.1. Material and Methods

3.1.1. AFM Probes

We used ultrasoft tipless cantilevers (HQ:CSC38/TIPLESS/NO AL, Micromasch), A (short) and B (long), as well as soft tipless cantilevers (TL-CONT, Nanosensors), as presented in **Figure 20**. **Table 2** resumes the geometrical parameters (length L, width w and thickness t) and characteristics of the cantilevers, which are made of single crystalline silicon, n-dopped with antimony, and have a density of $2{,}33\ \mathrm{g/cm^3}$. All cantilevers have a rectangular planar sections and trapezoidal cross-sections, with a small apical triangular end.

Homemade colloidal probes, presented in **Figure 21** and **Figure 22**, were produced as explained in the General Material and Methods section. The characterization of the radius of the sphere was done either by calibrated optical microscopy images, in the case of large spheres, or by reversed AFM imaging on a spiked grating (TGT1, NT/MDT) for spheres with a radius smaller than 10 µm [111,134]. **Table 3** recapitulates the produced CPs and their characteristics: the tip radius R with a density of borosilicate glass spheres as $2{,}23\ \mathrm{g/cm^3}$, the reduced mass $\tilde{m}$, the gyration radius $\tilde{r}$ (as defined in the Eq.15 and 16 respectively), as well as the added mass corrected factor β_{corr}, χ_{corr} and α_{corr}, defined in Eq. 14 and 28.

Type	L (μm)	w (µm)	t (µm)	$k_{nominal}$ (N/m)	f_0 (kHz)
A - Ultrasoft Tipless long ***HQ:CSC38/TIPLESS/NO AL***	350 ± 5	$32,5 \pm 3$	$1,0 \pm 0,5$	0,03	10
B - Ultrasoft Tipless short ***HQ:CSC38/TIPLESS/NO AL***	250 ± 5	$32,5 \pm 3$	$1,0 \pm 0,5$	0,09	20
C - Soft Tipless ***TL-CONT***	450 ± 10	50 ± 7	2 ± 1	0,02 – 0,77	6 – 21

Table 2. Table of the typical geometrical parameters, length L, width w and thickness t of the tipless rectangular cantilevers used in this work to create the CP. Indicated their nominal spring constant $k_{nominal}$ and nominal resonance frequency f_0 according to the manufacturer.

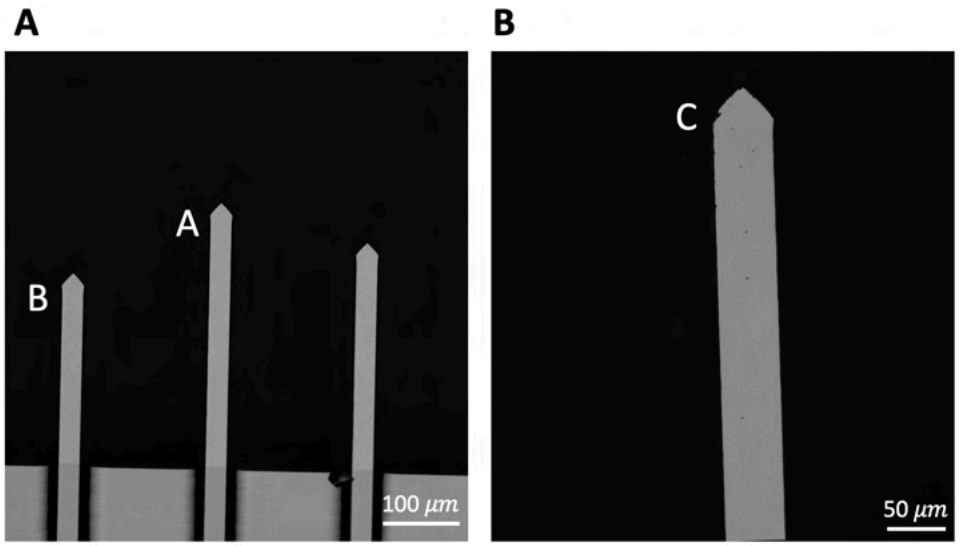

Figure 20. Optical microscopy images of the tipless cantilevers. (A) Micromasch HQ:CSC38/Tipless/No al and (B) Nanosensors TL-CONT as indicated in **Table 2**.

Name	*Tipless type*	R *(µm)*	$\tilde{m}$	$\tilde{r}$	β_{corr}	χ_{corr}	α_{corr}
CP 1	B	8,09 ± 0,12	0,26	0,04	0,9935	1,0399	0,9187
CP 2	B	4,97 ± 0,16	0,06	0,02	0,9812	1,0702	0,8567
CP 3	B	10,02 ± 0,22	0,49	0,05	0,9971	1,0259	0,9475
CP 4	A	8,32 ± 0,44	0,20	0,03	0,9915	1,0459	0,9065
CP 5	A	5,72 ± 0,18	0,06	0,02	0,9812	1,0702	0,8566

Table 3. Table of the measured and calculated characteristic parameters of the homemade CPs. The tipless cantilever used to assemble the CP is indicated (A or B cf. **Table 2**). Also indicated the tip radius R, the reduced mass $\tilde{m}$, the gyration radius $\tilde{r}$, the added mass corrected factor β_{corr}, χ_{corr} and α_{corr}.

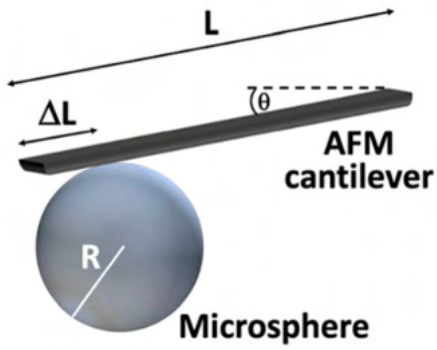

Figure 21. Schematic of a colloidal probe with the geometrical parameters defined : the radius R, the lenght L, the tilt angle θ and the shift of the loading point ΔL of the CP in comparison to the cantilever end.

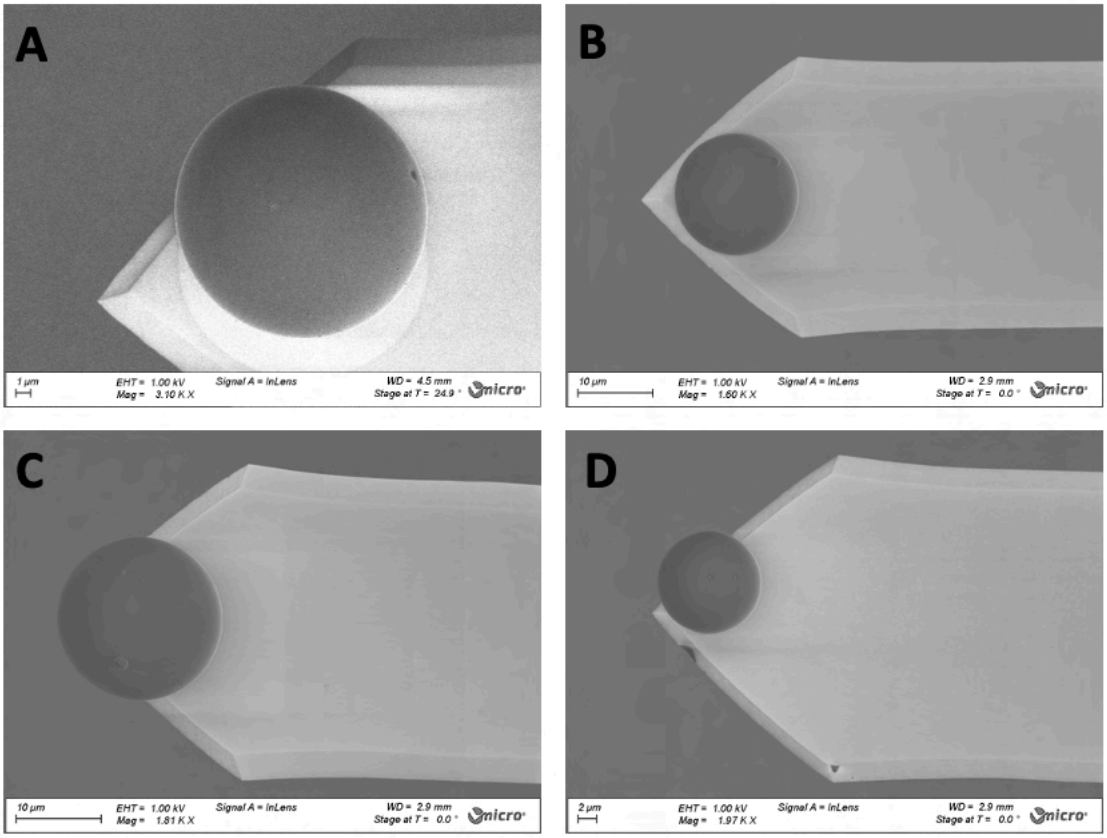

Figure 22. Scanning Electron Microscopy images of the colloidal probes (A) CP 1, (B) CP 3 (C) CP 4 and (D) CP5. Images acquired at VMicro (Lille,France).

3.1.2. Geometrical spring constant of AFM probes

Considering a cantilever with perfectly rectangular planar and transversal sections, with uniform density, width w, thickness t, length l and Young's modulus E, the theoretical formula for the spring constant is [155]:

$$k = \frac{Ewt^3}{4L^3} \tag{2}$$

The accuracy of Eq. 2 to predict the spring constant of a cantilever is severely limited by the fact the nominal geometry is not perfectly rectangular, the dimensions are not uniform, as well as the density and the Young's modulus. Importantly, the thickness (typically around 1 μm or below) is subject to large relative variations, which have a strong impact on the value of k due to the cubic dependence.

3.1.3. Standard thermal noise method

The standard thermal noise method for the calibration of the spring constant is based on the Boltzmann's equipartition theorem [119,120]:

$$\frac{1}{2}k\langle d_{\perp}^{2}\rangle = \frac{1}{2}k_{B}T \tag{3}$$

, where k_B is the Boltzmann constant, T the absolute temperature and $\langle d_{\perp}^{2}\rangle$ is the mean square oscillation amplitude of the free end of the cantilever. Here, we follow Ref. [78] for the implementation of the thermal noise method.

The first flexural mode of oscillation contains 98,5% of the oscillation amplitude. To take it into consideration, we must add a correction factor β counting for the fraction of the total quadratic oscillation amplitude $\langle d_{\perp,1}^{2}\rangle$ in the first normal mode:

$$\langle d_{\perp,1}^{2}\rangle = \beta\langle d_{\perp}^{2}\rangle \tag{4}$$

β = 0,971 for a tipless rectangular cantilever. The spring constant is then calculated as:

$$k = \frac{\beta k_{B}T}{\langle d_{\perp,1}^{2}\rangle} \tag{5}$$

The quadratic oscillation $\langle d_{\perp,1}^{2}\rangle$ can be calculated as the area below the first resonance peak in the power spectral density (PSD) of the cantilever oscillation [156,157]. The following formula then holds:

$$\langle d_{\perp,1}^{2}\rangle = {\chi_{eff}}^{2}S^{2}P_{V} \tag{6}$$

, where P_V is the area below the first peak of the PSD of the raw deflection signal (PSD_V, in units of V^2/Hz), S is the deflection sensitivity, and the additional correction parameter χ_{eff} accounts for the difference between the static and dynamic deflection sensitivity and includes the effect of the cantilever tilt and other geometrical factors ($\chi_{eff} \equiv \chi_0$ = 1,09 for an ideal tipless rectangular cantilevers)[119,156–162]:

$$\chi_{eff} = \chi_{0}\left\{\left(1-\frac{\Delta L}{L}\right)\left(\frac{1-{}^{3}/_{2}\dfrac{\frac{R}{L}}{\left(1-\frac{\Delta L}{L}\right)}tan\theta}{1-2\dfrac{\frac{R}{L}}{\left(1-\frac{\Delta L}{L}\right)}tan\theta}\right)cos\theta\right\}^{-1} \tag{7}$$

It follows that the intrinsic spring constant can be calibrated through the analysis of the PSD_V as:

$$k = \frac{\beta}{{\chi_{eff}}^2} \frac{k_B T}{S^2 P_V} \tag{8}$$

, and more specifically as:

$$k = \frac{\beta}{{\chi_0}^2} \left\{ \left(1 - \frac{\Delta L}{L}\right)^2 \left(\frac{1 - {}^3\!/_2 \dfrac{\dfrac{R}{L}}{\left(1 - \dfrac{\Delta L}{L}\right)} tan\theta}{1 - 2 \dfrac{\dfrac{R}{L}}{\left(1 - \dfrac{\Delta L}{L}\right)} tan\theta} \right)^2 cos^2\theta \right\} \frac{k_B T}{S^2 P_V} \tag{9}$$

When the Simple Harmonic Oscillator (SHO) model is fitted to (**Figure 23A**):

$$PSD(f) = A_0 + \frac{B^2 {f_R}^4}{Q^2} \left[\left(f^2 - {f_R}^4\right) + f^2 {f_R}^4 / Q^2 \right]^{-1} \tag{10}$$

, the area below it (P_V) can be calculated analytically in terms of characteristic parameters of the oscillator (the amplitude B_V, the resonance frequency f_R and the quality factor Q, respectively):

$$P_V = \int_0^\infty PSD_V(f) df = \frac{\pi B_V^2 f_R}{2Q} \tag{11}$$

We end up with:

$$k = \frac{\beta}{{\chi_0}^2} \left\{ \left(1 - \frac{\Delta L}{L}\right)^2 \left(\frac{1 - {}^3\!/_2 \dfrac{\dfrac{R}{L}}{\left(1 - \dfrac{\Delta L}{L}\right)} tan\theta}{1 - 2 \dfrac{\dfrac{R}{L}}{\left(1 - \dfrac{\Delta L}{L}\right)} tan\theta} \right)^2 cos^2\theta \right\} \frac{2Q}{S^2 \pi B_V^2 f_R} k_B T \tag{12}$$

In this work all CPs were produced with relatively long rectangular cantilevers and small spheres attached to the cantilever end, and the laser spot was located at the very end of the cantilever; therefore, the characteristic ratios were all small and, according to Eq. 12 and the intrinsic spring constant could be calculated as:

$$k = 0{,}817\frac{2Q}{S^2\pi B^2 f_R}k_B T \tag{13}$$

, where $\frac{\beta}{\chi_{eff}{}^2} \approx \frac{\beta}{\chi_0{}^2} \equiv \alpha_0 = 0{,}817$.

In the case of CPs, the addition of the mass of the sphere to the end of cantilever will affect the modal shapes of the normal modes, decreasing the resonance frequency while increasing the quality factor [112,141], which changes the pre-factor $\frac{\beta}{\chi_{eff}{}^2} \equiv \alpha$ of Eq. 8. In our case (see Eq. 13) the value changes from $\alpha_0$to a value that can only be calculated numerically (as long as the hypothesis of rectangular geometry holds [112,163] or by finite element (FEA) analysis [159]

Practically, the added mass correction to the spring constant is implemented by multiplying the intrinsic spring constant by the correction factor $\alpha_{corr} = \frac{\alpha}{\alpha_0}$:

$$k_{corr} = \alpha_{corr} k \tag{14}$$

, where k is the measured spring constant and k_{corr} is the corrected one [112].

The value of α_{corr} depends on two parameters, the reduced mass $\tilde{m}$ and the reduced radius $\tilde{r}$ of the sphere [92,120] (**Table 3**):

$$\tilde{m} = \frac{m_s}{m_c} \tag{15}$$

$$\tilde{r} = \sqrt{\frac{7}{5}}\frac{R}{L} \tag{16}$$

, where m_s and R are the mass and radius of the sphere, respectively, and m_c is the mass of the cantilever. In the case of rectangular cantilevers, the values of α_{corr} for different values of $\tilde{m}$ and $\tilde{r}$ are tabulated in Refs [112,163].

Once the intrinsic spring constant of the cantilever has been calibrated, the effective spring constant k_{eff} is calculated and used to rescale the force axis, as shown in the paper Holuigue et al. in the General Material and Methods. In case of negligibly small tip, loaded at the end of the cantilever:

$$k_{eff} = \frac{k}{cos^2\theta} \tag{17}$$

In case that ΔL it is not negligeable, we calculate k_{eff} as:

$$k_{eff} = \left\{\left[1 - \frac{3R/L}{(2(1-\Delta L/L)}tan\theta\right]cos^2\theta\right\}^{-1}\left(\frac{L}{L-\Delta L}\right)^3 k \tag{18}$$

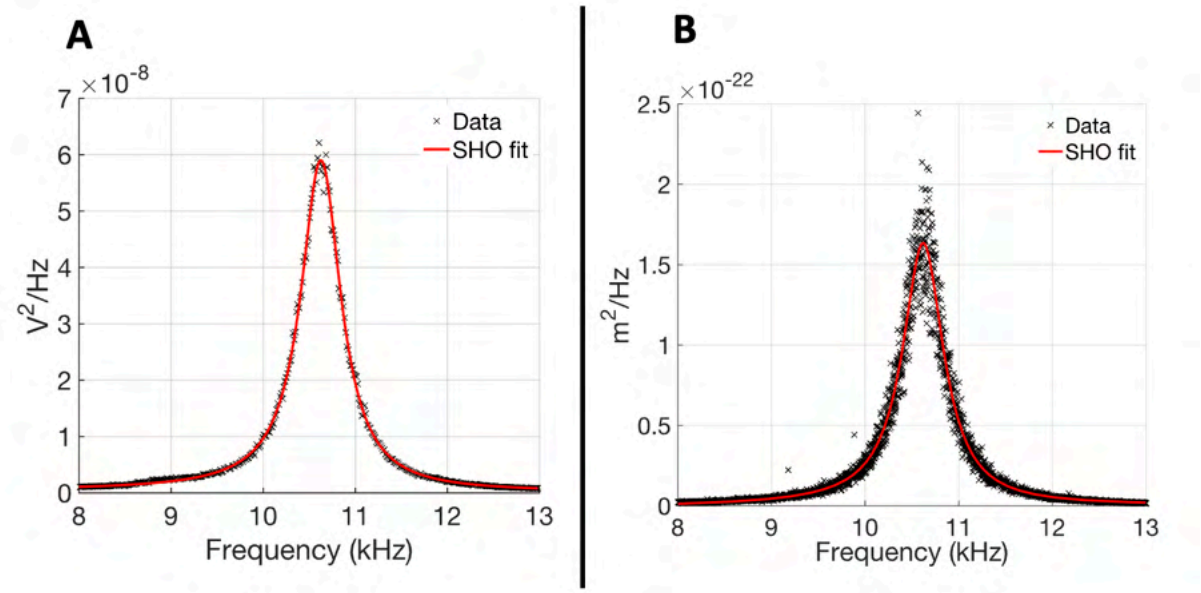

Figure 23. Representative of a measured PSD P_V at the first normal mode for a probe A - Ultrasoft Tipless long (HQ:CSC38/TIPLESS/NO AL) taken with the (A) Standard thermal noise method and the (B) LDV.

To be noted that in the literature the denomination of the factors of corrections such as β, α and χ are not yet standardized within the AFM community; in this work we followed the of the Ref. [78].

3.1.4. Sader method

Sader's method is derived from the modelling of the cantilever dynamics in a viscous fluid upon thermal excitation [78,137,151,164,165] where the spring constant is stated as followed:

$$k = \beta\rho b^2 L\Lambda(Re)\omega_R{}^2 Q \tag{19}$$

$$Re = \frac{\rho\omega_R b^2}{4\mu} \tag{20}$$

, where ρ and μ are density and shear viscosity of fluid surrounding the cantilever, respectively; L and b are the cantilever length and width, respectively; ω_R is the angular resonance frequency and $\Lambda(Re)$ the hydrodynamic function depending on the Reynolds number[164,165]. β relates to the fraction of the quadratic oscillation amplitude of the first normal mode [119,158]. Also, Sader's method requires the knowledge of β factor; nevertheless, it does not require the calibration of the deflection sensitivity, at odd with the standard thermal

noise method. Moreover, Sader's method does not require the determination of the cantilever thickness, since only the planar dimensions of the cantilever are required in the original implementation.

In this work the AFM cantilevers were calibrated using Sader's global calibration initiative online toolbox [151], which represents a further simplification of Sader' approach, only requiring the measurement of the resonance frequency f_0 and the quality factor Q for cantilevers that are present already in the database, which is contributed by a community of AFM users worldwide. The database is populated with cantilever specific correction factors that can be calculated once the spring constant of the cantilever is calibrated by another independent accurate method (such as LDV). The relation between the parameters of a reference cantilever (k_{ref} , Q_{ref} and f_{ref}) and those of a non-calibrated one of same planar geometry, dimensions and properties is:

$$k = k_{ref} \frac{Q}{Q_{ref}} \left(\frac{f_R}{f_{R,ref}} \right)^{2-\alpha} \tag{21}$$

, where $\alpha = 0{,}7$. This equation can be written as:

$$k = AQ{f_R}^{1,3} \tag{22}$$

The factor A, specific to a type of cantilever, implicitly accounts for the hydrodynamic function [151,166], and can be calculated statistically as the average of the N user-contributed values:

$$A = \frac{1}{N} \sum_{i=1}^{N} A_i = \frac{1}{N} \sum_{I=1}^{n} \frac{k_{ref}, i}{Q_{ref,i} * f_{R,ref,i}^{1,3}} \tag{23}$$

Following the online calibration initiative, the calibration of the intrinsic spring constant of the cantilever simply requires fitting the SHO model to the PSD_V and determining f_0 and Q. To this purpose, we asked colleagues in Sader's group to add TL-CONT, Nanosensors, tipless cantilevers to the database; the other one (HQ:CSC38/TIPLESS/NO AL, Micromasch) were already inserted.

3.1.5. Laser Doppler Vibrometer

The measurements of interferometry were performed at VMicro, Lille (France) using a Polytech MSA 500 with a velocity controller VD_06 1mm/s/v or VD_06 2mm/s/v and a displacement controller DD_300. The measurements were performed by aligning a first laser aligned on the back of the cantilever and the second laser (reference) aligned at the cantilever

base, as shown in **Figure 24**. The probe was placed on an AFM multimode (Bruker) tip holder, mounted on a 3D printed stage to compensate for the 11° tilt of the probe.

LDV is a non-contact interferometric technique that uses the doppler effect to measure the displacement of a moving surface [140,167,168.] The Doppler effect is the shift of the frequency of the light (or acoustic wave) emitted at the source when it reaches an observer, caused by the relative motion of the source and observer. By moving towards the source, a higher frequency is detected, while a lower frequency is detected in the opposite case [169].

For the calibration of AFM cantilevers, in the LDV apparatus the laser light reflected at the end of the cantilever that oscillates due to Brownian motion, experiences a Doppler shift compared to the reference beam placed at the base of the cantilever, as shown in **Figure 24**. The Doppler shift $\Delta f_D(t)$ is equal to [154]:

$$\Delta f_D(t) = \frac{2v(t)}{\lambda} \tag{24}$$

, with $v(t)$ the instantaneous speed and λ the wavelength of the initial emission. This method primarily measures the speed v, which is then transformed into displacement (oscillation amplitude) of the cantilever by integration over time. The first value of the displacement signal $d_{\perp,0}$ is assumed at 0, then the followed displacement $d_{\perp,i}$ is defined as:

$$d_{\perp,i} = d_{\perp,i-1} + v\Delta t \tag{25}$$

, with Δt the time interval, assuming that the current velocity is constant. LDV allows the direct measurement of the displacement $\langle d_\perp^2 \rangle$, which eliminates one of the greatest sources of the OBD error in the standard thermal noise methods i.e., the calibration of the deflection sensitivity S, which makes the LDV a contact-less calibration method [140,142]. It then allows for the elimination of the factor of correction χ, counting for the correction from the statistic to the dynamic S. Accuracy of interferometric detection makes LDV and other interferometric techniques [163,170] the gold standard for the calibration of the AFM spring constant [140,171] :

Using LDV, the intrinsic spring constant k is therefore calculated using the equipartition formula (Eq. 11):

$$k = \frac{\beta\, k_B T}{\langle d_{\perp,1}^2 \rangle} \tag{26}$$

, given that the amplitude of oscillation of the cantilever $\langle d_\perp^2 \rangle$ is measured directly and the amplitude of the first normal mode and $\langle d_{\perp,1}^2 \rangle$ can be extracted from the PSD, as described for the other methods, with the difference that the PSD in physical units (m^2/Hz) is used, instead of the PSD_V of the raw deflection signal (V^2/Hz) (**Figure 4B**).

The spring constant using the LDV system is then:

$$k = \beta \frac{2Q}{\pi B^2 f_R} k_B T \tag{27}$$

, where B here is the PSD amplitude as in Eq. 10.

As for the OBD-based method, while calibrating colloidal probes there can be a modification of the modal shapes due to the added mass effect[112,141], inducing a change in the parameter α, which in the case of LDV reduces to a change in the β factor only, since χ is not present.

In this case, we introduce the correction factor $\beta_{corr} = \frac{\beta}{\beta_0}$ and in the same way as Eq. 14, we calculate the corrected spring constant k_{corr} as:

$$k_{corr} = \beta_{corr} k \tag{28}$$

To be noted that the modal factor β, accounting for the fraction of the total quadratic oscillation amplitude in the first normal mode, is present also in the case of the LDV method. Noticeably, the factor β is required for all three techniques considered so far, and this fact poses a serious issue for the accurate calibration of the cantilever spring constant since this factor can only be calculated by FEA for non-ideally rectangular cantilevers.

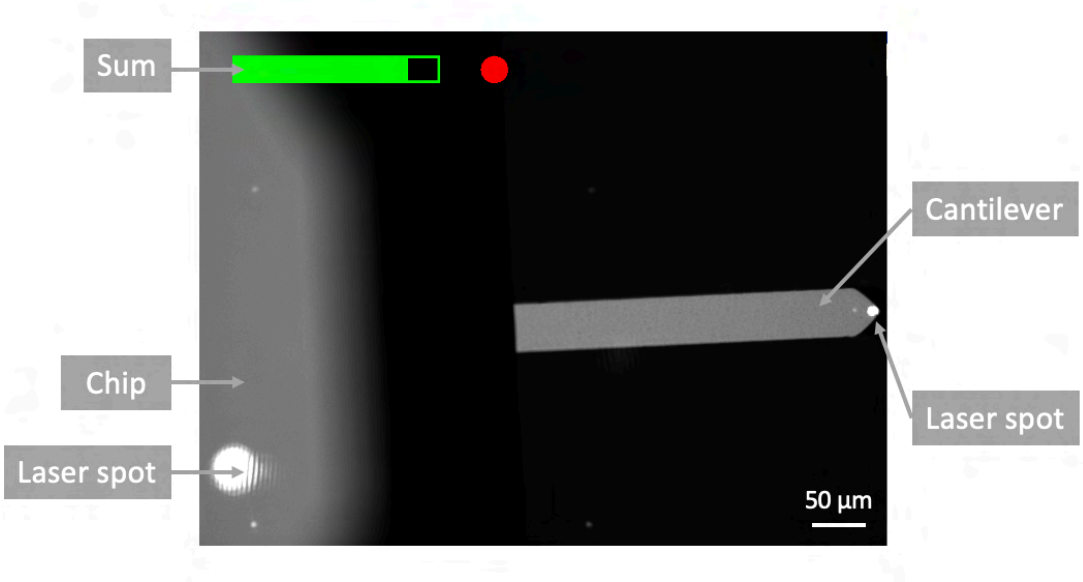

Figure 24. Image displayed by the Laser Doppler Vibrometer instrument. The cantilever and the chip are visible, with the spot of both lasers.

3.1.6. Data analysis

Processing of calibration data from LDV and AFM was carried out using custom Matlab scripts (Mathworks). The SHO model (Eq. 10) was fitted to the peak of the first mode of oscillation (**Figure 23**) and the parameters Q, f_0 and B_V (or B) were extracted, to compute the area below the PSD_V (or PSD). For the Sader's method, the fitted Q and f_0 values were used in the global calibration initiative online toolbox.

In the following, we refer to the values of the intrinsic spring constant calculated using the different methods as $\mathbf{k_{nominal}}$, for the spring constant communicated by the manufacturer, $\mathbf{k_{Geom}}$ the one recalculated geometrically (Eq.2), $\mathbf{k_{Th}}$ the one calculated by the standard

thermal noise (Eq. 14), $\mathbf{k_{LDV}}$ via the laser Doppler vibrometer (Eq. 28) and $\mathbf{k_{Sader}}$ using the Sader global initiative methods (Eq. 22). For the colloidal probes $\mathbf{k_{Th\ NC}}$ and $\mathbf{k_{LDV\ NC}}$ indicates the intrinsic spring constants non corrected via standard thermal noise method (Eq. 13) and LDV (Eq. 27) respectively.

The error associated with the calculation of k_{Geom} was evaluated by propagating the geometrical uncertainties through Eq. 2:

$$\frac{\delta k_{Geom}}{k_{Geom}} = \sqrt{\left(\frac{\delta w}{w}\right)^2 + 9\left(\frac{\delta L}{L}\right)^2 + 9\left(\frac{\delta t}{t}\right)^2} \quad (29)$$

Regarding k_{Th}, the error was calculated by propagating the uncertainty of the deflection sensitivity S (5% for tipless cantilever and 10% for colloidal probes), based on equation 13:

$$\frac{\delta k_{Th}}{k_{Th}} = 2\left(\frac{\delta S}{S}\right) \quad (30)$$

The error for k_{Sader} was directly provided by the online tool and is based on the distribution of A factors of the users, equivalent to the standard deviation of the mean regarding Eq. 23 [151].

Interferometry-based calibration for k_{LDV} are supposed to be the most reliable calibration method [140,171]. The error on the spring constant was evaluated as 2% compared to a SI traceable electrostatic force balance method [172]; here, we assume a conservative error of 5%.

3.2. Results

In the results below, we compare the outcomes of those calibration techniques for both tipless and colloidal probes.

3.2.1. Comparison of calibration methods for tipless cantilevers

In **Table 4** and **Figure 25** are presented the intrinsic spring constants measured using the different calibration methods for the tipless cantilevers. As expected, the nominal and theoretical values of the spring constant are similar, considering that usually manufacturers indicate a wide range of values. The error on the geometrical calculation (Eq. 29) is dominated by the cubic dependence of the relative error on the thickness (0,5 µm uncertainty compared to a thickness of 1µm); this explains the large error bars in **Figure 25**.

Interestingly, while comparing k_{Th} and k_{LDV} (**Figure 26**), we observed a good agreement, expressed by an R^2 of 0,9918. The difference between the calibration with AFM and LDV can be explained by the method of acquisition: LDV does not require the evaluation of the sensitivity of the OBD system. Concerning the comparison of k_{Th} and k_{Sader} spring constants,

they do also show an R^2 close to 1 (0,9962). In general, the calibration of the tipless cantilevers with all methods provides similar values consistently.

In comparison to TP1 and TP2, TP3 spring constant values are really dispersed and do not seem to converge to an agreement. The nominal and geometrical values have large errors, the manufacturer indicates indeed a nominal value between 0,02 and 0,77. This tipless cantilever was then not chosen to produce colloidal probes in this work, but rather the ultrasoft ones (TP1 and TP2 short and long).

Name / Spring constant (N/m)	$k_{Nominal}$	k_{Geom}	k_{Th}	k_{LDV}	k_{Sader}
TP 1 short	0,09	0,088 ±0,132	0,070 ± 0,007	0,075 ±0,004	0,078 ± 0,005
TP 2 short	0,09	0,088 ±0,132	0,080 ± 0,008	0,080 ±0,004	0,085 ± 0,005
TP 1 long	0,03	0,032 ±0,048	0,029 ± 0,003	0,027 ±0,001	0,031 ± 0,001
TP 2 long	0,03	0,032 ±0,048	0,028 ± 0,003	0,029 ±0,001	0,032 ± 0,002
TP 3	0,02 – 0,77	0,185 ±0,279	0,097 ± 0,010	0,455 ±0,023	0,326 ± 0,018

Table 4. Comparison of intrinsic spring constants in N/m measured using the three calibration methods: the standard thermal noise method (k_{Th}), the LDV method (k_{LDV}) and the Sader's method (k_{Sader}). The nominal and the geometrical values ($k_{Nominal}$ and k_{Geom}) for the tipless cantilevers are also indicated.

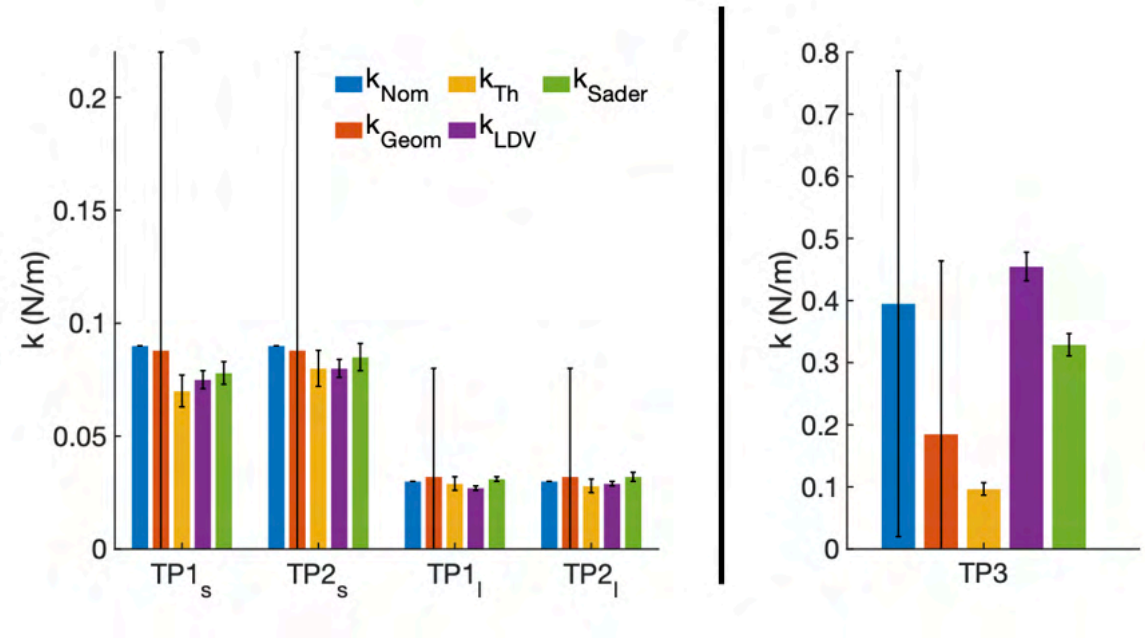

Figure 25. Bar plots representing the intrinsic spring constants in N/m measured with all calibration methods for the tipless cantilevers. Error calculations were evaluated as explained in Data analysis section of the Material and Methods of this chapter.

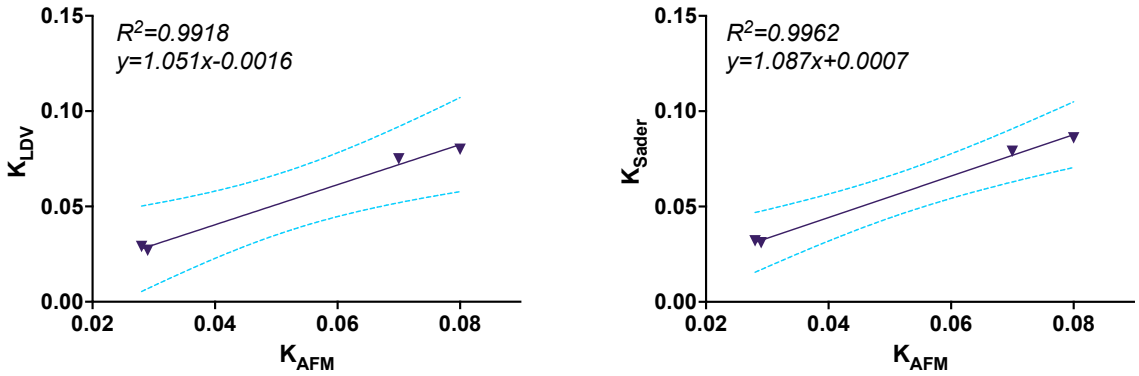

Figure 26. Comparison between (left) k_{th} and (right) both k_{LDV} and k_{Sader}.The light blue dotted line representing the 95% confidence intervals. TP3 is not presented in those graphs.

3.2.2. Comparison of custom colloidal probes

The homemade CPs were calibrated using the same methods as the tipless cantilevers described above. The added mass corrections are reported in **Table 2** and their intrinsic spring constant in **Table 5**.

In general, we measured higher values of the spring constant when using the LDV system k_{LDV} compared to the k_{Th} (**Figure 27**) for CPs. Even though the slope in **Figure 28** exceeds 1 (witnessing a systematic overestimation by one method compared to the other), the linear regression coefficient is close to 1 (R^2=0,8447). The values of k_{Th} and k_{Sader} were not well correlated (R^2 = 0,6505), as expected since the online tools do not account for added mass effects but assumes that the effects of the mass of the tip and any mass distribution non uniformity are negligible.

Name / Spring constant (N/m)	$k_{nominal}$	k_{Geom}	k_{Th} *NC*	k_{Th}	k_{LDV} *NC*	k_{LDV}	k_{Sader}
CP 1	0,09	0,088 ±0,132	0,082 ±0,016	0,092 ±0,0018	0,094 ±0,005	0,096 ±0,005	0,129 ± 0,008
CP 2	0,09	0,088 ±0,132	0,022 ±0,004	0,023 ±0,005	0,056 ±0,003	0,057 ±0,003	0,091 ± 0,006
CP 3	0,09	0,088 ±0,132	0,081 ±0,016	0,095 ±0,019	0,125 ±0,006	0,128 ±0,006	0,119 ± 0,007
CP 4	0,03	0,032 ±0,048	0,045 ±0,009	0,050 ±0,010	0,050 ±0,002	0,051 ±0,002	0,056 ± 0,003
CP 5	0,03	0,032 ±0,048	0,012 ±0,002	0,013 ±0,003	0,012 ±0,001	0,013 ±0,001	0,016 ± 0,001

Table 5. Comparison of intrinsic spring constant in N/m with the three calibration methods (the AFM standard thermal noise k_{Th}, the laser doppler vibrometer k_{LDV} and the Sader method k_{Sader}) as well as the nominal one from the manufacturer $k_{nominal}$ and recalculated one from geometrical parameters k_{Geom} for colloidal probes. NC indicates the non-corrected spring constant.

Both nominal and theoretical spring constants values are not taking into consideration the exact geometrical configuration of the cantilever neither the added mass, thus, show lower values. CP2 exhibits an unexpected and non-repeated softer spring constant for the k_{Th}, this value was overall considered as an outlier.

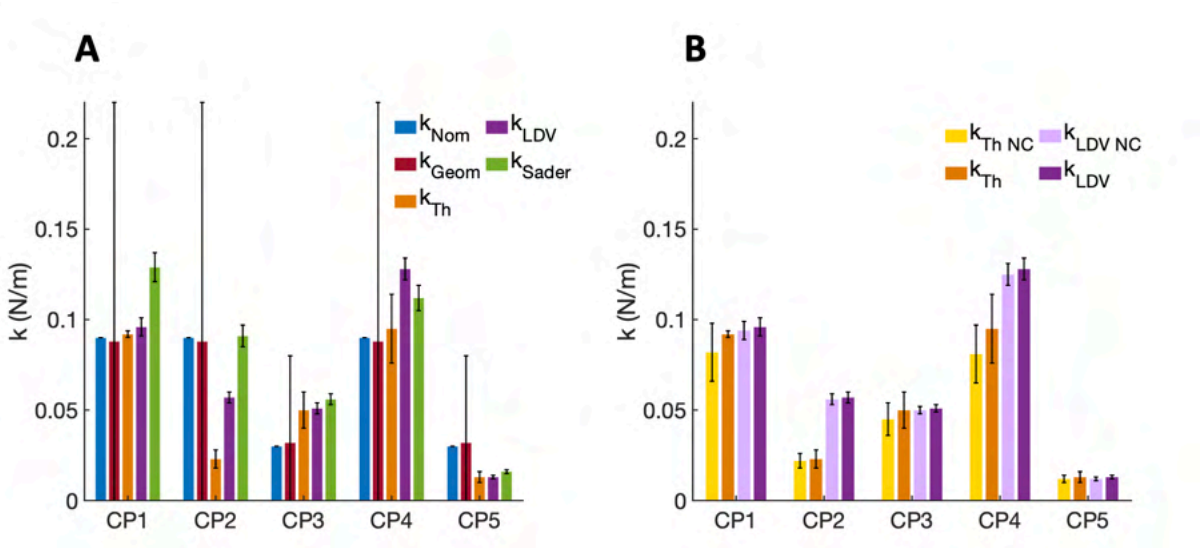

Figure 27. (A) Bar plot of spring constant with all calibration methods for the colloidal probes . (B) Calibration of the colloidal probe before and after correction, both for k_{LDV} and k_{Th} measurements. Error calculations were evaluated as explained in Data analysis section of the Material and Methods of this chapter.

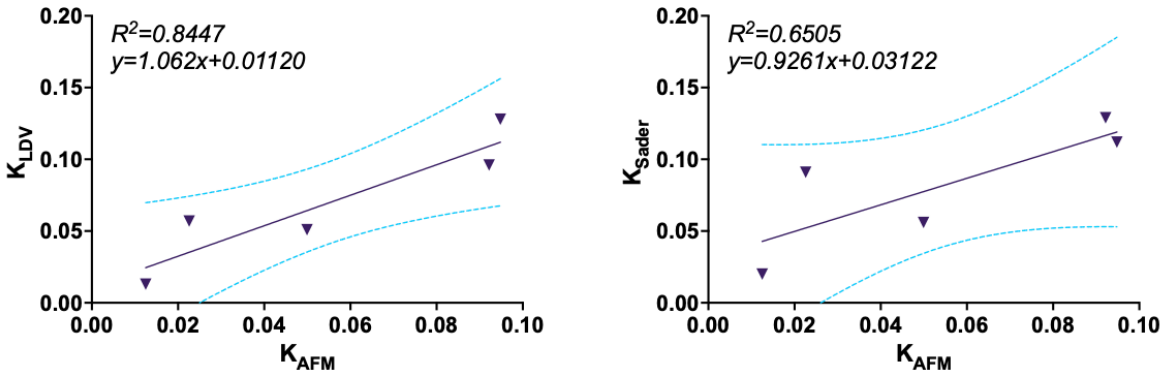

Figure 28. Comparison between (left) AFM and both LDV and (right) Sader's methods of calibration. The light blue dotted line representing the 95% confidence intervals.

When the correction for the added mass is not applied, cantilever spring constants k_{LDV} and k_{Th} reveal a little overestimate, as shown in **Figure 28B**. This was also observed in the work by Chighizola et al.[112] that shows that even the for a reduced mass as small as $\tilde{m}$ = 9.8x10^{-4}, a shift of the resonance frequency compared to the tipless cantilever can be observed [173].

3.3. Discussion

LDV, despite being noninvasive, faster, and supposedly more precise [140], is not accessible to all labs, as it requires the purchase of expensive equipment. As presented in the **Figure 23B**, the PSD acquired with the LDV system show higher signal to noise ratio compared to the one taken by the OBD system, which could impact on the accuracy of the estimation of the area under the first resonant peak and therefore of $\langle d_{\perp,1}^2 \rangle$.

One of the parameters whose estimation is most prone to errors is the deflection sensitivity S. The deflection sensitivity plays a critical role both in the rescaling of both force and tip-sample distance (or indentation) axes, and in the calibration of the spring constant by the standard thermal method.

For the CPs, the larger they are, the stronger the adhesion between the probe and a hard surface (especially in air). Since friction is proportional to load, friction-induced torque effects can be strong [160,174] and can modify the bending profile of the cantilever and consequently the measured deflection during the acquisition of a force curve. An approached proposed by Chighizola et al.[112] consists in calibrating the spring constant on the tipless cantilever prior to the attachment of the sphere; the presence of the attached mass indeed does not change the intrinsic stiffness of the cantilever, as long as we can exclude rigidification of the portion of the cantilever where the sphere is attached (due to the glue, for example). As explained in previous published papers [112,141], the addition of the mass of the sphere to the cantilever modifies the cantilever dynamics, inducing an apparent stiffening of the measured spring constant. As the Sader's calibration does not include these corrections (through the β factor), the values are expected to be higher than the ones measured with AFM and LDV as we

observed in this work (**Figure 28**). This observation is confirmed by Sader et al. [164], where it is mentioned that a sphere with a diameter comparable to the cantilever's width could induce an underestimation of the spring constant.

To be noted that in this work is presented calibration with regular rectangular cantilevers. The theory presented in the previous sections strictly applies only to the ideal rectangular geometry. The triangular geometry already needs an FEA approach. Nowadays, a variety of exotically and far from regularly shaped cantilevers and probes are produced for different applications, most of which, in addition to a non-standard geometry, possess a non-uniform mass distribution along the cantilever axis. For a precise evaluation of the correction factors β and χ, FEA must be used [159,175,176]; this would allow a reliable estimation of the spring constant for cantilevers of arbitrary geometry and tip dimensions. To be noted that FEA in principle considers all possible effects due to mass, geometry, shift of the loading point, etc. provided it is well guided by the accurate knowledge of the three-dimensional shape of the probe; the latter information can be acquired in house with some limitations in accuracy or could be better provided by the manufacturer.

The main objective of this chapter was to evaluate the relative accuracy of the different calibration procedures for both tipless and colloidal AFM probes, establishing best practices and standard procedures for our future experiments. While for the calibration of tipless cantilevers we reached a good agreement among the different methods (standard thermal noise, LDV and Sader's), the calibration of the CPs seemed to be more problematic. More systematic research, with more measurements should be performed to assess the best calibration method.

The protocol followed in the rest of the work presented in this thesis for the calibration of both tipless (Chapter 3) and colloidal probes (Chapter 2), in air, is reported below.

3.3.1. Calibration protocol for tipless cantilevers

1. The deflection sensitivity S is measured from raw FCs (raw deflection signal in Volts vs z-piezo displacement in nm) taken on a hard surface as the inverse of the slope in the contact region. It is advised to take the FCs on a TGT1 (NT/MDT) spiked grating to limit the contact area with the substrate and precisely define the loading point that is not well defined with a tipless cantilever and that could lead to potential inaccuracy of the sensitivity.
2. Data processing is performed using custom-made routines in Matlab (Mathworks) or directly within the Labview software, allowing extraction of PSD parameters as in Eq. 11 and calculation of intrinsic spring constant according to Eq. 13 with
3. The effective spring constant k_{eff} used to compute the force axis is calculated according to Eq. 17 with $\alpha_0 = 0{,}817$.

3.3.2. Calibration protocol for colloidal probes

When the pre-calibration of the tipless cantilever, prior to the attachment of the sphere, is not possible (i.e., commercial CPs, lack of time), we proceed for the calibration of the CPs as follows:

1. The deflection sensitivity S is measured from raw FCs (raw deflection signal in Volts vs z-piezo displacement in nm) taken on a hard surface as the inverse of the slope in the contact region. When too much adhesion is observed, the FC is taken on a

TGT1 (NT/MDT) spiked grating, reducing the adhesion between the CP and the glass. To ensure that the sphere rests on one spike rather than several (that could potential induced large torque effects of the CPs), this procedure can be carried out on a reversed triangular tapping mode cantilever (i.e., fixed on a glass slide) for relatively tiny spheres.

2. The radius of the CP (necessary to implement the corrections in Eq. 12 and 16) is characterized as described in Indrieri et al. [111], by reverse imaging on the same TGT1 spiked grating. For probes with radius larger than 10µm, calibrated optical images can be used instead.
3. Data processing is performed using custom made routines in Matlab (Mathworks) or directly within the Labview software, allowing extraction of PSD parameters as in Eq. 11 and calculation of intrinsic spring constant according to Eq. 13.
4. The α_{corr} correction factor (Eq. 14) for the added mass effect is calculated and applied to the measured intrinsic spring constant. An online tool based of Ref.[163] allows the calculation of the correction factors within the limit of ΔL negligeable: https://perso.ens-lyon.fr/ludovic.bellon/wp/tools/colloidal-probe-calibrator/
5. The effective spring constant $\mathrm{k_{eff}}$ used to compute the force axis is calculated according to Eq. 17 or 18.

4. Chapter 2

Study of cell-microenvironment interaction during bladder cancer invasion

During the progression of cancer, the epithelial to mesenchymal transition (EMT) and its reverse, mesenchymal to epithelial one (MET), is characteristic of the metastatic cells moving toward a secondary site and settling (**Figure 8**). During that process, there is a switch between epithelial markers and a gain in mesenchymal ones [39]. The matrix plays an important role in that transition as the cells require a niche to support their growth (the pre-metastatic niche) [41,54] and displacement (the metastatic niche) [40]. It is then clear that it is in the adhesion between cells and the microenvironment, more specifically the ECM with its proteins, that resides the clues to the understanding of cancer progression[34].

Since cell-microenvironment interaction forces are of the order of 1-100 pN, AFM arises as the most suitable instrument to characterize them using the Force Spectroscopy mode (See the section Atomic Force Microscopy for the study of biological interactions for details). In this method, a functionalized probe with either proteins [21,93] or ECM motifs [90,130] is approached to a cell and allowed to interact for a defined contact time. Once done, the cell and the cantilever are separated and several parameters are extracted from the retracting curves: F_a, the maximum adhesion force; W, the work done during that detachment; $N_{j,t}$, the number of events (respectively jumps and tethers), with their mean forces per event $F_{j,t}$. All these parameters give us an insight into the cell-microenvironment interactions and affinities [97,113,135].

Previous research established the link between the invasiveness properties of the cancer cells and their adhesion to ECM proteins, using for example adhesion assay: a typical test to assess in which cells are plated onto a functionalized substrate, after a washing step, colorimetric detection of bound cells is performed [177]. Nonmalignant bladder cells HCV29 have been shown to have a higher affinity to laminin, fibronectin, and collagen IV than their cancerous counterpart T24 [178]. The variations in integrin expression in healthy and cancerous cells may account for those adhesion discrepancies. Even though the $\alpha 2$, $\alpha 3$ and $\alpha 5$ integrin subunits were found to be similar in HCV29, T24, and HU456 cells [179], it is in general well known that the alteration of the integrins can be linked to cancer invasion: as an example, $\alpha 5\beta 3$ was found to facilitate tumor invasion and metastasis, also with T24 bladder cells in 3D reconstructed ECMs [180].

In the following chapter, we aimed at assessing the role of specific ECM proteins, in cancer invasion by means of reversed single-cell force spectroscopy. In this approach, rather than attaching the cell to the cantilever and approaching it to functionalized substrate, an ECM's protein functionalized CP is approached to adherent cells. The advantages of this strategy are, among others, the study of multiple cells and a more precise evaluation of the contact region between the cell and substrate for an accurate assessment of the observed and applied forces.

We conducted adhesion force spectroscopy experiments on a human model of bladder carcinoma in contact with laminin and fibronectin functionalized colloidal probes. The purpose

was to gain a better knowledge of how cells alter their integrin-related adhesion to the ECM matrix as their invasiveness increases to promote the epithelial-to-mesenchymal transition. Laminin and fibronectin, two of the most common matrix proteins, and three cell lines with invasiveness grades ranging from grade 1 to 3 were used: RT4, RT112, and T24. These cells lines have been widely studied in terms of mechanics [42,43,181] and our nanoindentation data are presented in the published article on Sensor by H. Holuigue et al. [85], which confirmed the softening of grade 3 cells, T24, compared to RT4, their less invasive counterpart as expected from cells undergoing the malignancy process [42,73].

4.1. Material and Methods

4.1.1. Fabrication, calibration, and functionalization of colloidal probes

Custom-made Colloidal Probes (CP) have been fabricated, and calibrated according to previously established protocols [111,112] and discussed respectively in General Material and Methods and in Chapter 1 of this thesis.

We used ultrasoft tipless cantilevers from Micromasch USA HQ:CSC38/TIPLESS/NO AL, cantilever B (long) as presented in **Figure 20A** for their small spring constant (around 0,03N/m) that allows the recording of tiny unbinding events below 10 pN. The radius of the sphere was kept around 5µm.

The deflection sensitivity was calibrated before every measurement using the SNAP method[122], using as a reference the spring constant of the cantilever characterized before the functionalization as described in Chapter 1; in this way, no contact with a hard substrate (in that case the glass bottom of the petri dish) was established, avoiding possible degradation of the functionalization of the CP.

The functionalization of clean CPs with ECM proteins was performed using a first coating of (APTES) followed by glutaraldehyde (GAH) and then protein incubation in solution for 1h [128,129], as explained in the section Functionalization of AFM probes of General Material and Methods.

4.1.2. Cell culture

The experiments were carried out with the three cells line RT4, RT112, and T24 representative of the human cell model of bladder carcinoma, from grade 1 to grade 3 of invasiveness. They were kindly provided by Dr. M. Alfano (San Raffaele Hospital, Milano) and used in this work, as described in **Table 1** and culture as presented in General Material and Methods

For AFM experiments, cells were seeded one day before the measurements and the medium was exchanged 20 minutes before with phenol red-free medium to avoid damage to the AFM tip holder.

4.1.3. Force Spectroscopy experiments

Experiments were performed at CIMAINA, Department of Physics, Università degli studi di Milano, with a Bioscope Catalyst (Bruker) as presented in **Figure 14**. During the

experiments, cells were kept at 37°C degree with a perfusion stage incubator (Bruker) and a temperature controller (Lakeshore 331, Ohio, USA), as described in General Material and Methods.

We performed force spectroscopy on the three cell lines with functionalized probes with laminin and fibronectin and with bare borosilicate glass as a control experiment at 4 contact times: 0, 20, 60 and 120s, as shown in **Figure 29**. Each FC containing 8192 points was acquired with the z close loop on, with a maximum load of 1nN, with a ramp size of 15µm and a ramp frequency of 1Hz. During the contact time the AFM controller maintained a constant z-piezo position. At least 4 cells were tested for each contact time, for each condition (different cell lines, different proteins etc.) and at least 3 FCs were acquired per cell. To be noticed that these experiments are time-consuming since the contact time can be of several minutes.

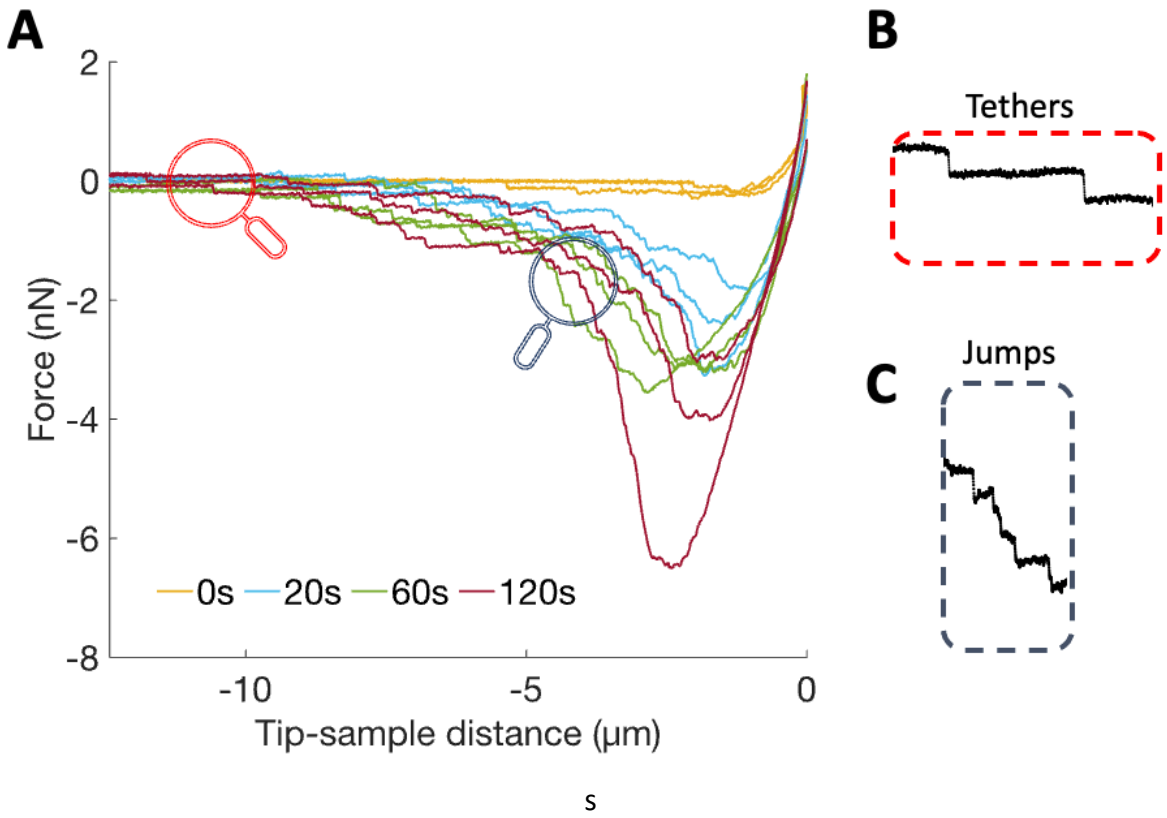

s

Figure 29. (A) FCs representing at different contact time, the interaction between the RT4 cells and a laminin functionalized probe, with insights on of representative (B) tethers and (C) jumps.

4.1.4. Data analysis

Data analysis was carried out using custom Matlab (Mathworks) routines. Analysis of the rescaled retraction portion of the FCs was performed as described in recent works [113,135]. The numerical derivative of the FC is directly used to detect events out of a manually defined noise threshold, as presented in **Figure 30**. Adhesion events give rise to discontinuities in the derivative, which allows to identify them. Those adhesion events can be of two forms, jumps and tethers, as shown in **Figure 29B** and **C**; while both are associated to breaking of integrins bonds, jumps are the one for which integrins is directly linked to the cell's cytoskeleton while tethers are generally providing information about the cell's membrane, and are associated to receptors not anchored to the cell's cortex. In the study that follows, we focus on jump events

and their corresponding mean forces and force distributions as we are studying on active integrins related bond, that are implied in mechanotransduction processes, hence transmitting information from the matrix to the cell.

Mean values of the parameters were calculated for each cell (from 3 FCs) and then further averaged across the cell population for each contact time and condition. The associated errors were calculated as a sum in quadrature of the standard deviation of the mean (across the number of cells or the numbers of events for the case of mean forces) and an instrumental error of 3% previously calculated by propagation of the calibration uncertainties through Monte Carlo simulation [134].

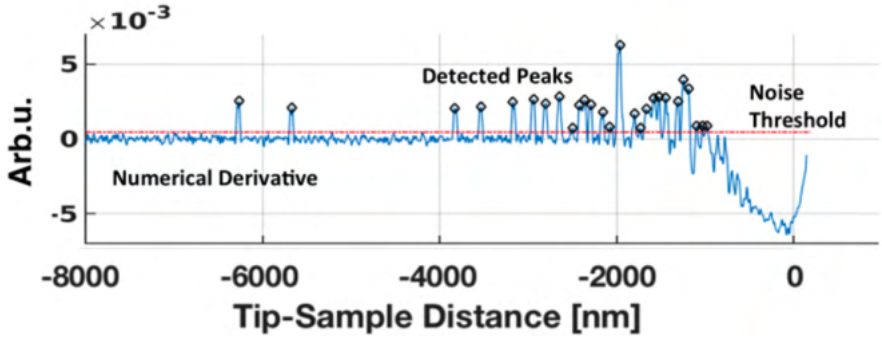

Figure 30. Numerical derivative of a representative FC used to detect events in the retraction part of the FC. Adapted from Chighizola et al.[113].

4.2. Results

We reported in **Figure 31** the mean adhesion, work, and number of jumps for every cell line with glass and protein functionalized probes: fibronectin (Fn) and laminin (Lam). The distribution of the jumps precisely at 60 and 120s contact time for all cell line with laminin and fibronectin are presented in **Figure 33**. The distribution of jumps at 120s for the three cells line, compiled using data from **Figure 33** as well as those from the non-functionalized probes, is shown in **Figure 32**.

4.2.1. Less invasive cell lines exhibit a higher affinity to Laminin

We observed markedly higher adhesion for all cell lines on laminin rather than on glass and Fibronectin, although while for RT4 and RT112 the force reaches a plateau after 60s and 20s contact time, respectively, for T24 cells the force keeps increasing at all contact times. Fibronectin and glass seem to have similar adhesion trends for all contact times and all cell lines (**Figure 31A, B, C**). Glass events were considered as not representative of the cell-ECM interaction as they do not engage any integrins-ECM protein complex.

Furthermore, we examined the work (**Figure 31D, E, F),** which is representative of both typical bond lengths and forces of all events (jumps, tethers) as well as their numbers. This makes the interpretation of the trends of the work not straightforward. The general trend observed in adhesion is observed also for the work: in particular, we see a higher work with laminin, markedly for the RT4 cells, which also show significantly smaller work for glass and fibronectin compared to the other cell lines. The difference between laminin and fibronectin for RT112 cells is lost. RT112 and T24 cells show a similar increasing trend of the work, with an

unexpected rise at 120s for T24 cells, which could be explained by the large maximum adhesion F_a values (doubled from 60s to 120s for T24 cells with laminin).

T24 cell line seems to need longer contact time to reach strong adhesion with laminin, compared to less invasive cells (**Figure 31C**). Interestingly, the number of jumps for RT4 and T24 cell lines seems to be slightly higher with laminin (**Figure 31G and I**)., whereas for RT112 cells it is higher with fibronectin (**Figure 31H**). The number of jumps in general increases with the contact time.

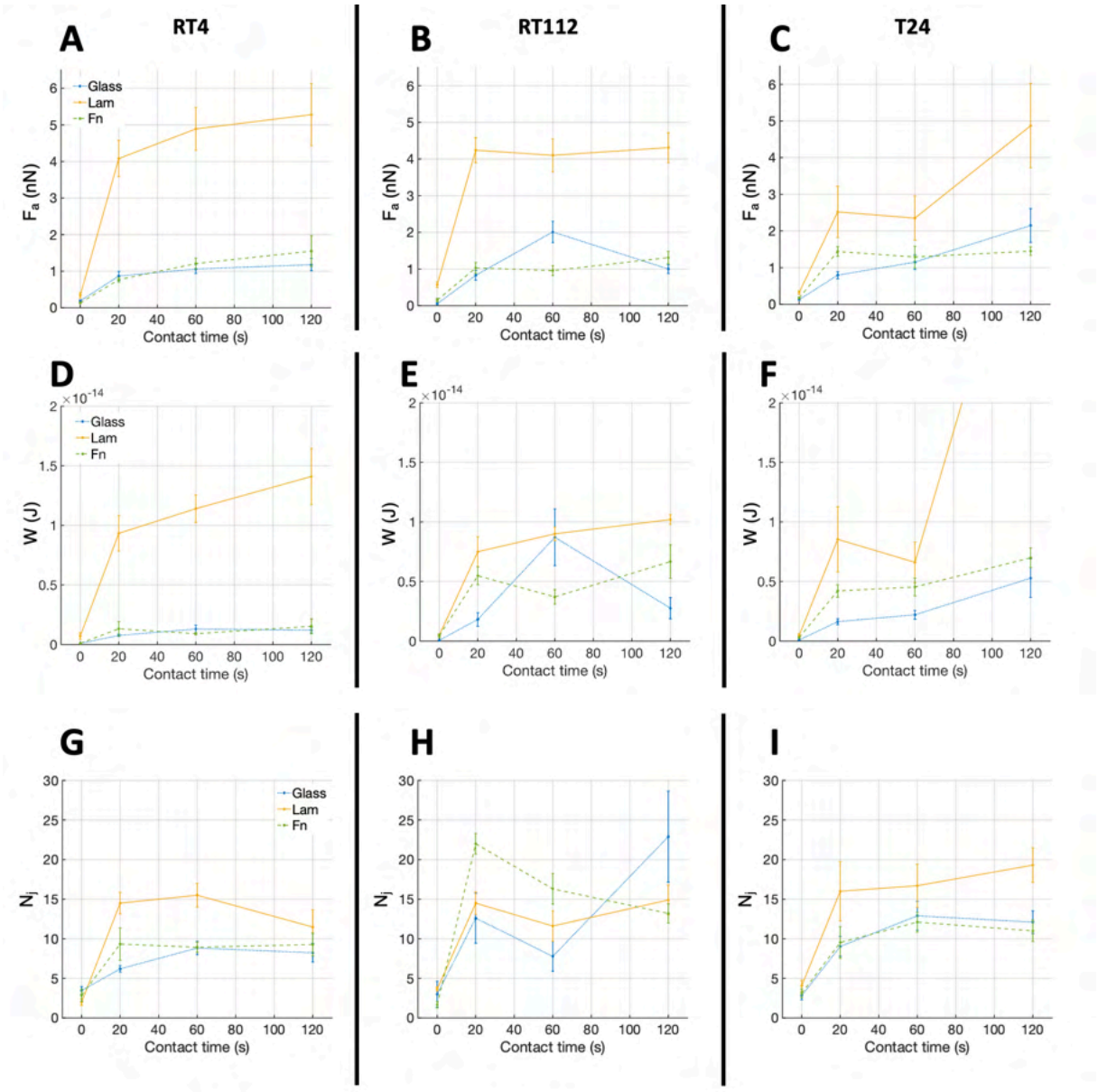

Figure 31. For the three cell lines in order of invasiveness RT4, RT112 and T24, ordered column wise left to right, (A-C) adhesion force F_a, (D-F) work and (G-I) the mean number of jumps per force curve N_j are shown. Errors bars represent the effective standard deviation of the mean as explained in Material and Methods.

4.2.2. Unbinding forces with laminin are stronger than fibronectin in RT4 and RT112 cells.

The forces of jumps at the longest contact time 120s (**Figure 32**), where most of the difference in adhesion, work and the number of jumps is seen, show different distributions according to the cell and protein association.

The distribution of forces for laminin bonds is wider for grade 1 (RT4) and grade 2 cells (RT112), while for the most invasive T24 cells we observe a shift towards weaker bonds and less dispersed distribution (**Figure 32C**). Fibronectin on the contrary display weaker bonds than laminin, with a maximum around of 250 pN; more concentrated between 0 and 100 pN for RT112 cells.

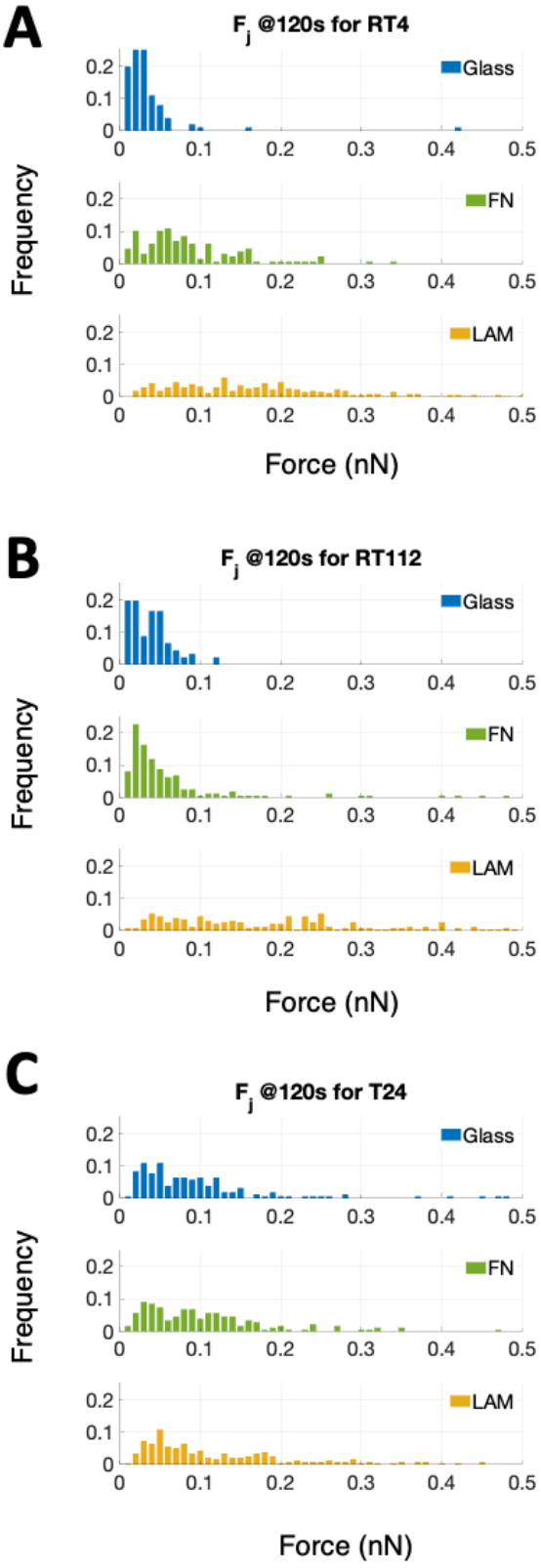

Figure 32. Distribution of forces at 120s for (A) RT4, (B) RT112 and (C) T24 for the three probes: glass (blue), fibronectin (green) and laminin (yellow). Frequency represents the relative frequency counts.

4.2.3. Fibronectin forces do not differ with the contact time for less invasive cells.

While looking at **Figure 33**, we can observe that the forces of fibronectin unbinding did not differ by doubling the contact time for RT4 and RT112. T24 on the contrary seems to have reinforced its fibronectin-cell binding at 120s contact time, seen by the widening of the distribution. This effect is not seen in laminin, where the forces get stronger with respect to the contact time for all cell lines. In general, we observed the weaker laminin related bonds with T24 cells than with less invasive cell RT4 and RT112.

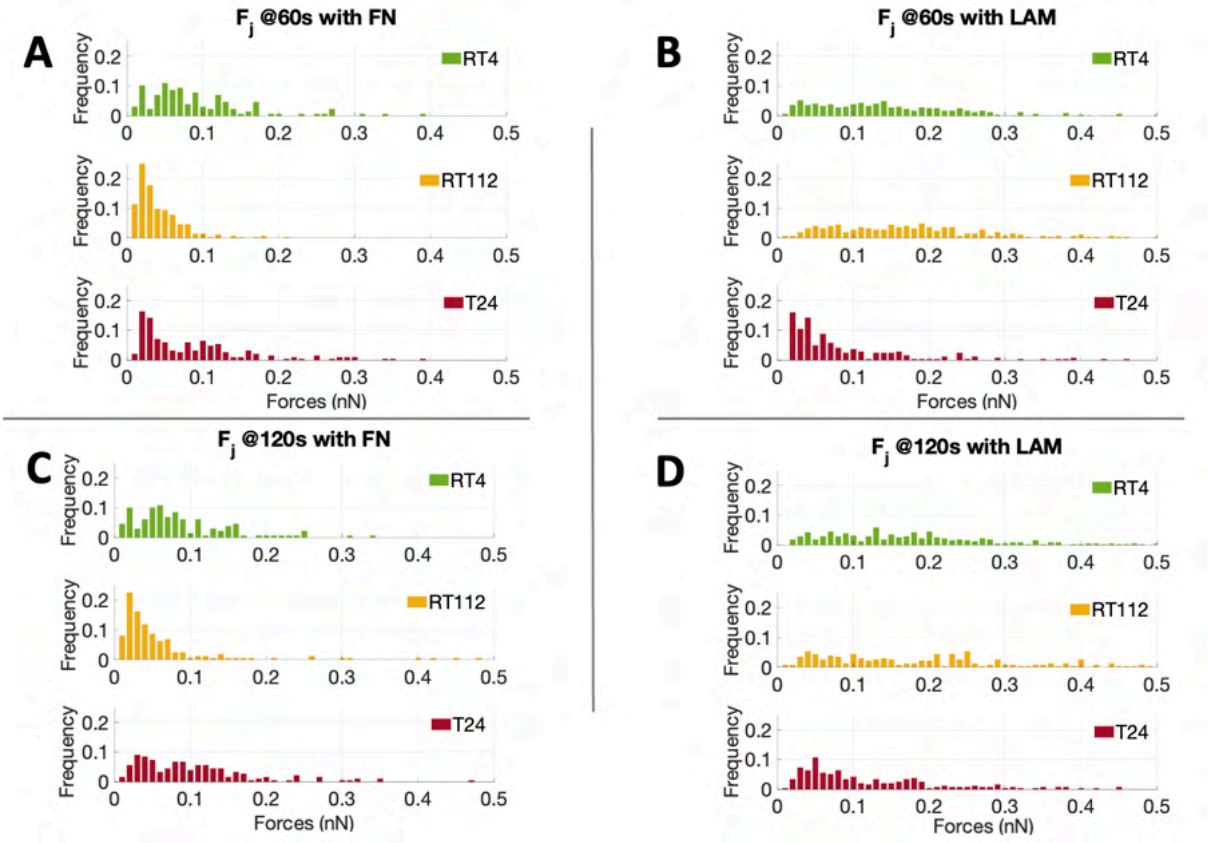

Figure 33. Distribution of force (A and B) s at 60s and (C and D) 120s contact time for all cell lines, with (A and C) fibronectin FN and (B and D) laminin LAM functionalized probes. Containing similar data as in **Figure 32**. Frequency represents the relative frequency counts.

4.3. Discussion and perspectives

In this work, it has been observed a change in the interaction between the cell and the ECM proteins in respect of the cell's invasiveness. Our results demonstrated that T24 cells were less adhesive to laminin compared to their less invasive counterpart. Laminin is an ECM protein of the basal lamina and a strong interaction with an epithelial-like cell such as RT4 and RT112 was expected [4,5], while T24 cells, which represent grade 3 of invasiveness of urinary bladder carcinoma, are closer to the mesenchymal type and therefore are less adhesive towards the ECM and their motifs.

Laminin-related unbinding forces were seen to be generally stronger for grade 1 and 2 cell lines compared to fibronectin ones. Regarding the most invasive cell line T24 it is observed a specific strengthening of the fibronectin bonds with respect to the contact time, that is not observed in RT4 and RT112. Taubenberger et al.' observed that cell adhesion with collagen was slowly increasing in the first 60s and was strongly reinforced after that time [182], it might be an indicator of integrin clustering and reinforcement of the original bond that could be studied via live fluorescence imaging [103].

With this approach, we can confirm the general hypothesis that during EMT, here represented by different grades of invasiveness, those cells interact differently with their microenvironment. More invasive cells were demonstrated to have less affinity with epithelial markers like laminin, and slightly stronger with fibronectin; protein that has been in multiple paper, associated with cell invasion and helping in building niche for neovascularization[183,184]. The forces related to those fibronectin-binding were in general, shown to be weaker than the laminin counterpart in less invasive cell lines.

The fact that the cell-probe events associated with ECM proteins (laminin, fibronectin) are in the same force range as one of those measured on the bare glass surface (**Figure 32**), which is supposed to provide unspecific protein-cell binding, could give rise to concerns regarding the nature of the unbinding events characterized. Glass has been selected in this experiment as a negative control, representative of a non-functionalized probe, to give us an idea of the range of forces expected for non-specific protein-protein interactions. As explained in General Material and Methods, measurements were made in cell media without phenol red. The proteins in the cell's medium, which are primarily derived from FBS, might have adsorb onto the probe glass surfaces and caused a minimal amount of binding between the glass and the cell. Due to time constraints, controls to confirm the precise nature of those interactions between glass with the three-cell lines were not performed.

Integrin and in general CAMs related bonds are calcium-dependent [90,185], among all the possible approach to assess the nature of the integrins related bond, one could be the addition (or reduction) of calcium within the medium. Inhibition of specific integrin subunit: targeting $\beta 1$ that regulates most of the laminin related bonds, or αV for fibronectin for example (**Figure 3**) is also a possibility.

Although the effectiveness of the functionalization procedure was accepted as following established protocols [128–130], it is still considered that additional research is required to confirm the firmly attached nature of the proteins to the probe. As an example, the addition of a PEG chain to the functionalization (between the glass and the protein), might provide more flexibility for the protein to interact with the cells.

Finally, as demonstrated in the article Holuigue et al. in the Introduction, the three cell lines exhibit different Young's Modulus, the most invasive T24 being significantly softer than the less invasive RT4. During Force Spectroscopy, the maximum loading force has been kept at 1nN for the three systems, and one could argue that the different indentation of the cells could induce a larger contact area, consequently leading to a higher adhesion and/or higher number of available receptors for binding. The presented data are not normalized according to the contact area, In *in vitro* conditions, the invasive cell's cytoskeleton rearrangement/softening is also part of their change toward mesenchymal phenotype and consequently, those cells can have a different perception and/or adjustment to their microenvironment. The estimated maximum relative change (from RT4 to T24) in the contact

area is 10%. Cells, however, dynamically modulate the contact area during the development of an adhesive interaction, to an extent that probably overtakes the difference in contact area due to the contact mechanics predictions. We think therefore that the absence of a normalization with respect to the contact area, besides being probably not reliably implementable, does not introduce a strong bias in our data and conclusions. This issue deserves further attention in the future.

The force spectroscopy experiments performed with a single ECM protein attached to the tip is an oversimplification of a more complex system, which does not represent faithfully the reality of the complex 3D ECM network interacting with the cells. The production of functionalized AFM probes that better mimic the ECM complexity could provide stronger insight into the interaction between cells and their microenvironment. While one of the approaches could be the engineering of more complex probes, with a combination of more ECM components [130], we have addressed this issue by developing fully native ECM probes. They should allow us to achieve a deeper understanding of the cell-microenvironment interaction and characterize the specific adhesive properties of selected cells against selected ECMs. Proof-of-principle of the production, characterization, and application of native ECM probes is presented in the following chapter, Chapter 3.

5. Chapter 3

Production and characterization of native ECM probes for adhesion force spectroscopy studies of the cell-microenvironment interactions

This Chapter focuses on the development of an innovative way to study cell-microenvironment interaction using AFM in force spectroscopy mode. While many aimed at mimicking the ECM environment via functionalization of probes with ECM proteins [21,86,97] including collagen [90,130] or using nanostructured probes to reproduce the ECM nanotopography[113], we wanted to get one step closer by reproducing the ECM microenvironment by attaching a piece of native ECM to the tip and perform adhesion force spectroscopy experiments on target cells.

To this purpose, we designed, produced, and characterize native ECM probes for AFM using a combination of decellularization procedures, Laser Microdissection (LMD) and AFM. This work has been carried out in collaboration with Dr. Massimo Alfano (Ospedale San Raffaele, Milano) and Dr. Giuseppe Diaferia (Instituto Europeo di Oncologia, Milan).

A preprint currently on BioRxiv, “Novel native extracellular matrix probes to target patient- and tissue specific cell-microenvironment interactions by force spectroscopy”, doi: 10.1101/2022.12.02.518867, present the results of this work. Reported here as a major part of this Chapter the updated version, containing modification on the control experiments.

Native extracellular matrix probes to target patient- and tissue- specific cell-microenvironment interactions by force spectroscopy

H. Holuigue[1], L. Nacci[2], P. Di Chiaro[2], M. Chighizola[1], I. Locatelli[3], C. Schulte[1], M. Alfano[3*], G.R. Diaferia[2,*], A. Podestà[1,*]

[1] CIMAINA and Dipartimento di Fisica "Aldo Pontremoli", Università degli Studi di Milano, via Celoria 16, 20133 Milano, Italy.
[2] Department of Experimental Oncology, IEO, European Institute of Oncology IRCCS, Milano, Italy.
[3] Division of Experimental Oncology/Unit of Urology, URI, IRCCS San Raffaele Hospital, Milan, Italy.
*Corresponding authors: alessandro.podesta@mi.infn.it, alfano.massimo@hsr.it, giuseppe.diaferia@ieo.it

Abstract

Atomic Force Microscopy (AFM) is successfully used for the quantitative investigation of the cellular mechanosensing of the microenvironment. To this purpose, several force spectroscopy approaches aim at measuring the adhesive forces between two living cells and also between a cell and a suitable reproduction of the extracellular matrix (ECM), typically exploiting tips suitably functionalised with single components (e.g. collagen, fibronectin) of the ECM. However, these probes only poorly reproduce the complexity of the native cellular microenvironment and consequently of the biological interactions.
We developed a novel approach to produce AFM probes that faithfully retain the structural and biochemical complexity of the ECM; this was achieved by attaching to an AFM cantilever a micrometric slice of native decellularised ECM, which was cut by laser microdissection. We demonstrate that these probes preserve the morphological, mechanical, and chemical heterogeneity of the ECM.
Native ECM probes can be used in force spectroscopy experiments aimed at targeting cell-microenvironment interactions. Here, we demonstrate the feasibility of dissecting mechanotransductive cell-ECM interactions in the 10 pN range. As proof-of-principle, we tested a rat bladder ECM probe against the AY-27 rat bladder cancer cell line. On the one hand, we obtained reproducible results using different probes derived from the same ECM regions; on the other hand, we detected differences in the adhesion patterns of distinct bladder ECM regions, such as submucosa and detrusor, in line with the disparities in composition and biophysical properties of these ECM regions.
Our results demonstrate that native ECM probes, produced from patient-specific regions of organs and tissues, can be used to investigate cell-microenvironment interactions and early mechanotransductive processes by force spectroscopy. This opens new possibilities in the field of personalised medicine.

Keywords. Atomic Force Microscopy (AFM), laser microdissection (LMD), adhesion force spectroscopy, extracellular matrix (ECM), cell-microenvironment interaction.

1. Introduction

Cells and their microenvironment have a strong intercommunication and interplay, influencing each other. The extracellular matrix (ECM) surrounding the cells is mainly composed of a three-dimensional network of collagen and crosslinked proteins, such as fibronectin and laminin; ECM from various tissues can have strong differences in their composition and biophysical properties (i.e., rigidity and structural features, such as nanotopography) [1–4]. Cells use the ECM as a scaffold for their anchorage and interact with it in a reciprocal manner. Cells can convert external mechanical and topographical stimuli into biochemical signalling, which often determine changes in the mechanical properties of the cell through the reorganisation of the cytoskeleton and modulates gene/protein expression, a process called mechanotransduction. Cells are therefore able to perceive changes in the physical properties of their surrounding ECM. The cell itself uses force to sense the biophysical characteristics of the ECM. The study of these reciprocal interactions pertains to the fields of cellular mechanobiology [5–12].

Different techniques are used to study these cell-ECM interactions, among which Atomic Force Microscopy (AFM) stands out due to its ability to both sense and apply forces at the nanoscale, with sub-nanonewton sensitivity [13–17]. In the context of biophysical investigations, many AFM-based force spectroscopy (FS) configurations can be found [18]: a single-cell probe approaching a substrate coated with proteins [19–24]; an ECM-mimicking probe approaching an adherent cell [11,25–29]; a single-cell probe approaching an adherent cell [15,30,31]. Both cell-cell and cell-ECM interactions can be investigated, through the direct measurement of faint (10-100 pN) interaction forces, which are mostly cadherin or integrin related, respectively [32–36].

The main advantage of FS techniques using tips functionalised with single proteins [26,28,29] is the simplification of the complex cell-microenvironment interface, allowing us to study one specific molecular interaction at a time. An example for this approach for the study of cell-ECM interactions consists in the functionalisation of AFM tips with collagen, a major component of the ECM [29,37]. While these methods enable an accurate characterisation of specific molecular interactions, the reconstituted interface is poorly mimicking the complexity of the native interface in physiological conditions.

Aiming at reproducing the native cell-ECM interface within a typical AFM-based FS experiment, we developed native ECM probes and demonstrated that they can be

reliably used to scrutinise integrin-related adhesive interactions between cells and their microenvironment. Attaching the ECM to the cantilever and ramping it against adherent living cells, instead of using single-cell functionalised cantilevers against an ECM sample, is advantageous, among other reasons, because it allows to test i) many different cells with the same probe, that can be used and re-used repeatedly, and ii) cells seeded on different substrates, i.e. polarized or with different phenotypes such as type 1 and type 2 macrophages or epithelial cancer cells or cancer cells during and after epithelial-mesenchymal transition. Indeed, the ECM is more stable and easier to handle than living cells, and each single-cell probe requires a different cantilever and a new calibration; overall, using ECM probes more likely provides improved reliability and statistics of the FS experiments.

Here we describe the fabrication approach of novel native ECM probes and the results of their characterisation, showing that the chemicophysical properties of the native ECM are preserved, also after intense and prolonged use. We also report on the application of these new probes in adhesion force spectroscopy experiments, showing that the peculiar patterns of adhesive molecular interactions observed in FS experiments were reproduced. As a proof-of-principle, we focused on rat bladder - derived ECM and used the rat bladder tumour cell line AY-27 as a suitable interaction partner. The described protocol is, however, universally applicable, and allows to reliably fabricate probes out of any ECM, and even from specific regions of the same ECM, to be tested against both immortalised and primary cells, paving the way to the investigation of patient-specific cell-ECM interactions.

2. Results and Discussion

3.1 Production of native ECM-probes for adhesion force spectroscopy

To produce native ECM probes, we developed a novel approach based on the cutting of ECM pieces from a glass-supported, decellularised ECM slice; these pieces will then be detached from the glass slide and attached to tipless functionalised cantilevers (Figure 1A-D).

To cut pieces with predefined and reproducible dimensions and shapes from the ECM slice, we used an LMD apparatus (in Figure 1A, square cuts with 20µm x 20µm area are shown).

LMD is typically used to cut a selected area from a dehydrated tissue section attached on the upper surface of a glass slide, where a thin plastic membrane is cemented to the glass at its edges leaving a rectangular area with air trapped between the membrane and the glass backbone (Figure S1A-C). A focused UV laser then cuts the selected regions of the tissue, together with the plastic membrane allowing the microdissected pieces to fall by gravity in a reservoir located below. These samples are then typically digested for genomics or proteomics assays [38,39], where the presence of the rigid plastic membrane does not interfere with the subsequent molecular reactions.

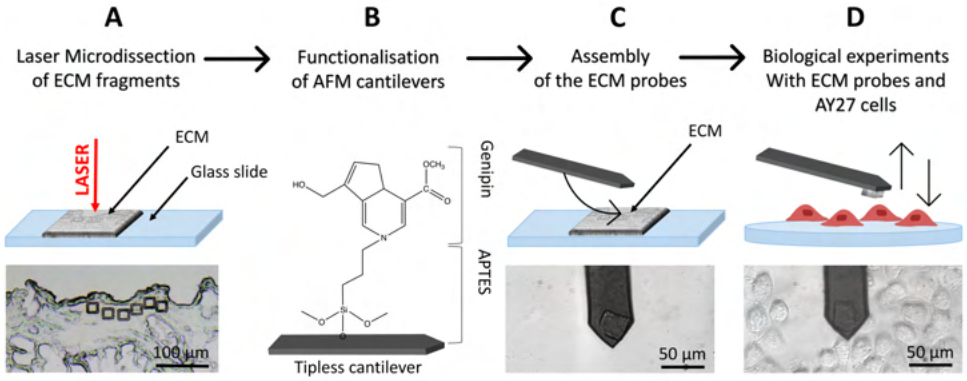

Figure 1. Schematics of the ECM probe production. (A) Optimised use of the LMD system to produce native ECM-probes, keeping the ECM directly on the standard microscope glass slide, used without the plastic membrane, resulting in ECM fragments physically separated from the surrounding matrix. (B) Tipless cantilevers are functionalised with APTES and genipin (covalently bonded), and then used for the attachment of the ECM probes (C), exploiting the XY micro-translation stage of the optical microscope that includes the AFM (stand-alone stages can be used equivalently). (D) The resulting ECM-probes are used for biological experiments, such as force spectroscopy measurements on top of living cells.

For our application, given that the objective is to transfer and attach intact fragments of ECM to either AFM tipless cantilevers or spherical tips, the presence of the plastic membrane is detrimental. We therefore modified the standard LMD procedure to develop an optimised approach, based on the elimination of the plastic membrane from the glass slide and the introduction of suitable procedures to detach the cut pieces from the slide and to transfer them to the AFM cantilever or tip.

The protocol is represented schematically in Figure 1. Here, the laser is still used for the cut, but the ECM slices are attached directly on the glass slide, without the plastic membrane in between (Figures 1A and S2A) and placed on the microscope, with the tissue facing up. After the cut, the microdissected pieces remain on the glass surface

(Figures 1A and S2B-D), separated from the surrounding ECM by a narrow empty region vaporised by the laser, where they can be picked up by, and deposited onto, the functionalised cantilever used for the assembling of the ECM probe, exploiting the XY motorised stage of the AFM integrated in the optical microscope (see Supporting Movies SM1-SM3). This procedure takes place in liquid. After the attachment, the cantilever is withdrawn from the surface and kept at rest for 10 min. ECM probes were typically stored in PBS at 37°C in a humid environment (for example in the cell incubator) and used in the following days.

The fact that the ECM pieces remain on the glass slide after the cut facilitates the investigation of same or twin specimens by other techniques, like immunofluorescence. Moreover, having the ECM attached to the cantilever and testing it against a cell population cultured on a suitable support is very convenient compared to having a single cell probe that interrogates an ECM sample; indeed, in the first case many cells can be tested with the same ECM probes, while in the standard configuration each new tested cell requires the preparation of a new probe.

In this work, 20µm x 20µm, 10µm thick squares (Figure 1A) were cut in different regions of decellularised rat bladder: submucosal, detrusor and adventitia [17,40,41].

3.2 Characterisation of ECM and ECM probes

LMD provides many advantages including the possibility to precisely select the ROI, cut ECM pieces with predefined, reproducible geometry and dimensions, and collect the samples without damaging them. To ensure that the ECM pieces retain the properties of the pristine ECM, we performed several assessments of biophysical and compositional parameters.

Firstly, we controlled the possible effect of the laser cut on morphology, mechanics and composition of the ECM, respectively, through combined AFM topographic and nanomechanical measurements (Figure 2) and quantitative immunofluorescence staining (Figure 3). For the nanomechanical assessment of the ECM, we measured the region inside and outside the microdissected piece; the inner region is the one that it is then attached to the AFM cantilever, while the outer region is taken as reference for the untreated ECM. For the immunofluorescence analysis, we measured the fluorescent signals detected after immunostaining from the inner regions of the microdissected pieces and the same regions from a consecutive section obtained from the same ECM specimen not subjected to laser ablation.

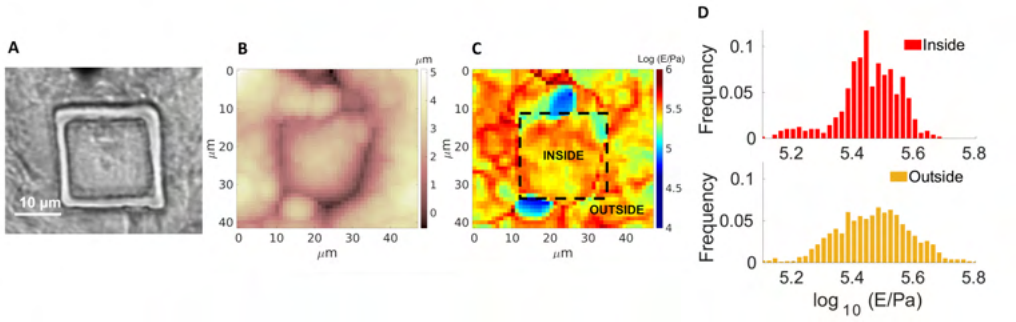

Figure 2. (A) Optical image, (B) Young's modulus and (C) topographic maps of an ECM slice with the cut of the laser clearly visible (highlighted in C). (D) Distribution of the measured Young's Modulus values for the internal and external regions of the cut.

Figure 2A-C shows the optical image of a cut ECM piece together with AFM topographic and mechanical maps. The borders of the cut region are clearly visible in both optical image and topographic AFM maps. No evident differences between the inner and the outer regions are visible, regarding both morphological and mechanical properties (the median Young's modulus values are 280 and 289 kPa for the internal and external parts, respectively). Besides the medians, also the distributions of Young's modulus values E (Figure 2D) are similar (the distribution of the external part is slightly broader, which can be explained by the larger covered area, encompassing a larger heterogeneity of the sample).

These results are in line with the results obtained by quantitative staining of major ECM proteins such as collagen, laminin, and fibronectin on different cut pieces of ECM, demonstrating that the composition of the matrix is not affected by the cut (Figure 3). The UV laser of the LMD apparatus could induce thermal damage and autofluorescence [42], and fibronectin inactivation [43] around the edge of the ablated region; nevertheless, the central area used for the production of the probes and interacting with the cells is not affected by these phenomena.

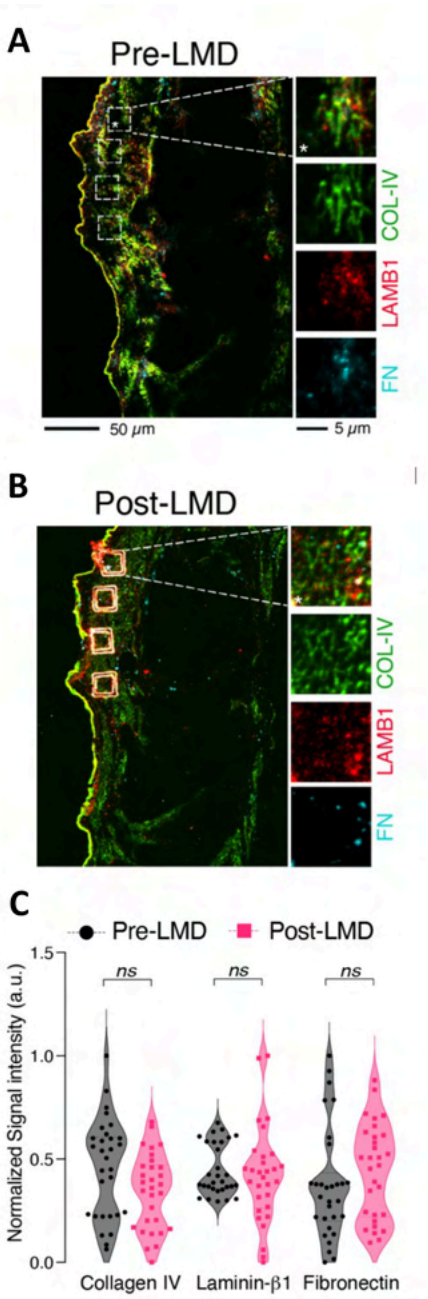

Figure 3. Immunostaining for Collagen IV (COL-IV, *green*), laminin β1 (LAMB1, *red*), and fibronectin (FN, *cyan*) before (A, Pre-LMD) and after (B, Post-LMD) the cut. The white boxes in the Pre-LMD image represent the matched area subjected to microdissection. (C) Quantification of the fluorescent signal associated to the different proteins in each ROI (white squares). The data represent normalised fluorescent signal (a.u., arbitrary units) scaled between 0 and 1 (n=30, 5 ROIs per each field, 6 fields acquired distributed along the layers of the bladder).

Stress tests were performed to assess the firm attachment of the matrix to the cantilever and the force spectroscopy functionality after repeated use. The ECM remained attached to the cantilever after scanning continuously in Contact Mode on a glass slide for 1h (Figure S3A); similar adhesion forces were measured during continuous acquisition of 400 FCs (Figure S3B).

To further assess the lifetime of ECM probes, in particular the structural resistance of the ECM fragments, the firmness of their attachment to the cantilevers and their capability to sense reliably molecular interactions, we performed adhesion force spectroscopy experiments during two consecutive days (day 1 and day 2) on cells from the same passage plated on two different petri dishes. We observed that the probe detected similar mean number of jumps N_j (Figure S4A), with some discrepancies at higher contact times, and very similar force per jump $<F_j>$ (Figure S4B). Remarkably, besides the satisfactory agreement of the mean N_j and $<F_j>$ values, the distributions of the measured single-bonds forces for the two days for the same contact times agree very well (Figure 4A,B), and also clearly show that there is an increase of the force at higher contact times. This leads us to conclude that the same probe in different days is able to measure the same adhesive events, i.e. the probe maintains its ability to capture both qualitatively and quantitatively the biological picture of the adhesive cell-ECM interaction. The slight difference observed from day to day in the measured parameters could be explained by the well-known heterogeneity of cells, as well as by their high sensitivity to slight changes in the environmental conditions.

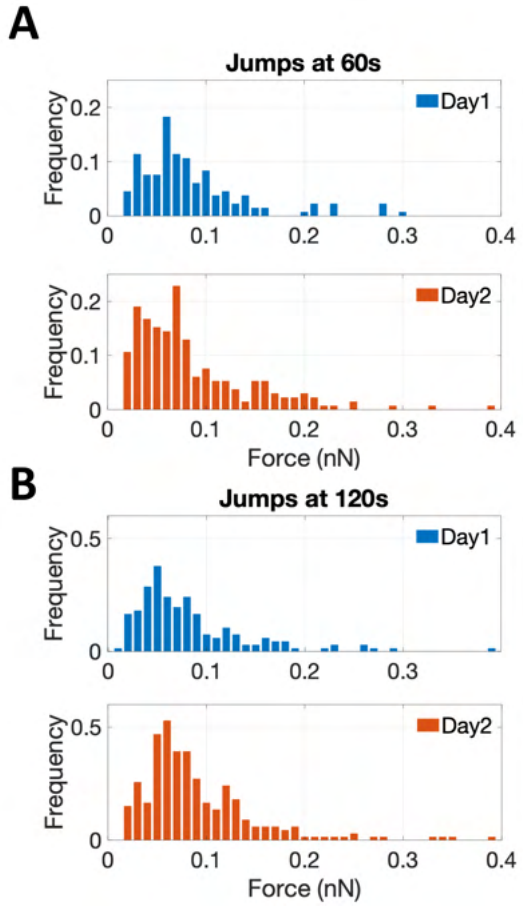

Figure 4. Results of the adhesion force spectroscopy measurements performed with the same ECM probe in two consecutive days (day 1 in blue and day 2 in red) on AY-27 cells from the same passage. The distributions of the force of single jumps at two contact times are shown in (A) (ct=60s) and (B) (ct=120s).

3.3 Use of tailored native ECM probes in adhesion force spectroscopy experiments

To demonstrate the potential of native ECM-probes for the study of cell-microenvironment interactions, we carried out adhesion force spectroscopy experiments with these probes against AY-27 cells.

For the proof-of-principle presented here, we selected two main bladder regions for the creation of the ECM probes: the submucosal region, closer to the lumen of the bladder, rich in connective tissue to support the attachment of the urothelium, a type of stratified epithelium made of transitional epithelial cells, and the detrusor region, a

central layer of the bladder made of muscle fibres that allow contraction [40,41], as shown in Figure 5A-C. The ECM probes, named after their corresponding region of origin (Probe SM, submucosal, and Probe D, detrusor) are interesting because, albeit deriving from adjacent areas of the same bladder tissue, they are characterised by major differences in the composition and mechanical properties [17,40].

We performed immunostaining and quantification of the abundance of principal ECM proteins, such as collagen, laminin, and fibronectin, which are responsible for major integrin-mediated cell/ECM interaction in the bladder tissue (Figure 5D,E). We observed a lower frequency of occurrence of collagen IV in detrusor, compared to submucosal and adventitia regions of the ECM (Figure 5E).

While laminin seems to be consistent in all the matrix, fibronectin is more present in the detrusor compared to the other two proteins. We furthermore observed different mechanical properties of the ECM regions (Figure S5), in agreement with the results recently reported for the three tissue layers of the rat bladder (i.e., urothelium, lamina propria and muscle layer)[17]. These assessments confirm that the different parts of the bladder ECM reproduced by Probe SM and Probe D exhibit significant distinctions in their compositional and biophysical features.

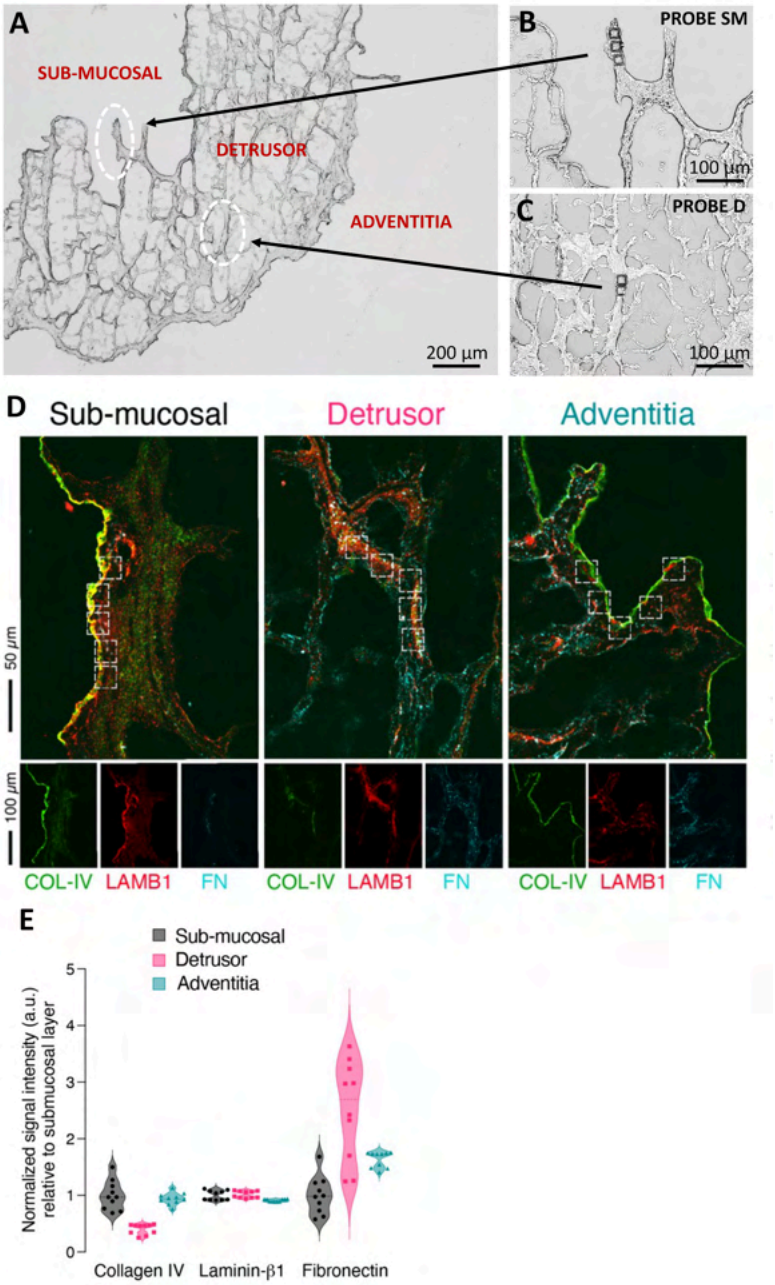

Figure 5. Optical images of the ECM before (A) and after (B and C) the LMD cut. The white circles highlight the regions of the cuts, from where the ECM probes have been produced: probe SM from the submucosal, and probe D from the detrusor. The denomination of the specific regions of the bladder in (A) follows Refs [40,41]. (D) Immunostaining of different regions of the decellularised bladder (submucosal, detrusor and adventitia) with collagen IV (COL-IV, *green*), laminin β1 (LAMB1, *red*), and fibronectin (FN, *cyan*). (E) Quantification of the fluorescent signal associated to the different proteins in each ROI (white squares). The data represent normalised fluorescent signal (a.u., arbitrary units) relative to the mean value of the submucosal layer for each matrix (n=10, 5 ROIs per each field, 2 field acquired per each layer).

We then performed adhesion force spectroscopy experiments comparing Probe SM and Probe D against AY-27 cells. For both substrates, N_j rose initially (0-60s) and then remained nearly constant. While no clear difference is seen in the number of jumps (Figure 6A), we observed important differences between the two ECM probes in both $<F_j>$ (Figure 6B) and F_a (Figure 6C). For both parameters, the values were higher for the SM substrate at almost all time points. The maximum adhesion force for Probe SM reached ~1.5 nN, compared to only ~0,5 nN for Probe D. A similar outcome was detected for $<F_j>$.

Remarkably, the distribution of the forces of jump unbinding events (Figure 6D,E) are very different for the two probes. For Probe SM, a more ample spectrum with occurrence of higher forces per jump was noted, whereas for Probe D the forces are restricted to lower values. Moreover, at longer contact times we observed a moderate shift towards lower forces for Probe D, while in the distribution of Probe SM the frequency of both smaller and higher forces increased slightly.

These results demonstrate that our approach allows to produce ECM-probes from different regions of a tissue with tailored adhesive properties, to sense qualitatively and quantitatively different molecular interactions. The unbinding events might be attributable to different types of bonds, i.e., cell-fibronectin or cell-collagen IV interaction, depending on the ECM portion attached to the probe. Since AY-27 rat bladder tumour cells are derived from a urothelium transitional carcinoma,[44] they likely express those receptors that bind ECM components present in the submucosal layer, since this region of the bladder allows urothelial cells attachment, as mentioned above. The probe derived from the fibronectin-dominated, muscular type detrusor layer is probably less ideal for AY-27 attachment therefore explaining the poorer affinity observed. The increase of the frequency at higher forces at longer contact times for Probe SM is congruent with the transition from single to cooperative α2β1 integrin receptor binding to collagen I during the early steps of adhesion, shown by Taubenberger et al[45]. In the fibronectin-prevalent Probe D condition this does not occur (the trend is more in the opposite direction). However, the forces measured for the first pristine adhesion events to Probe D at 0s are in the range of what was measured for α2β1 integrin/fibronectin binding by Sun et al. (39±8 pN versus 36±9 pN in our measurements, see Table 1). The lower binding force and the lower adhesion pattern measured with Probe D are consistent with the invading character of cancer

cells in the inner muscular detrusor layers of the bladder[46,47], which is necessary for the tumour to become muscle invasive. Altogether, the specific adhesive features measured with the two ECM probes are in line with the composition of the native ECM portions (Figure 5D,E) and distinct types of cell-ECM interactions.

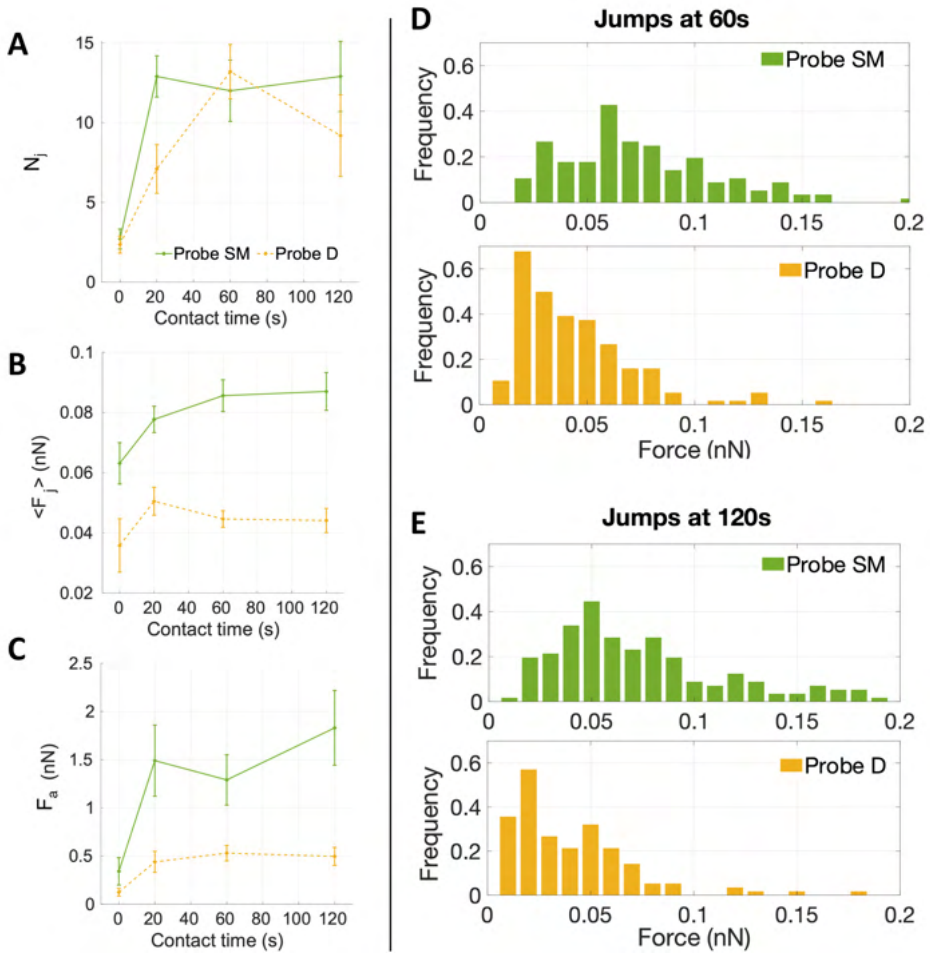

Figure 6. The figure shows the results of adhesion force spectroscopy measurements performed with two different ECM probes on AY-27 cells of the same passage: Probe SM (green) and D (yellow), obtained using ECM fragments from submucosal and detrusor regions, respectively. Four different cell/probe contact times have been tested (ct = 0 s, 20 s, 60 s, 120 s). (A-C) The mean number of events (jumps) N_j, the mean force per jump $<F_j>$, and the mean total adhesion force F_a as a function of the contact time, respectively. (D,E) The distributions of the force of single jumps at two contact times (ct=60s and 120s, respectively). Error bars in A-C represent effective standard deviations of the mean, as explained in the Methods.

Table 1. Mean forces per jump at contact times 0, 20, 60 and 120 seconds.

Contact time (s)	0	20	60	120
Probe SM	63±7	77±4	85±5	87±6
Probe D	36±9	51±5	45±3	45±4

To validate the association of measured jumps to integrin-related events, we performed a control experiment treating the cells with an allosteric inhibitory antibody against β1 integrin (4b4), at fixed contact time (ct=60 s), using two ECM probes made from a submucosal region (Probe CTRL1 and CTRL2, Figure S6). The major component of the submucosa is collagen IV (Figure 5D,E), which is bound by α1β1 and α2β1 integrins, targeting β1 was then strategical. We observed force of adhesion, mean force of jumps and tethers and mean number of events before and after the addition of 4b4 (Figure 7). We considered both jumps and tethers as representative events in these experiments, since the inhibitory antibody targets all β1 subunits of the integrins, either linked to the cell cytoskeleton (jumps related events) or not (tethers)[45,48–50]. The two ECM-probes CTRL1 and CTRL2 (Figure S6) were used on two consecutive days and data were grouped together, as it was observed that the force of events were similar and displayed similar distributions (Figure S7).

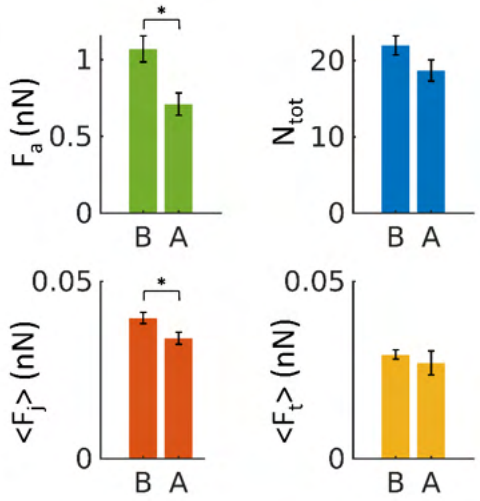

Figure 7. The mean force of adhesion F_a, mean number of events N_{tot} (both jumps and tethers) and mean force of jumps and tethers measured $<F_j>$ and $<F_t>$ respectively, using control probes CTRL1 and CTRL2 before (B) and after (A) the addition of the 4b4 inhibitory antibody against β1 integrin at concentration of 5μg/ml. Errors represent effective standard deviations of the mean, as explained in the Methods.

Figure 7 shows a significant decrease upon exposure of cells to the antibody of the total adhesion force F_a as well as the mean force of jumps $<F_j>$. A decrease of the total number of events N_{tot} (jumps and tethers) and the mean force of tethers $<F_t>$ was also observed, although not significant. These results confirm that the measured interaction forces depend at least partially on β1 subunits of integrin proteins.

3. Conclusions

In the current work, we presented a novel adhesion force spectroscopy approach for the study of the cell-microenvironment interaction obtained by attaching selected pieces of native ECM to an AFM tipless cantilever, exploiting laser microdissection. These probes reproduce the full complexity of the cell-ECM interface in the physiological condition, in terms of both biophysical cues and composition.

We demonstrated, as proof-of-principle, the functionalisation of AFM cantilevers with native rat bladder ECM pieces from different regions of the tissue, and the use of these novel probes in adhesion force spectroscopy experiments against bladder cancer cells AY-27.

With this novel strategy, we could highlight differences in the adhesive pattern between the AY-27 cells and the ECM when isolated from the submucosa or the detrusor layer. The lower adhesion force detected when the detrusor ECM was used highlights the relevance of our strategy to investigate the impact of cell-ECM adhesion on tumour invasion [46,47]. An added value of our approach is that its spatial resolution allows measurements at the single cell level, and thus it could be used to assess the heterogeneity of neoplastic clones.

The robustness and durability of the ECM probes were demonstrated by stress tests performed both in ramping and contact scanning modes. In addition, we showed the ability of this approach to reliably and repeatedly detect specific integrin-related events, as well as to assess significant differences in the mechanotransductive parameters such as the mean number and force of unbinding events, and their distribution, depending on the ECM region used to produce the probe. The observed differences correlate with the differences in the ECM protein and collagen composition and biophysical properties, revealed by the immunostaining and mechanical analysis.

Our results demonstrate the potential of these novel AFM probes to perform highly specific force spectroscopy investigations. Indeed, the adhesive properties of the probes can be tailored by selecting the type and the specific region of the ECM. The

target cells can also be selected to probe specific mechanotransductive and mechanobiological interactions.

For example, experiments can be performed probing different types of matrices against a wide variety of cells (both healthy, tumoural, and from metastatic sites). Both ECM and cells could be extracted from different organs and tissues of the same patient, which might find application in identifying biomarkers for early diagnosis of diseases (particularly the context of cancer and metastasis, but also other diseases). This could allow in-depth understanding of disparities in the cell/microenvironment interaction between healthy, tumoural and metastatic cells confronted with different ECM substrates. The approach can also be used to test the effects of chemotherapeutic drugs targeting mechanotransduction-associated key players (such as integrins or Rho signalling-related proteins) and structures (e.g., components of the ECM, glycocalyx, and cytoskeleton) in pathophysiological conditions, with a very high precision at the level of forces and number of adhesion sites.

This novel adhesion force spectroscopy approach is therefore characterised by a high potential versatility, which could be a key element in the nanotechnological toolkit of nascent personalised medicine.

4. Material and methods

Cells

The rat bladder cancer cell line AY-27 (Sigma-Aldrich, cat. number SCC254) was authenticated for lack of cross-contamination by analyzing 9 short tandem repeats DNA (IDEXX Bioanalytics, Ludwigsburg, Germany)[51]. The cell line was cultured in RPMI 2mM L-glutamine with 10 % FBS, 1% penicillin/streptomycin and 1% amphotericin; cells were cultured in an incubator at 37°C and 5% CO_2 (Galaxy S, RS Biotech). All reagents and materials are from Sigma Aldrich, if not stated otherwise.

For AFM measurements, the cells were plated one day before on glass bottom petri dishes (∅ 40 mm Willco Wells) coated with poly-l-lysine (0.1% w/v for 30 min at room temperature), in the same RPMI medium without phenol red.

Extracellular Matrices

The bladder from healthy rat was decellularised following the protocol from Genovese et. al [52], validated also for bladder[53]. The ECM samples were embedded in optimal cutting temperature compound (OCT), frozen in dry ice and kept at -80°C. All procedures and studies involving mice were approved by the Institutional Animal Care and Use Committee of San Raffaele Scientific Institute, and performed according to the prescribed guidelines (IACUC, approval number 942). Adult (9-10 weeks old) female Fischer rats were from Charles River Laboratories, Italy.

For the laser microdissected slices, 10μm thick ECMs were cut with a cryostat and mounted onto classical optical microscopy glass slides. The sample was then immerged in PBS to remove OCT and then in Ethanol 70% to dehydrate it prior to laser microdissection.

We tested the effect of dehydration of the ECM and we confirmed that this process does not alter the mechanical properties of the matrix. For the comparison of mechanical properties before and after dehydration, an ECM slice was first characterised after gently washing away the OCT with PBS, then dehydrated in 70% EtOH (following the same procedure used for LMD) and measured again (Figure S3C).

Two different slices were used for the comparison of morphological and mechanical properties of the inner and outer regions of the LMD cut.

For AFM mechanical experiments, 50μm thick ECMs were cut with a cryostat and attached to super-frost microscope glass slides. The prepared ECM slices were kept at -20°C prior to the AFM experiments. Before starting the AFM measurements, the slices were washed with PBS to remove the OCT.

Reagents

For the functionalisation of the probes, 3-aminopropyl triethoxysilane (APTES) and Genipin were used, both purchased from Sigma. Genipin was diluted in 1,5% (v/v) in PBS. 4b4 antibody was purchased from Beckman Coulter.

Laser Microdissection (LMD)

400 μm^2 (20μm x 20μm) regions were cut using a UV-based LMD7 laser microdissection system (Leica Microsystems) at 20x magnification placing the slide

with the ECM section facing up. This setup allowed to separate the regions of interest (ROIs) from the rest of the tissue without detaching them from the glass. The engraved sections were kept dry at 4°C until further processing.

Atomic Force Microscopy

All the experiments have been performed using a Bioscope Catalyst AFM (Bruker), mounted on top of an inverted optical microscope (Olympus X71). The system was isolated from the ambient noise placing the AFM on top of an active anti-vibration base (DVIA-T45, Daeil Systems) and enclosing it in an acoustic box (Schaefer, Italy).

Mechanical measurements, aimed to characterise the Young's modulus of elasticity of the ECM were performed by recording force versus distance curves (shortly force curves, FCs), then transformed into force vs indentation curves, as described in Refs [13,54,55]. We used custom colloidal probes, produced by attaching borosilicate glass spheres to tipless cantilevers (MikroMasch HQ:CSC38/Tipless/No Al or NanoandMore TL-FM), as described in Ref. [56]. The tip radius was calibrated by means of reverse AFM imaging [56]. The cantilever spring constant was calibrated using the thermal noise method [57,58], and fine corrections were applied to account for geometrical and dimensional issues [59,60]. The deflection sensitivity (or inverse optical lever sensitivity, invOLS) of the optical beam deflection apparatus was measured as the inverse of the slope of the deflection vs z-piezo displacement curves acquired on a stiff substrate [55]. The deflection sensitivity was monitored and if necessary corrected during AFM experiments using the contactless SNAP method [61], assuming as reference spring constant the intrinsic spring constant previously calibrated.

The probes used had spring constants of 3-4 N/m, radii of 5.5 and 9 μm. 10 sets of force-distance curves (force volumes, FVs), consisting of 20x20 curves each, spanning typically an area of 50μm x 50μm, were acquired on regions separated by more than 200 μm on each slice. All measurements were carried out in a droplet of PBS, confined on the glass slide by means of hydrophobic ink (Sigma).

The precise alignment of AFM and optical images was possible thanks to the Bruker MIRO software, which allowed to choose the ROIs on the ECMs for the analysis (as during the force spectroscopy experiments). The transparency of the slices with thickness below 50 μm allowed us to identify and select regions where pieces of ECM

had been cut by LMD. The ECM probe can be placed precisely on top of a cell using the optical alignment, ensuring that contact is established with the ECM, and not with another part of the cantilever.

Adhesion Force Spectroscopy measurements were performed according to the protocol described in Refs [11,25], by acquiring several FCs per cell on at least 4 cells per each contact time, using the ECM probes. In force spectroscopy experiments, the adhesion pattern in the retracting portion of the FC is studied; upon contact with the sample, the tip was retracted after a contact time (ct) of 0, 20, 60 and 120s, during which the z-sensor position was kept constant by the feedback of the AFM. A typical retraction portion of a FC is shown in Figure S8, where the adhesive features (jumps and tethers) can be clearly observed. We typically used the following values for the ramp parameters: ramp frequency, 1 Hz; ramp size, 10 μm; maximum force, 1nN.

For the control (inhibition) experiment, the 4b4 antibody, an inhibitor of β1 integrin, was added to the medium, at a concentration of 5 μg/mL, 20 minutes before the AFM measurement. Experiments were carried out at 37°C using a thermostatic fluid cell and a temperature controller (Lakeshore 331, Ohio, USA).

Functionalisation of tipless cantilever. The tipless cantilevers were cleaned in an oxygen plasma chamber at a power of 80W for two minutes prior to the functionalisation, to remove organic contaminants and maximise the number of surface -OH groups. The vapor APTES deposition was performed under static nitrogen for three minutes in a desiccator with 50μl of APTES (Sigma). Cantilevers are then washed in toluene to remove any unbound APTES and left in an oven for the curing of the functionalisation [62,63]. The successful functionalisation of the cantilevers with APTES was checked by wettability measurements on an equivalent silicon substrate (with native oxide layer on top), before and after APTES deposition (Figure S9). This substrate has the same surface chemistry of AFM cantilevers. Deposition of APTES typically makes a hydrophilic surface more hydrophobic, as revealed by the marked increase of the contact angle in Figure S9. On APTES functionalised cantilevers, we deposited a droplet of genipin for 20 min to allow covalent reaction both with APTES and future ECM [64,65]. Afterwards, the cantilevers were gently washed with PBS and directly used for assembling with the ECM pieces. The obtained probes can be reused many times; indeed, the removal of the functionalisation can be done by piranha cleaning, as discussed in Supporting Note SN1[66].

Production of native ECM probes. The laser microdissected pieces of ECM (Figure S2 and S6) were attached to functionalised tipless cantilevers (MikroMasch HQ:CSC38/Tipless/No Al). Attachment of ECM pieces to tipless cantilevers, rather than to cantilevers with tip, was found to be more reliable. The procedure for the detachment of ECM pieces from the glass slide and the attachment to the tipless cantilever is described in detail in the Results section. For force spectroscopy experiments, the spring constant of the cantilevers was chosen in the range 0.01-0.05 N/m.

Data analysis. Processing of the data was carried out using custom routines written in Matlab (Mathworks) language. The raw FCs, consisting of the raw deflection signal from the photodetector (in Volts) units as a function of the z-piezo displacement (in nm), have been rescaled using the measured calibration factors (deflection sensitivity and spring constant) into force (in nN) vs indentation or tip-sample distance (in nm), according to the standard procedure [55].

The elastic properties of cells and ECMs were characterised through their Young's modulus (YM) of elasticity, extracted by fitting the Hertz model to the 20%-80% indentation range of the FCs (details in Refs [13,54]),

$$F = \frac{4}{3}\frac{E}{1-\nu^2}R^{\frac{1}{2}}\delta^{\frac{3}{2}} \qquad (1)$$

, which is accurate as long as the indentation δ is small compared to the radius R. In Eq. (1), ν is the Poisson's coefficient, which is typically assumed to be equal to 0.5 for in-compressible materials, and E is the YM.

Finite thickness correction for cells was applied as described in Refs [54,67,68]. In the case of ECM, despite the relatively small thickness of the slices, this correction was not applied because the thickness is not known with good accuracy, being the underlying substrate not always accessible; nevertheless, despite a systematic overestimation of the YM of the ECM, we were able to carry out a comparative characterisation of ECM elasticity in different conditions.

For the analysis of adhesion force spectroscopy data, a custom MATLAB routine was used to detect specific adhesion events in the FCs (jumps and tethers [22,25]) and to calculate the values of the relevant parameters (see Figure S8), as described in Chighizola et. al. [25,69], like the mean number of jumps and tethers per force curve, N_j and N_t, respectively, the total number of events $N_{tot}=N_j+N_t$, and the mean total

adhesion force F_a, all these quantities being averaged across all FCs for a given condition; the mean force per jump $<F_j>$ and the mean force per tether $<F_t>$ represent the mean values from the distribution of F_j and F_t values measured in a specific condition. The associated errors were calculated by summing in quadrature the standard deviation of the mean to an instrumental error of 3%, calculated by propagating the calibration uncertainties in the fitting procedure through a Monte Carlo simulation[54].

Immunofluorescence

10µm thick snap-frozen OCT-embedded cryosections were mounted on positively charged glass slide (Superfrost plus adhesion slide, #J1800AMNZ, Epredia Inc) and processed as described above for laser microdissection. Engraved and non-engraved sections were fixed in 4% Paraformaldehyde (#15710 EM grade, Electron Microscopy Sciences) at room temperature for 10 min. After washing in PBS, sections were incubated for 1 hour with blocking buffer (2% Donkey serum, 1.5% BSA, 0.25% Fish Gelatin, PBS pH=7.2) and then incubated overnight at 4˚C with the following primary antibodies: anti-Laminin β1 (4µg/ml, sc-17810, Santa Cruz Biotech), anti-Fibronectin (10 µg/ml, NBP1-91258SS, NovusBio), anti-Collagen IV (20 µg/ml, AB769, Millipore).

After washing, anti-goat Alexa Fluor® 488, anti-mouse Alexa Fluor® 647 and anti-rabbit Alexa Fluor 555 conjugated fluorophore-labeled F(ab)2 donkey secondary antibodies were used (Jackson Immunoresearch). Sections were DAPI counterstained and 3x3 Z-stacked large images (9 mm depth, 11 stacks) were acquired using a Yokogawa Spinning Disk Field Scanning Confocal System (CSU-W1, Nikon Europe BV, Amsterdam, Netherlands) equipped with 405, 488, 561, 640, 785 nm lines of solid-state lasers, 40x/1.15NA water immersion objective lens and a Prime BSI sCMOS camera (Teledyne Photometrics, Tucson, AZ).

Mean fluorescent intensity signal was quantified in multiple ROIs (175 um2 each; n=10, 5 ROIs per each field, 2 field acquired per each layer) and normalised to the respective average pixel intensity of the entire stained area. Data represent the normalised signal intensity compared to the average value of the submucosal layer for each matrix. For pre- and post-cut evaluation, fluorescent signal intensity was quantified in the central portion of the engraved region (Post-LMD) and the

corresponding area on a consecutive section not subjected to laser cut (Pre-LMD). The normalised signal intensity was averaged for each ECM and scaled between 0 and 1 (n=30, 5 ROIs per each field, 6 fields acquired distributed along the layers of the bladder). Mann-Whitney test was used to compare differences in the signal intensity.

Author contributions

Conceptualisation: AP, CS;
methodology – ECM preparation: IL;
methodology – probe fabrication and characterisation: HH, GRD, AP;
methodology – laser microdissection and staining: LN, PDC, GRD;
methodology – cell culture and preparation: HH, CS;
methodology – AFM and force spectroscopy: HH, MC, AP;
data curation and analysis: HH, MC, GRD, PDC, AP;
original draft writing and editing: HH, MC, AP;
draft revision: all authors;
supervision: MC, GRD, CS, AP;
resources, funding, and project administration: AP, GRD, MA.

Author contributions were allocated adopting the terminology of CRediT Contributor Roles Taxonomy.

Conflicts of interest

There are no conflicts to declare.

Acknowledgements

This research was funded by the European Union's Horizon 2020 research and innovation program under the Marie Skłodowska-Curie Action grant agreement No. 812772, project Phys2Biomed, and under FET Open grant agreement No. 801126, project EDIT.
PDC is supported by an AIRC fellowship.

References

(1) Alberts, Bruce. *Essential Cell Biology*, 2nd ed.; Garland Science Pub.: New York NY, 1998; Vol. 51. https://doi.org/10.1002/(sici)1098-2795(199812)51:4<477::aid-mrd17>3.0.co;2-w.

(2) Frantz, C.; Stewart, K. M.; Weaver, V. M. The Extracellular Matrix at a Glance. *J Cell Sci* **2010**, *123* (24), 4195–4200. https://doi.org/10.1242/jcs.023820.

(3) Theocharis, A. D.; Skandalis, S. S.; Gialeli, C.; Karamanos, N. K. Extracellular Matrix Structure. *Adv Drug Deliv Rev* **2016**, *97*, 4–27. https://doi.org/10.1016/j.addr.2015.11.001.

(4) Cox, T. R. The Matrix in Cancer. *Nat Rev Cancer* **2021**, *21* (4), 217–238. https://doi.org/10.1038/s41568-020-00329-7.

(5) Gauthier, N. C.; Roca-Cusachs, P. Mechanosensing at Integrin-Mediated Cell–Matrix Adhesions: From Molecular to Integrated Mechanisms. *Curr Opin Cell Biol* **2018**, *50*, 20–26. https://doi.org/10.1016/j.ceb.2017.12.014.

(6) Alcaraz, J.; Otero, J.; Jorba, I.; Navajas, D. Bidirectional Mechanobiology between Cells and Their Local Extracellular Matrix Probed by Atomic Force Microscopy. *Semin Cell Dev Biol* **2018**, *73*, 71–81. https://doi.org/10.1016/j.semcdb.2017.07.020.

(7) Sun, Z.; Guo, S. S.; Fässler, R. Integrin-Mediated Mechanotransduction. *Journal of Cell Biology* **2016**, *215* (4), 445–456. https://doi.org/10.1083/jcb.201609037.

(8) Jaalouk, D. E.; Lammerding, J. Mechanotransduction Gone Awry. *Nat Rev Mol Cell Biol* **2009**, *10* (1), 63–73. https://doi.org/10.1038/nrm2597.

(9) Chighizola, M.; Dini, T.; Lenardi, C.; Milani, P.; Podestà, A.; Schulte, C. Mechanotransduction in Neuronal Cell Development and Functioning. *Biophysical Reviews*. 2019, pp 701–720. https://doi.org/10.1007/s12551-019-00587-2.

(10) Lansky, Z.; Mutsafi, Y.; Houben, L.; Ilani, T.; Armony, G.; Wolf, S. G.; Fass, D. 3D Mapping of Native Extracellular Matrix Reveals Cellular Responses to the Microenvironment. *J Struct Biol X* **2019**, *1*, 100002. https://doi.org/10.1016/j.yjsbx.2018.100002.

(11) Chighizola, M.; Dini, T.; Marcotti, S.; D'Urso, M.; Piazzoni, C.; Borghi, F.; Previdi, A.; Ceriani, L.; Folliero, C.; Stramer, B.; Lenardi, C.; Milani, P.; Podestà, A.; Schulte, C. The Glycocalyx Affects the Mechanotransductive Perception of the Topographical Microenvironment. *J Nanobiotechnology* **2022**, *20* (1), 418. https://doi.org/10.1186/s12951-022-01585-5.

(12) Martinez-Vidal, L.; Murdica, V.; Venegoni, C.; Pederzoli, F.; Bandini, M.; Necchi, A.; Salonia, A.; Alfano, M. Causal Contributors to Tissue Stiffness and Clinical Relevance in Urology. *Commun Biol* **2021**, *4* (1), 1–16. https://doi.org/10.1038/s42003-021-02539-7.

(13) Holuigue, H.; Lorenc, E.; Chighizola, M.; Schulte, C.; Varinelli, L.; Deraco, M.; Guaglio, M.; Gariboldi, M.; Podestà, A. Force Sensing on Cells and Tissues by Atomic Force Microscopy. *Sensors* **2022**, *22* (6), 2197. https://doi.org/10.3390/s22062197.

(14) Krieg, M.; Fläschner, G.; Alsteens, D.; Gaub, B. M.; Roos, W. H.; Wuite, G. J. L.; Gaub, H. E.; Gerber, C.; Dufrêne, Y. F.; Müller, D. J. Atomic Force Microscopy-Based Mechanobiology. *Nature Reviews Physics* **2019**, *1* (1), 41–57. https://doi.org/10.1038/s42254-018-0001-7.

(15) Omidvar, R.; Tafazzoli-shadpour, M.; Shokrgozar, M. A.; Rostami, M. Atomic Force Microscope-Based Single Cell Force Spectroscopy of Breast Cancer Cell

Lines: An Approach for Evaluating Cellular Invasion. *J Biomech* **2014**, *47* (13), 3373–3379. https://doi.org/10.1016/j.jbiomech.2014.08.002.
(16) Alessandrini, A.; Facci, P. AFM: A Versatile Tool in Biophysics. *Meas Sci Technol* **2005**, *16* (6), 65–92. https://doi.org/10.1088/0957-0233/16/6/R01.
(17) Martinez-Vidal, L.; Chighizola, M.; Berardi, M.; Alchera, E.; Locatelli, I.; Pederzoli, F.; Venegoni, C.; Lucianò, R.; Milani, P.; Bielawski, K.; Salonia, A.; Podestà, A.; Alfano, M. Micro-Mechanical Fingerprints of the Rat Bladder Change in Actinic Cystitis and Tumor Presence. *Commun Biol* **2023**, *6* (1), 217. https://doi.org/10.1038/s42003-023-04572-0.
(18) Müller, D. J.; Dumitru, A. C.; lo Giudice, C.; Gaub, H. E.; Hinterdorfer, P.; Hummer, G.; de Yoreo, J. J.; Dufrêne, Y. F.; Alsteens, D. Atomic Force Microscopy-Based Force Spectroscopy and Multiparametric Imaging of Biomolecular and Cellular Systems. *Chem Rev* **2021**, *121* (19), 11701–11725. https://doi.org/10.1021/acs.chemrev.0c00617.
(19) Friedrichs, J.; Helenius, J.; Muller, D. J. Quantifying Cellular Adhesion to Extracellular Matrix Components by Single-Cell Force Spectroscopy. *Nat Protoc* **2010**, *5* (7), 1353–1361. https://doi.org/10.1038/nprot.2010.89.
(20) Strohmeyer, N.; Bharadwaj, M.; Costell, M.; Fässler, R.; Müller, D. J. Fibronectin-Bound A5β1 Integrins Sense Load and Signal to Reinforce Adhesion in Less than a Second. *Nat Mater* **2017**, *16* (12), 1262–1270. https://doi.org/10.1038/nmat5023.
(21) Yu, M.; Wang, J.; Muller, D. J.; Helenius, J. In PC3 Prostate Cancer Cells Ephrin Receptors Crosstalk to B1-Integrins to Strengthen Adhesion to Collagen Type i. *Sci Rep* **2015**, *5* (1), 8206. https://doi.org/10.1038/srep08206.
(22) Friedrichs, J.; Legate, K. R.; Schubert, R.; Bharadwaj, M.; Werner, C.; Müller, D. J.; Benoit, M. A Practical Guide to Quantify Cell Adhesion Using Single-Cell Force Spectroscopy. *Methods* **2013**, *60* (2), 169–178. https://doi.org/10.1016/j.ymeth.2013.01.006.
(23) Maynard, S. A.; Gelmi, A.; Skaalure, S. C.; Pence, I. J.; Lee-Reeves, C.; Sero, J. E.; Whittaker, T. E.; Stevens, M. M. Nanoscale Molecular Quantification of Stem Cell-Hydrogel Interactions. *ACS Nano* **2020**, *14* (12), 17321–17332. https://doi.org/10.1021/acsnano.0c07428.
(24) Jiang, L.; Sun, Z.; Chen, X.; Li, J.; Xu, Y.; Zu, Y.; Hu, J.; Han, D.; Yang, C. Cells Sensing Mechanical Cues: Stiffness Influences the Lifetime of Cell-Extracellular Matrix Interactions by Affecting the Loading Rate. *ACS Nano* **2016**, *10* (1), 207–217. https://doi.org/10.1021/acsnano.5b03157.
(25) Chighizola, M.; Previdi, A.; Dini, T.; Piazzoni, C.; Lenardi, C.; Milani, P.; Schulte, C.; Podestà, A. Adhesion Force Spectroscopy with Nanostructured Colloidal Probes Reveals Nanotopography-Dependent Early Mechanotransductive Interactions at the Cell Membrane Level. *Nanoscale* **2020**, *12* (27), 14708–14723. https://doi.org/10.1039/d0nr01991g.
(26) Sun, Z.; Martinez-Lemus, L. A.; Hill, M. A.; Meininger, G. A. Extracellular Matrix-Specific Focal Adhesions in Vascular Smooth Muscle Produce Mechanically Active Adhesion Sites. *Am J Physiol Cell Physiol* **2008**, *295* (1), C268–C278. https://doi.org/10.1152/ajpcell.00516.2007.
(27) Harjumäki, R.; Zhang, X.; Nugroho, R. W. N.; Farooq, M.; Lou, Y.-R.; Yliperttula, M.; Valle-Delgado, J. J.; Österberg, M. AFM Force Spectroscopy Reveals the Role of Integrins and Their Activation in Cell–Biomaterial Interactions. *ACS Appl Bio Mater* **2020**, *3* (3), 1406–1417. https://doi.org/10.1021/acsabm.9b01073.
(28) Li, Z.; Liu, T.; Yang, J.; Lin, J.; Xin, S. X. Characterization of Adhesion Properties of the Cardiomyocyte Integrins and Extracellular Matrix Proteins Using Atomic

Force Microscopy. *Journal of Molecular Recognition* **2020**, *33* (4). https://doi.org/10.1002/jmr.2823.
(29) Chièze, L.; le Cigne, A.; Meunier, M.; Berquand, A.; Dedieu, S.; Devy, J.; Molinari, M. Quantitative Characterization of Single-Cell Adhesion Properties by Atomic Force Microscopy Using Protein-Functionalized Microbeads. *Journal of Molecular Recognition* **2019**, *32* (3), e2767. https://doi.org/10.1002/jmr.2767.
(30) Helenius, J.; Heisenberg, C. P.; Gaub, H. E.; Muller, D. J. Single-Cell Force Spectroscopy. *J Cell Sci* **2008**, *121* (11), 1785–1791. https://doi.org/10.1242/jcs.030999.
(31) Viji Babu, P. K.; Mirastschijski, U.; Belge, G.; Radmacher, M. Homophilic and Heterophilic Cadherin Bond Rupture Forces in Homo- or Hetero-Cellular Systems Measured by AFM-Based Single-Cell Force Spectroscopy. *European Biophysics Journal* **2021**, *1*, 3. https://doi.org/10.1007/s00249-021-01536-2.
(32) Takada, Y.; Ye, X.; Simon, S. The Integrins. *Genome Biol* **2007**, *8* (5), 215. https://doi.org/10.1186/gb-2007-8-5-215.
(33) Orré, T.; Rossier, O.; Giannone, G. The Inner Life of Integrin Adhesion Sites: From Single Molecules to Functional Macromolecular Complexes. *Exp Cell Res* **2019**, *379* (2), 235–244. https://doi.org/10.1016/j.yexcr.2019.03.036.
(34) Humphries, J. D.; Chastney, M. R.; Askari, J. A.; Humphries, M. J. Signal Transduction via Integrin Adhesion Complexes. *Curr Opin Cell Biol* **2019**, *56*, 14–21. https://doi.org/10.1016/j.ceb.2018.08.004.
(35) Changede, R.; Sheetz, M. Integrin and Cadherin Clusters: A Robust Way to Organize Adhesions for Cell Mechanics. *BioEssays* **2017**, *39* (1), e201600123. https://doi.org/10.1002/bies.201600123.
(36) Campbell, I. D.; Humphries, M. J. Integrin Structure, Activation, and Interactions. *Cold Spring Harb Perspect Biol* **2011**, *3* (3), a004994–a004994. https://doi.org/10.1101/cshperspect.a004994.
(37) Nugroho, R. W. N.; Harjumäki, R.; Zhang, X.; Lou, Y.-R.; Yliperttula, M.; Valle-Delgado, J. J.; Österberg, M. Quantifying the Interactions between Biomimetic Biomaterials – Collagen I, Collagen IV, Laminin 521 and Cellulose Nanofibrils – by Colloidal Probe Microscopy. *Colloids Surf B Biointerfaces* **2019**, *173*, 571–580. https://doi.org/10.1016/j.colsurfb.2018.09.073.
(38) Datta, S.; Malhotra, L.; Dickerson, R.; Chaffee, S.; Sen, C. K.; Roy, S. Laser Capture Microdissection: Big Data from Small Samples. *Histology and Histopathology*. 2015. https://doi.org/10.14670/HH-11-622.
(39) Bevilacqua, C.; Ducos, B. Laser Microdissection: A Powerful Tool for Genomics at Cell Level. *Mol Aspects Med* **2018**, *59*, 5–27. https://doi.org/10.1016/j.mam.2017.09.003.
(40) Ajalloueian, F.; Lemon, G.; Hilborn, J.; Chronakis, I. S.; Fossum, M. Bladder Biomechanics and the Use of Scaffolds for Regenerative Medicine in the Urinary Bladder. *Nat Rev Urol* **2018**, *15* (3), 155–174. https://doi.org/10.1038/nrurol.2018.5.
(41) Orabi, H.; Bouhout, S.; Morissette, A.; Rousseau, A.; Chabaud, S.; Bolduc, S. Tissue Engineering of Urinary Bladder and Urethra: Advances from Bench to Patients. *The Scientific World Journal* **2013**, *2013*, 1–13. https://doi.org/10.1155/2013/154564.
(42) Mortensen, L. J.; Alt, C.; Turcotte, R.; Masek, M.; Liu, T.-M.; Côté, D. C.; Xu, C.; Intini, G.; Lin, C. P. Femtosecond Laser Bone Ablation with a High Repetition Rate Fiber Laser Source. *Biomed Opt Express* **2015**, *6* (1), 32. https://doi.org/10.1364/BOE.6.000032.

(43) Gudzenko, T.; Franz, C. M. Controlling Fibronectin Fibrillogenesis Using Visible Light. *Front Mol Biosci* **2020**, *7*. https://doi.org/10.3389/fmolb.2020.00149.
(44) Zuiverloon, T. C. M.; de Jong, F. C.; Costello, J. C.; Theodorescu, D. Systematic Review: Characteristics and Preclinical Uses of Bladder Cancer Cell Lines. *Bladder Cancer* **2018**, *4* (2), 169–183. https://doi.org/10.3233/BLC-180167.
(45) Taubenberger, A.; Cisneros, D. A.; Friedrichs, J.; Puech, P. H.; Muller, D. J.; Franz, C. M. Revealing Early Steps of A2β1 Integrin-Mediated Adhesion to Collagen Type I by Using Single-Cell Force Spectroscopy. *Mol Biol Cell* **2007**, *18* (5), 1634–1644. https://doi.org/10.1091/mbc.E06-09-0777.
(46) Janiszewska, M.; Primi, M. C.; Izard, T. Cell Adhesion in Cancer: Beyond the Migration of Single Cells. *Journal of Biological Chemistry* **2020**, *295* (8), 2495–2505. https://doi.org/10.1074/jbc.REV119.007759.
(47) Cavallaro, U.; Christofori, G. Cell Adhesion in Tumor Invasion and Metastasis: Loss of the Glue Is Not Enough. *Biochim Biophys Acta Rev Cancer* **2001**, *1552* (1), 39–45. https://doi.org/10.1016/S0304-419X(01)00038-5.
(48) Müller, D. J.; Helenius, J.; Alsteens, D.; Dufrne, Y. F. Force Probing Surfaces of Living Cells to Molecular Resolution. *Nature Chemical Biology*. Nature Publishing Group May 15, 2009, pp 383–390. https://doi.org/10.1038/nchembio.181.
(49) Evans, E. A.; Calderwood, D. A. Forces and Bond Dynamics in Cell Adhesion. *Science (1979)* **2007**, *316* (5828), 1148–1153. https://doi.org/10.1126/science.1137592.
(50) Mescola, A.; Vella, S.; Scotto, M.; Gavazzo, P.; Canale, C.; Diaspro, A.; Pagano, A.; Vassalli, M. Probing Cytoskeleton Organisation of Neuroblastoma Cells with Single-Cell Force Spectroscopy. *Journal of Molecular Recognition* **2012**, *25* (5), 270–277. https://doi.org/10.1002/jmr.2173.
(51) Alfred Yung, W. K. The Value of Cell Line Validation. *Neuro Oncol* **2012**, *14* (6), 675. https://doi.org/10.1093/neuonc/nos132.
(52) Genovese, L.; Zawada, L.; Tosoni, A.; Ferri, A.; Zerbi, P.; Allevi, R.; Nebuloni, M.; Alfano, M. Cellular Localization, Invasion, and Turnover Are Differently Influenced by Healthy and Tumor-Derived Extracellular Matrix. *Tissue Eng Part A* **2014**, *20* (13–14), 2005–2018. https://doi.org/10.1089/ten.tea.2013.0588.
(53) Alfano, M.; Nebuloni, M.; Allevi, R.; Zerbi, P.; Longhi, E.; Lucianò, R.; Locatelli, I.; Pecoraro, A.; Indrieri, M.; Speziali, C.; Doglioni, C.; Milani, P.; Montorsi, F.; Salonia, A. Linearized Texture of Three-Dimensional Extracellular Matrix Is Mandatory for Bladder Cancer Cell Invasion. *Sci Rep* **2016**, *6* (1), 36128. https://doi.org/10.1038/srep36128.
(54) Puricelli, L.; Galluzzi, M.; Schulte, C.; Podestà, A.; Milani, P. Nanomechanical and Topographical Imaging of Living Cells by Atomic Force Microscopy with Colloidal Probes. *Review of Scientific Instruments* **2015**, *86* (3), 33705. https://doi.org/10.1063/1.4915896.
(55) Butt, H. J.; Cappella, B.; Kappl, M. Force Measurements with the Atomic Force Microscope: Technique, Interpretation and Applications. *Surf Sci Rep* **2005**, *59* (1–6), 1–152. https://doi.org/10.1016/j.surfrep.2005.08.003.
(56) Indrieri, M.; Podestà, A.; Bongiorno, G.; Marchesi, D.; Milani, P. Adhesive-Free Colloidal Probes for Nanoscale Force Measurements: Production and Characterization. *Review of Scientific Instruments* **2011**, *82* (2), 023708. https://doi.org/10.1063/1.3553499.
(57) Hutter, J. L.; Bechhoefer, J. Calibration of Atomic-Force Microscope Tips. *Review of Scientific Instruments* **1993**, *64* (7), 1868–1873. https://doi.org/10.1063/1.1143970.

(58) Butt, H. J.; Jaschke, M. Calculation of Thermal Noise in Atomic Force Microscopy. *Nanotechnology* **1995**, *6* (1), 1–7. https://doi.org/10.1088/0957-4484/6/1/001.
(59) Chighizola, M.; Puricelli, L.; Bellon, L.; Podestà, A. Large Colloidal Probes for Atomic Force Microscopy: Fabrication and Calibration Issues. *Journal of Molecular Recognition* **2021**, *34* (1), e2879. https://doi.org/10.1002/jmr.2879.
(60) Laurent, J.; Steinberger, A.; Bellon, L. Functionalized AFM Probes for Force Spectroscopy: Eigenmode Shapes and Stiffness Calibration through Thermal Noise Measurements. *Nanotechnology* **2013**, *24* (22), 225504. https://doi.org/10.1088/0957-4484/24/22/225504.
(61) Schillers, H.; Rianna, C.; Schäpe, J.; Luque, T.; Doschke, H.; Wälte, M.; Uriarte, J. J.; Campillo, N.; Michanetzis, G. P. A.; Bobrowska, J.; Dumitru, A.; Herruzo, E. T.; Bovio, S.; Parot, P.; Galluzzi, M.; Podestà, A.; Puricelli, L.; Scheuring, S.; Missirlis, Y.; Garcia, R.; Odorico, M.; Teulon, J.-M.; Lafont, F.; Lekka, M.; Rico, F.; Rigato, A.; Pellequer, J.-L.; Oberleithner, H.; Navajas, D.; Radmacher, M. Standardized Nanomechanical Atomic Force Microscopy Procedure (SNAP) for Measuring Soft and Biological Samples. *Sci Rep* **2017**, *7* (1), 5117. https://doi.org/10.1038/s41598-017-05383-0.
(62) Acres, R. G.; Ellis, A. v.; Alvino, J.; Lenahan, C. E.; Khodakov, D. A.; Metha, G. F.; Andersson, G. G. Molecular Structure of 3-Aminopropyltriethoxysilane Layers Formed on Silanol-Terminated Silicon Surfaces. *Journal of Physical Chemistry C* **2012**, *116* (10), 6289–6297. https://doi.org/10.1021/jp212056s.
(63) Fiorilli, S.; Rivolo, P.; Descrovi, E.; Ricciardi, C.; Pasquardini, L.; Lunelli, L.; Vanzetti, L.; Pederzolli, C.; Onida, B.; Garrone, E. Vapor-Phase Self-Assembled Monolayers of Aminosilane on Plasma-Activated Silicon Substrates. *J Colloid Interface Sci* **2008**, *321* (1), 235–241. https://doi.org/10.1016/j.jcis.2007.12.041.
(64) Jorba, I.; Beltrán, G.; Falcones, B.; Suki, B.; Farré, R.; García-Aznar, J. M.; Navajas, D. Nonlinear Elasticity of the Lung Extracellular Microenvironment Is Regulated by Macroscale Tissue Strain. *Acta Biomater* **2019**, *92*, 265–276. https://doi.org/10.1016/j.actbio.2019.05.023.
(65) Genchi, G. G.; Ciofani, G.; Liakos, I.; Ricotti, L.; Ceseracciu, L.; Athanassiou, A.; Mazzolai, B.; Menciassi, A.; Mattoli, V. Bio/Non-Bio Interfaces: A Straightforward Method for Obtaining Long Term PDMS/Muscle Cell Biohybrid Constructs. *Colloids Surf B Biointerfaces* **2013**, *105*, 144–151. https://doi.org/10.1016/j.colsurfb.2012.12.035.
(66) Reinhardt, K. *Handbook of Silicon Wafer Technology*, 3rd ed.; 2018.
(67) Garcia, P. D.; Garcia, R. Determination of the Elastic Moduli of a Single Cell Cultured on a Rigid Support by Force Microscopy. *Biophys J* **2018**, *114* (12), 2923–2932. https://doi.org/10.1016/j.bpj.2018.05.012.
(68) Dimitriadis, E. K.; Horkay, F.; Maresca, J.; Kachar, B.; Chadwick, R. S. Determination of Elastic Moduli of Thin Layers of Soft Material Using the Atomic Force Microscope. *Biophys J* **2002**, *82* (5), 2798–2810. https://doi.org/10.1016/S0006-3495(02)75620-8.
(69) Chighizola, M.; Dini, T.; Marcotti, S.; D'Urso, M.; Piazzoni, C.; Borghi, F.; Previdi, A.; Ceriani, L.; Folliero, C.; Stramer, B.; Lenardi, C.; Milani, P.; Podestà, A.; Schulte, C. The Glycocalyx Affects the Mechanotransductive Perception of the Topographical Microenvironment. *J Nanobiotechnology* **2022**, *20* (1), 418. https://doi.org/10.1186/s12951-022-01585-5.

Native extracellular matrix probes to target patient- and tissue- specific cell-microenvironment interactions by force spectroscopy

H. Holuigue[1], L. Nacci[2], P. Di Chiaro[2], M. Chighizola[1], I. Locatelli[3], C. Schulte[1], M. Alfano[3*], G.R. Diaferia[2,*], A. Podestà[1,*]

[1] CIMAINA and Dipartimento di Fisica "Aldo Pontremoli", Università degli Studi di Milano, via Celoria 16, 20133 Milano, Italy.
[2] Department of Experimental Oncology, IEO, European Institute of Oncology IRCCS, Milano, Italy.
[3] Division of Experimental Oncology/Unit of Urology, URI, IRCCS San Raffaele Hospital, Milan, Italy.
*Corresponding authors: alessandro.podesta@mi.infn.it, alfano.massimo@hsr.it, giuseppe.diaferia@ieo.it

Supporting Information

Contents

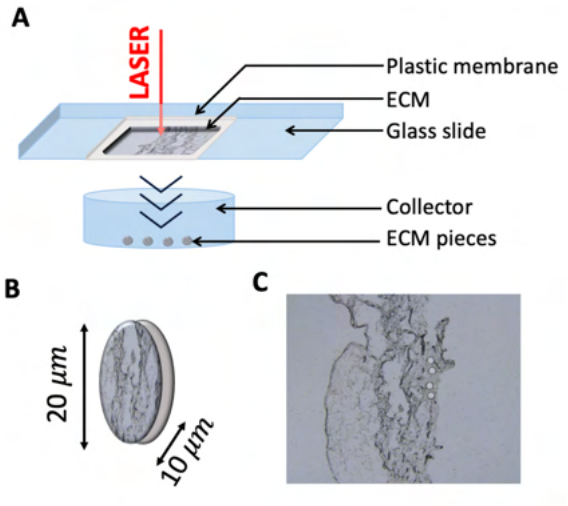

Figure S1. Schematics of the conventional use of the LMD system. (A) ECM fragments are cut by the UV laser together with the underlying plastic membrane and collected in a suitable reservoir where they fall by gravity. (B) The resulting circular pieces are 20 µm in diameter and 10µm thick, excluding the plastic membrane. (C) Upon cutting and collecting the pieces, circular holes are left in the ECM slice.

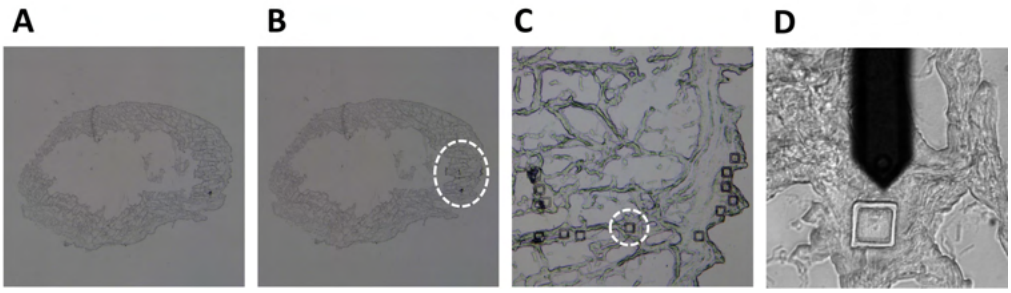

Figure S2. Optical images of the ECM rat bladder. (A) Before LMD cut, after PBS wash and ethanol dehydration. (B) After the LMD cut; the region of the cut is indicated. (C,D) Magnification of the cut region. The AFM cantilever is visible in D.

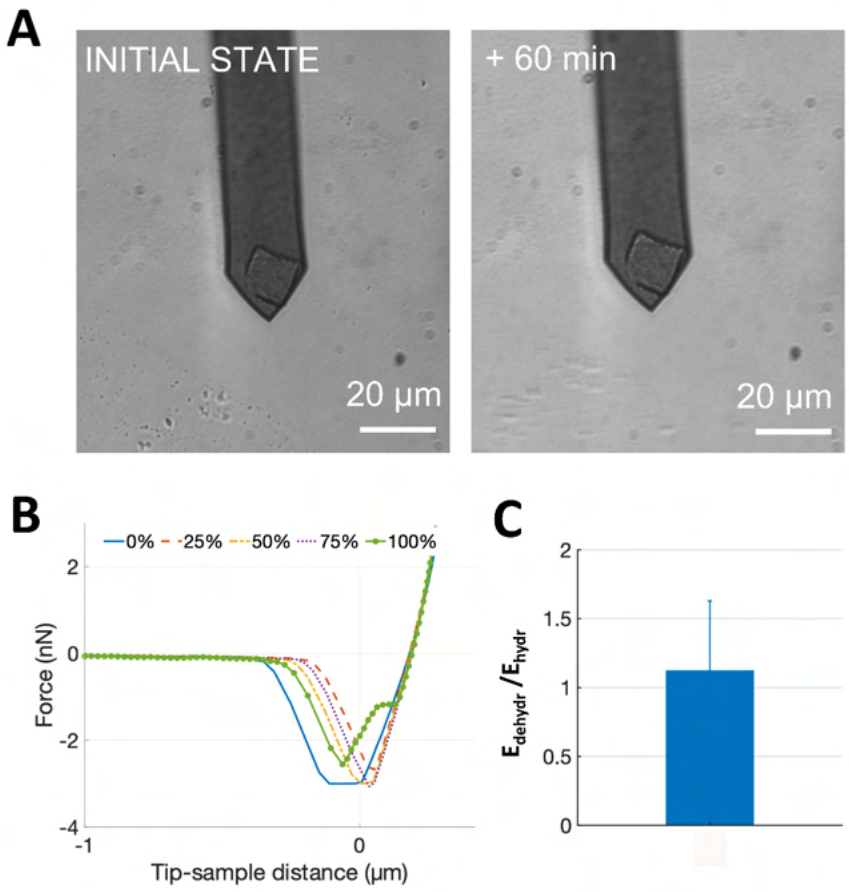

Figure S3. Stress tests on the ECM probes. (A) Optical images of an ECM probe before and after continuous scanning across a 20µm x 20µm area in Contact Mode for 60 minutes on a glass surface with a scan frequency of 1Hz. (B) Representative retraction curves acquired using an ECM probe ramped against a glass substrate before (0%), during (25, 50 and 75%), and at the end (100%) of an adhesion force spectroscopy experiment consisting in the acquisition of a total of 400 FCs. (C) The ratio E_{dehydr}/E_{hydr} of Young's modulus values E of an ECM sample before and after dehydration with 70% EtOH (the error bar represents the error calculated as the propagation of the effective standard deviations of the mean of E_{hydr} and E_{dehydr}).

Stress tests were performed to assess the firm attachment of the matrix to the cantilever and the force spectroscopy functionality after repeated use.

Firstly, we perform continuous scanning of a 20µm x 20µm square on glass at a frequency of 1Hz with the probe for more than 60 minutes and observed no appreciable displacement or damage (Figure S3A). Then, we carried out force spectroscopy in liquid on a glass surface, with 10s contact time, by recording 400FCs at 1Hz with 5nN applied force. Looking at representative FCs at the beginning (0%), during (25, 50 and

75%) and at the end of the experiment (100%), we did not notice important changes in the measured total adhesion force (Figure S3B) (a slight decrease can be noted at the end of the test, while no significant differences is observable in the first 75% of the test). Interestingly, in this case, where the ECM is interacting with a glass surface instead of a cell, we did not detect unbinding events (jumps and tethers) in the FCs, which are typically associated to integrin-related specific adhesive interactions.

Furthermore, as LMD requires the dehydration of the matrix with a minimum of 70% Ethanol, we performed AFM nanoindentation measurements on the same ECM before and after dehydration with Ethanol. No significant difference in the Young's modulus of the ECM was observed (Figure S3C).

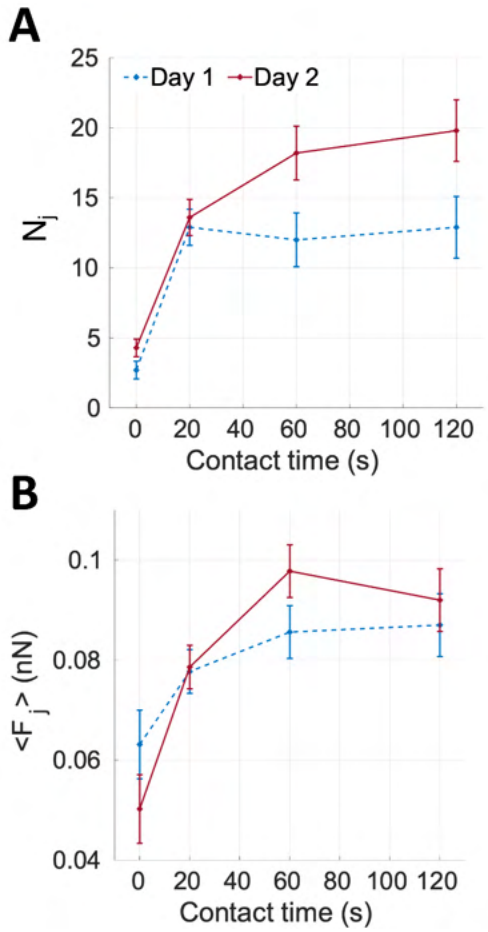

Figure S4. Mean number of jumps and force per jump measured on consecutive days (boxes A and B, respectively), during adhesion force spectroscopy experiments performed with the same ECM probe on AY-27 cells from the same passage: day 1 (in blue) and day 2 (in red). Different contact times (ct) have been used (ct = 0 s, 20 s, 60 s, 120 s).

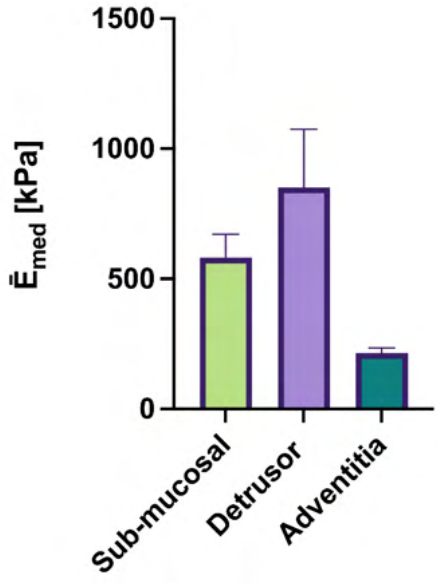

Figure S5. Young's modulus of the different ECM regions: sub-mucosal, detrusor and adventitia. The mean median values are reported; error bars represent standard deviations of the mean. Data have not been corrected for bottom effect and might therefore overestimate the true Young's modulus values. All measurements have been performed on the same 10µm decellularised ECM slice, on microdissected pieces (inside and outside taken as equivalent). Error bars represent the standard deviation of the mean.

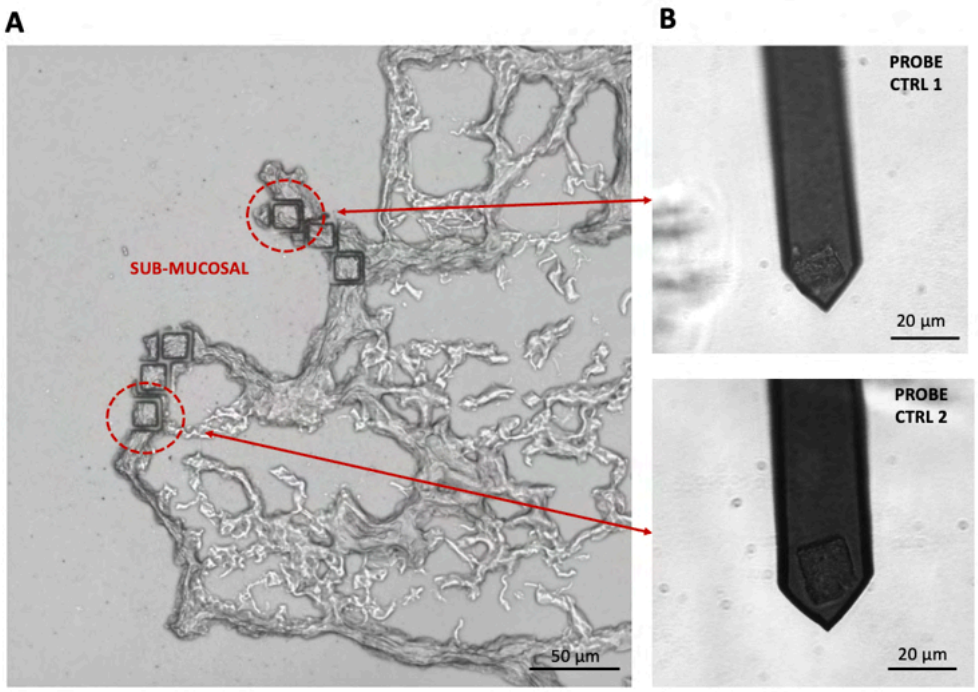

Figure S6. Optical image of the rat bladder ECM with the LMD cut. The red circles in (A) highlights the region in the submucosal layer where the ECM was cut to produce the control probes CTRL1 and CTRL2, shown in (B). The control probes were used in the integrin inhibitory experiments.

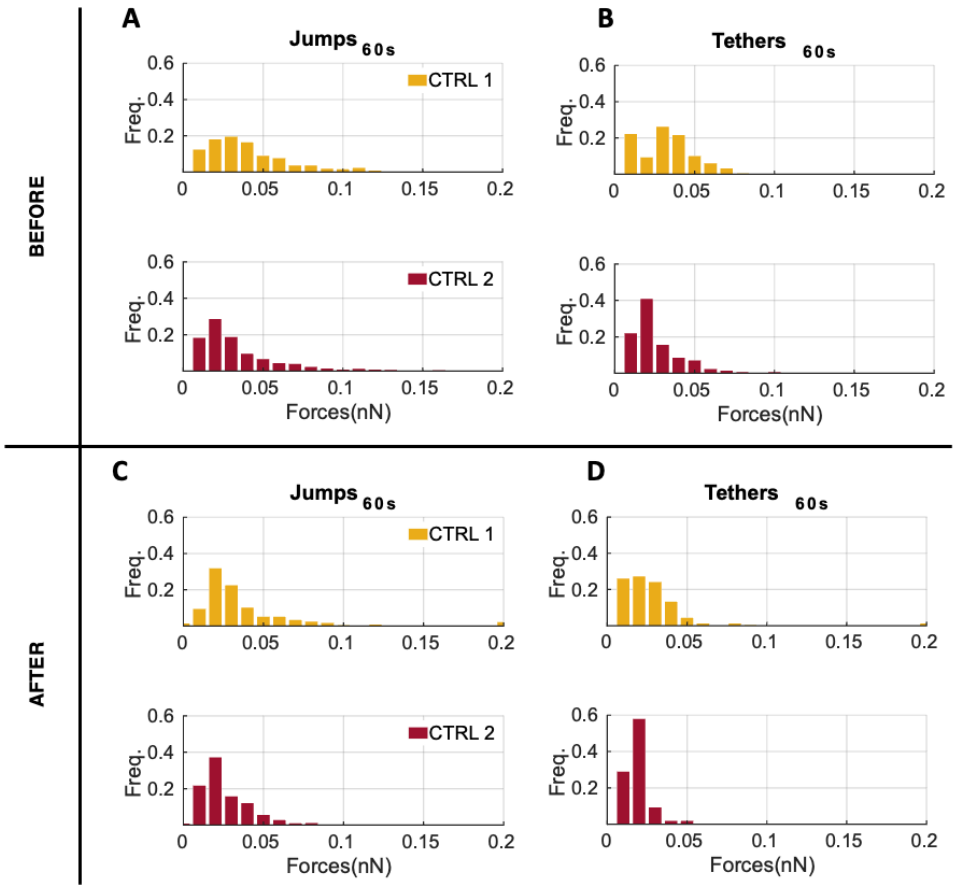

Figure S7. Distributions of jumps and tethers forces before and after the addition of the 4b4 integrin inhibitor antibody on AY-27 cells (boxes A-B and C-D, respectively), measured during control adhesion force spectroscopy experiments with ct= 60s performed with the CTRL1 and CTRL2 probes (see Figure S6).

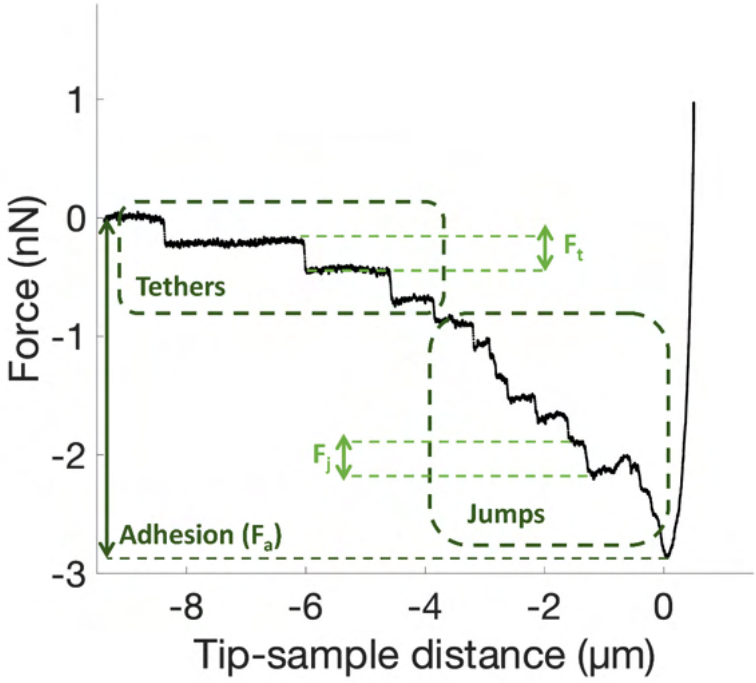

Figure S8. Representative force curve acquired during an adhesion force spectroscopy experiment using a native ECM probe. The relevant features and parameters are indicated: unbinding events (jumps and tethers), and the total adhesion force F_a. The forces F_j and F_t necessary to break a single integrin-ECM bond in jumps and tethers, respectively, are shown. From the distribution of jumps and tethers forces, the mean jumps and tethers forces $\langle F_j \rangle$ and $\langle F_t \rangle$, as well as the mean number of jump and tether events per force curves, N_j and N_t, and the total number of integrin-related events $N_{tot}=N_j+N_t$, are be calculated. The adhesion force F_a is calculated as the absolute difference between the minimum force value and the baseline value.

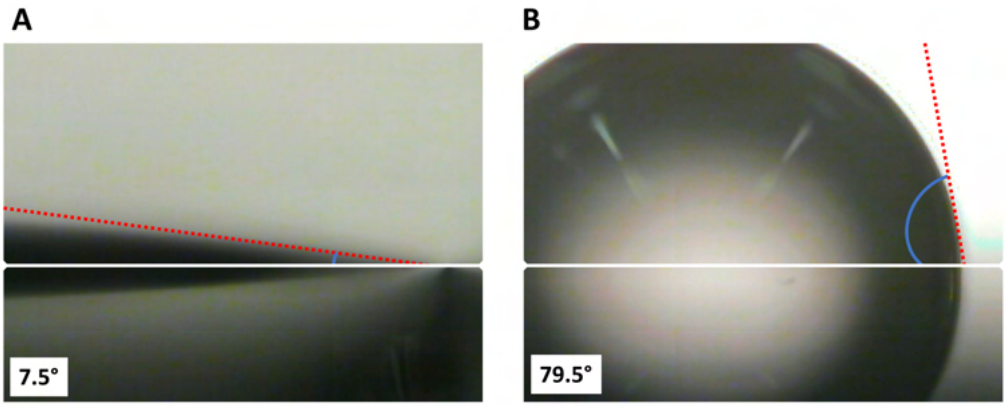

Figure S9. Contact angle analysis of water on functionalised silicon substrates, (A) before, and (B) after functionalisation with APTES. The contact angle increased from 7° to 79.5° upon APTES functionalisation of the oxidised silicon substrate.

Supporting Note SN1. Cleaning and re-use of the ECM probes

ECM probes can be cleaned and re-functionalised. In fact, the ECM can be degraded with proteolytic enzyme solutions such as helizyme, while the APTES coating (as well as the ECM) can be removed by piranha solution. Piranha solution is known to degrade any organic residues out of substrate such as silicon wafer and is commonly use in the AFM community for cleaning the probes.

Supporting Movies SM1, SM2, SM3. Attachment of ECM pieces to functionalised cantilevers

5.1. Conclusion and perspectives

Native ECM probes are likely to offer a different approach for cell-microenvironment interaction studies. Indeed, the possibility to select either the ECM region or/and the specific cell (including when both are taken by the same patient) makes this approach the most versatile and close to reproducing the original biological conditions in the field of adhesion force spectroscopy, so far. The developed protocol paves the way for applications to the study of cases of biological and clinical relevance in the context of cancer research and therapy, and beyond.

Even though the results presented in the chapter are interesting and demonstrate the capability of the probes to be used reliably, some further investigation should be carried out.

Firstly, some additional controls should be performed to identify more specifically the precise nature of the unbinding events. The distinction and fine mechanisms behind jumps and tethers, for example, are still an open issue within the community. A possibility of inhibiting specific subunits of integrins or collagen could help in the assignment of jumps events to cell-proteins interactions. In the last part of the paper, we targeted $\beta 1$ which is common for most of the collagen and laminin receptors [10,186] (**Figure 3**). By doing immunostaining on adjacent slices of the ECM (spatially separated by approximately 10 µm), we would be able to identify the principal components of the cut region for the ECM probe and propose a specialized control. For ECM probes mostly made from the detrusor region of the bladder, it might be more interesting to perform the control with α_V receptors. Similar approaches can be devised for probes produced from tissue specimens of other organs.

One could argue about the staining, even when performed on consecutive slices, could show some variation in protein composition within the original sample. In collaboration with IEO, we tried to perform an enzyme-linked immunosorbent assay (ELISA)[187] test directly on ECM pieces that have been previously attached to the cantilever. Considering that the area of single pieces was 400µm^2, the concentration of proteins was below the detection limit and did not allow us to obtain reliable data. Another approach could be the use of mass spectrometry tools to precisely identify and evaluate the quantity of proteins present in the ECM-probes[188,189].

Scanning electron microscopy (SEM) images and/or hi-resolution AFM imaging of the ECM before and after the laser microdissection treatment (including dehydration), but also at the edges of the cut, would further help confirm that the collagen fibers maintain their integrity during the process. SEM investigation of ECM probes could provide important information on the outcome of the probe production procedure, on one side, and on the other side could enrich the comprehension of the cell-ECM contact interface (effective contact area, nanotopographical details, etc.) during the force spectroscopy experiment.

Following the overall strategy outlined in this work, one possibility is to use the human bladder cancer cell models used in Chapter 2 in relation to human bladder ECM from the patients in different stages of the disease. Combining our methodology with complementary tools like immunostaining, SEM, ELISA, and mass spectrometry to precisely characterize the nature and evolution of the cell-ECM integrins interaction, may help us understand how bladder carcinoma has evolved throughout its stages from the perspective of the cells and the ECM. By analyzing specific patient cell-ECM interactions, one could have an idea of the next

potential target of the cancerous cells, leading to prevention and/or early diagnosis. This method could result in patient-oriented studies in the context of cancer prognosis.

6. General conclusions and perspectives

In this thesis the work carried out during my PhD project to study the cell-microenvironment interaction with AFM was presented. AFM was once again demonstrated to be an adjustable, resourceful, and most of all reliable technique for the quantitative investigation of nanoscale phenomena in biological systems. The study of the extracellular matrix but also cells' influence on cell, specifically in the context of cancer, is not trivial, and it was necessary to develop tools and methods to specifically target the players of cell-microenvironment communication. Interdisciplinarity and strong scientific collaboration has been proven to be a motor to scientific development.

The major results of the research work during my PhD are listed below.

- In Chapter 1, the critical points of the calibration of AFM probes have been considered. The available methods (LDV, Sader's, equipartition-based thermal noise method) are equivalent in principle, but require specific correction factors. Existing formulas, when available, are limited to the ideal rectangular geometry, while FEA calculations are necessary for handling the case (very frequently occurring) of non-ideal geometries; this is however still far from being routinary available in the laboratories, either via custom procedures or through the instrument software. Given the actual limitations, we provided our best calibration procedure for both tipless and CPs for applications to AFM studies of biological and other systems.
- In Chapter 2, we reported on the investigation, using custom CPs properly functionalized by ECM proteins, of the adhesion between cells and ECM in the context of urinary bladder carcinoma. We have measured distinct adhesion features with fibronectin and laminin in terms of maximum adhesion force and distribution of force, depending on the grade of invasiveness of the cells. More invasive cancer cell exhibits less adhesion and binding force with laminin, the major basal membrane protein, indicating the change in integrin interaction throughout cancer progression. Fibronectin binding was found to strengthen with time for the most invasive cell T24.
- We successfully produced native ECM probes using a combination of decellularization procedures and a novel Laser Microdissection approach, to faithfully reproduce, and not simply mimic, the structural and compositional complexity of the ECM (Chapter 3). We have opened a new path to perform personalized adhesion force spectroscopy experiments, where both the ECM and the cells can be selected to probe specific interactions and address specific biological and clinical questions. In fact, native ECM probes have a potential to contribute to develop novel quantitative approaches in the field of personalized medicine.
- A method to speed up nanomechanical measurements on cells and other systems has been developed, allowing for only partial mapping of the substrate (necessary for the evaluation of the local thickness of the sample). This results in a sparse set of FCs instead of a regular square or rectangular force volume; nevertheless, the total acquisition time is greatly reduced, which allows primarily to acquire more maps on different cells, to the benefit of statistics (Appendix A).
- Within the standardization activity of the Phys2BioMed project, a method has been developed to implement the bottom effect correction in nanoindentation experiments

in those cases where the local thickness of the cellular sample cannot be directly determined, such as with confluent cell layers, because the substrate (i.e., the bottom of the Petri dish) is not exposed (Appendix A). The method requires the determination of the mean layer thickness (i.e., by means of optical methods, such as confocal fluorescence microscopy, or by AFM, from the subset of topographic maps where the substrate is exposed). This method allows to accurately characterize the Young's modulus of elasticity of cells and other thin transparent systems and is particularly important when CPs are used, since the bottom effect in this case is typically amplified.

7. Appendix A

Improved measurement and data analysis procedures for faster and accurate nanomechanical investigation of cells: partial mapping and finite thickness correction

There is an interest in implementing robust methods for nanoindentation of cells, and this also includes data analysis procedures. AFM simultaneously provides the mechanical and topographical maps of the samples, allowing the user to implement point by point corrections that depends on the local thickness of the sample. An important example is provided by the bottom effect (or finite thickness) correction.

7.1. Development of the partial mapping method for the combined topographical and nanomechanical imaging

AFM can provide a topographic map as well as a stiffness map, for those map the better resolution, the more time consuming are the measurements. To have robust data, especially in the case of cells, that are heterogenous and complex system, it is necessary to have bigger statistics and measure the maximum of them. To that purpose, we developed two new methods to allow us to save time during the measurements, hence enhancing our statistics by measuring more cells.

As a reminder, the standard force mapping (or Force Volume) method [134,190,191]consisted in the acquisition of force curve on a defined grid of point, spanning the whole cell and its substrate. In this way the recording of both topographical maps, as well as elasticity maps was simultaneous and equivalent, allowing side by side comparison. The disadvantage of this method is the time of acquisition, in fact for a well resolved force volume map both in term of topography and Young's Modulus, it could take up to hours. During that time, cells could undergo changes in term of cytoskeleton and even initiation of mitosis, this could cause the need for repetition of the experiments on consecutive days inducing potential difference between the cells' population.

Our new method consists in the following steps:

- The acquisition of a limited number of FCs (minimum 10) on the rigid substrate around the cell, possibly in points symmetrically distributed around the cell, and the rest of the FCs acquired directly on the cells, at higher resolution, spanning the whole region of interest within the cell body. This requires the capability of the AFM software to

acquire an arbitrarily irregular set of FCs in precise locations, selected on an optical image of the sample that is accurately aligned with the AFM scan area.

- From the FCs recorded on the substrate, we reconstruct the local height z_s as the value of the z-sensor axis at the point of maximum force (a common deflection or force setpoint is set during the acquisition of the FCs)[134]. The substrate coordinates x_s, y_s and z_s coordinates are then obtained.

- A plane fit is performed to the image. To this purpose, using the x_s, y_s and z_s coordinates of the substrate, the parameters a, b, c, d defining the plane are obtained through a multilinear regression:

$$ax + by + cx + d = 0 \tag{31}$$

- For each of the points taken on the cells, with planar x_c, y_c coordinates, we evaluate the substrate height as follows:

$$z_{substrate} = -\frac{a}{c}x_c - \frac{b}{c}y_c - \frac{d}{c} \tag{32}$$

- Point by point reconstruction of the unperturbed (i.e., non-deformed, in the zero-force limit) cell's height h_{cell} is done by subtracting the local substrate height $z_{substrate}$ and adding back the local indentation δ, estimated in the process of the Hertzian fit (**Figure 34A**):

$$h_{cell} = z_c - z_{substrate} + \delta \tag{33}$$

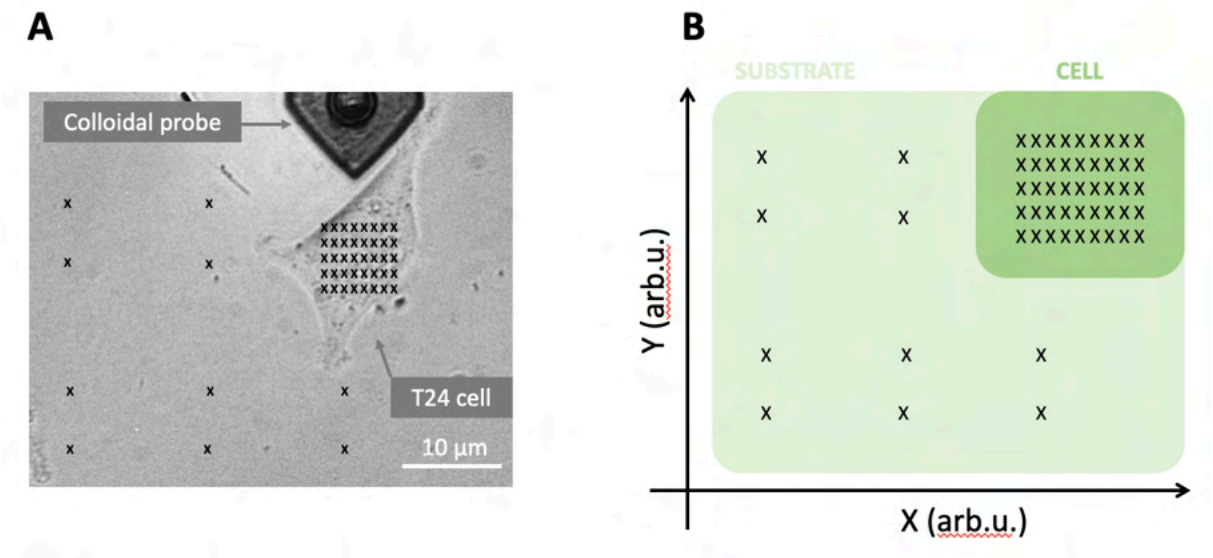

Figure 34. (A) Schematic of the grid of point made during the AFM measurements, both on the substrate and on the cell. (B) Allowing for reconstruction of the height of each point of the cells, according to the fitted substrate plane.

This method allowed for the reconstruction of the local plane-fitted undeformed cell topography as shown in **Figure 34B**. The accurate reconstruction of the local cell's height is essential to implement the finite thickness correction [134]. Thanks to this newly developed method, we were able to reduce the time of acquisition from 40 min-1hour to 10 min, which in principle would allow to measure at least 4 times more cells in the same amount of time, for sake of stronger statistics. This novel imaging method could also help in the characterizing of larger cells, such as potentially hundreds of micron-long fibroblast or neuronal cells, bigger than the scan capacities of the AFM. Both methods have been used complementarily for the characterization of the bladder cancer cells' mechanics as shown in **Figure 35**.

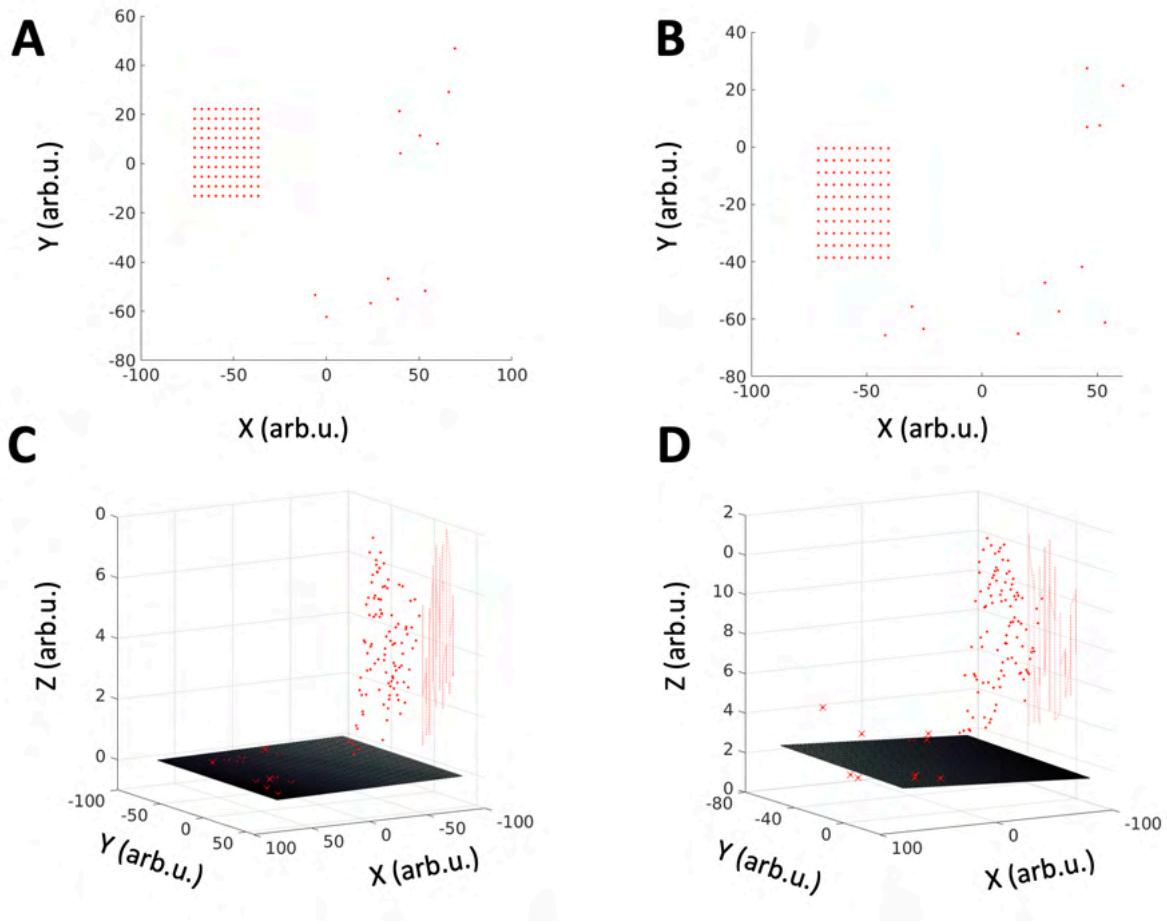

Figure 35. (A and B) Representation of the partial method mapping in 2D and (C and D) 3D on two different T24 cells.

7.2. Finite thickness correction on confluent cell monolayers: when the local thickness is not directly measurable

The Phys2BioMed project aimed at developing standard AFM methods for the nanomechanical mapping of cells and tissues. To standardize the mechanical measurements on cells, it was decided to send same cells to different labs, where the cellular samples were prepared, measured and data analysed according to common established procedures. The

work presented here contributed to an upcoming paper on the standardization of mechanical measurements of cells in the context of the Phys2BioMed project [192]. Measurements have been carried out therefore in different laboratories, with different AFM equipment (including commercial nanoindenters) and operators, on a monolayer of pancreatic cells, PANC-1. Nanoindentation on a monolayer of cells was selected as a reliable cells' seeding control, allowing all the different partners to measure the cells at the same confluency degree.

The finite thickness correction corrects the influence of a stiff substrate on the mechanical measurement of thin and soft samples, making the elastic response stiffer (higher Young's Modulus) than in the case of a thick sample[116,118]. This is required when the sample thickness h is not large compared to the maximum contact radius $a = \sqrt{R\delta}$, where R is the tip radius. The non-dimensional parameter $\chi = \frac{\sqrt{R\delta}}{h}$ must be much smaller than 1 for the finite thickness effect being negligible. When CPs are used (large R) this condition can be hardly satisfied, especially when indenting up to 1-2 µm on relatively thin systems like cells. For the finite thickness correction, the experimentally measured force vs indentation curve must be divided by a polynomial correction function before the Hertz equation can be fitted to it. The details of this correction are reported in the paper presented in the Introduction, Holuigue et al. 2022 [85].

The value of the χ factor was close to 2 for the hemispherical tip and the typical maximum indentation we used during the cell standardization experiments (R = 5,5µm and δ < 1µm (**Figure 36**).

The drawback of measuring a cell monolayer is the impossibility to directly measure the local height of the cells, given that the underlying reference substrate is typically non accessible by the tip; this limitation in principle makes it impossible the application of the standard finite thickness correction. When comparing the results of the measurements from different labs, the dispersion of Young's modulus values due to the changes in the local thickness of the cell layer can severely hamper the interpretation of results, in particular it becomes difficult to assess whether the observed differences are due to methodological issues or to the finite thickness effect.

With the objective of allowing the implementation of the finite thickness correction also in the case of confluent cell layers and similar systems, we developed a new method based on the independent assessment of the mean layer thickness, and the use of the topographic maps calculated from the FCs to calculate the relative thickness variations around the mean value. The mean layer thickness can be conveniently and accurately evaluated through either optical confocal images and/or other microscopy techniques, including AFM itself, from those few maps where the substrate is exposed (provided they exist, and are numerous enough).

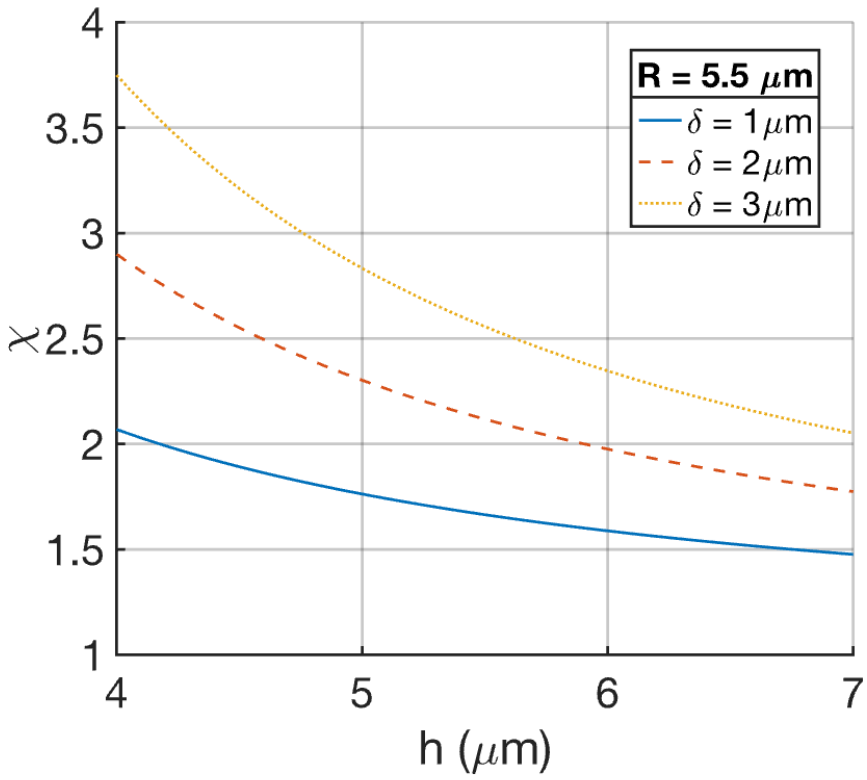

Figure 36. Estimation of the χ, according to Dimtriadis et al.[116] parameters for a fixed radius of 5,5 µm and indentation from 1 to 3 µm.

The evaluation of the cell height for the finite thickness corrected monolayer of cells was performed as follows:

- The topographic maps Z' (x, y) calculated from the force volumes, (either as the contact point maps, or as the z-sensor height at the force setpoint plus the maximum indentation) are mean-subtracted, so that the new maps represent the relative thickness variation ΔZ (x, y) as presented in **Figure 37**:

$$\Delta Z(x,y) = Z'(x,y) - mean\big(Z'(x,y)\big) \tag{34}$$

- The local thickness of the cell $h(x,y)$ is calculated with the previously measured mean thickness of the whole cell monolayer (h_{mono}) as follows (**Figure 38**):

$$h(x,y) = h_{mono} + \Delta Z(x,y) \tag{35}$$

- Knowing the local height of the cell point by point, it is now possible to implement the finite thickness correction.

In our case, the mean height of the PANC-1 cells was estimated with the classical full mapping method described in Puricelli et al. [134] from two supplementary force volumes acquired on regions where the substrate was exposed and accessible to the AFM tip. The mean cell monolayer thickness was measured as h_{mono} = 5,40 ± 0,30 µm (**Figure 37**)

determined as mean ± standard deviation of the mean (n=2). This value is in good agreement with the value h_{mono} = 5,30 ± 0,09 µm determined as mean ± standard deviation of the mean (n=187) measured by Prof. M. Lekka (IFJPAN, Krakow, Poland) by means of confocal microscopy, on the whole cell layer (which makes it presumably more accurate).

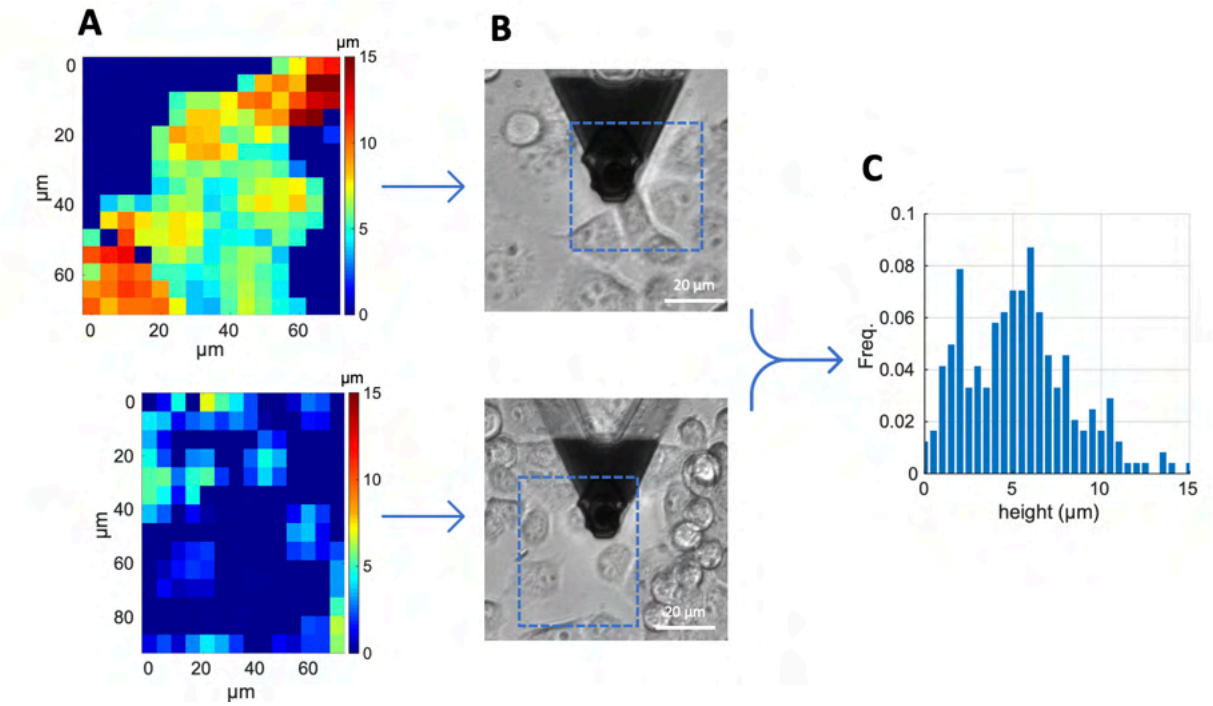

Figure 37. (A) Topographical maps where the substrate is visible with (B) their respective optical images, used for the evaluation of (C) the mean cell's height.

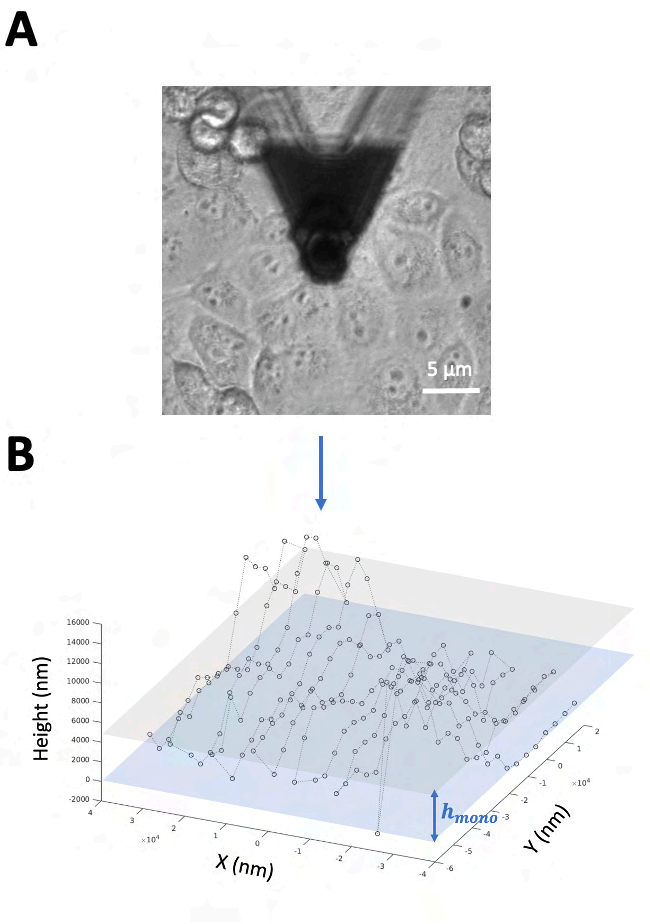

Figure 38. From a zone with (A) a monolayer of cells, we reconstruct (B) the local variation of heights at a mean heigh of h_{mono} defined previously.

With this new method the finite thickness correction was applied on the 10 force volume maps acquired in Milano for the standardization experiments. as shown in **Figure 39**, it was observed a general shift of the Young's Modulus towards lower values, which is typical result of the finite thickness effect correction: the median Young's modulus value decreased from 501,1 $\pm$ 8,8 Pa to 239,9 $\pm$ 10,7 Pa after the correction. Errors are evaluated as the standard deviation of the mean (n=241). With this newly developed method it is possible to assess the contribution of the glass substrate—in this example, the petri dish—in experiments involving cell monolayers, and allow for the finite thickness correction. This approach was then implemented to the standardisation of cell's mechanics in an upcoming paper of the Phys2BioMed project[192].

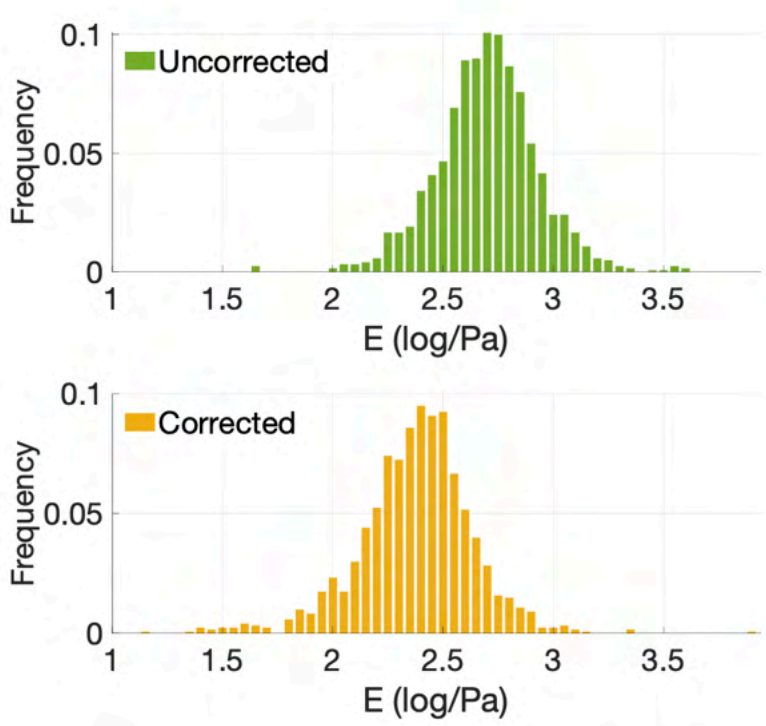

Figure 39. Histograms of the Young's Modulus of the PANC-1 cells before and after finite thickness correction. The correction was performed on the 10 force volume maps of the cells' monolayer.

8. Appendix B

Cell-cell interaction between bladder cancer cells

As presented in the Introduction, the cell's microenvironment consists in the extracellular matrix, that we studied both in Chapter 2 and Chapter 3, but also it includes its neighbouring cells. The importance of their mutual interaction regulates tumour progression and metastasis as well as normal cell development [1,13,193]. Using the same bladder cancer cell model as in Chapter 2, we decided to also study the cell-cell interaction. Preliminary cell-cell force spectroscopy experiments have been performed, aiming at understanding another role player in the cell-microenvironment interaction, in the peculiar context of disease: cadherins, the cell-cell junctions.

This work has been performed in collaboration with partners of the Phys2BioMed network, during scientific secondments in the laboratories of Prof. M. Radmacher lab, Institute of biophysics, University of Bremen, Bremen, Germany, and of Prof. C. Franz, NanoLSI, University of Kanazawa, Kanazawa, Japan.

It has been previously demonstrated that the cell models of bladder carcinoma in rat previously used in this thesis express different cadherins [37,194], as resumed in **Table 6**. Preliminary tests, we performed homotypic cell-cell force spectroscopy with the most invasive bladder cell T24, following previously established protocols [105,182,195,196].

Cell / Cadherin presence	E-Cadherins	P-Cadherins	N-Cadherins
RT4	+	+ (cytoplasm)	-
RT112	+	+ (cytoplasm)	+
T24	-	-	+

Table 6. Table summarizing the presence (+) and absence (-) of classical cadherins in the bladder cancer cells RT4, RT112 and T24.

8.1. Material and methods

8.1.1. Tip functionalization to produce single cell probes

We used DNP-like tipless cantilevers (triangular) for cell attachment. The procedure of functionalization of the cantilever consists in activation of surface hydroxyl (-OH) groups on top of the cantilever via oxygen plasma or UV cleaning. It has been noted that the UV procedure demonstrated more reliable and repeatable results. This step was followed by addition of Concanavalin A (ConA, at 2mg/ml for 2 hours), a plant lectin who specifically binds to glycoproteins, and glycolipids [86,105]. Functionalized cantilevers were stored in PBS at 4°C.

8.1.2. Cell culture

For the force spectroscopy measurements, two dishes were necessary: one dish as used as substrate, covered with firmly attached cells that are grown for 2 days; the second dish was used to provide suspended cells by detaching them with trypsin and resuspend them in their regular medium[105,182,195]. The suspended cells were then transferred in the first petri containing the cell layer and that petri was used directly for measurements. By this method, there was no necessity of changing petri for the creation of the cantilever and the measurements.

8.1.3. Experimental setup

ConA cantilevers were placed on top of a suspended cells, and the attachment was performed by approaching manually the cell with a maximum loading force of 3nN for 10 to 20s contact time. The cell-cantilever assembly was then left few µm away from the bottom of the petri dish during the time necessary to observe firm adhesion of the cell to the tip of the cantilever (**Figure 40**). Cell-cell Force Spectroscopy experiments were then carried out on firmly attached cells (**Figure 41A**), and a minimum of 3 force curves per cells were collected, at each contact time (1, 20, 60 and 120s). Maximum loading force was 1nN, and ramp frequency was 1Hz; we performed the experiment on 3 cells per condition.

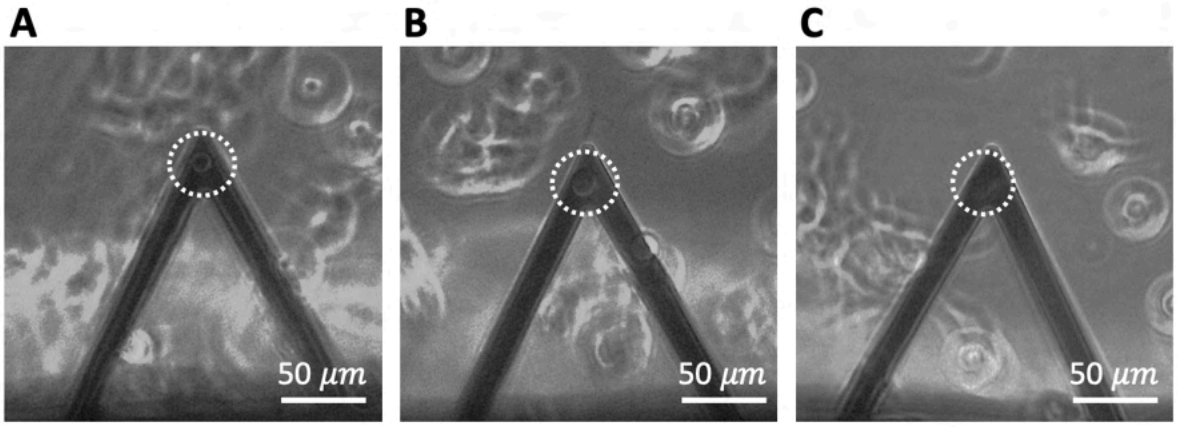

Figure 40. Evolution of the attachment of the cells to the cantilever (from A to C). Out of focus the cells firmly attached to the Petri dish and the rounded suspended cells are visible. Images taken at NanoLSI, Kanazawa University, Japan.

8.2. Results and discussion

The cell-cell experiments have been both performed in the laboratory of Prof. M. Radmacher, at the University of Bremen, Institute of Biophysics, Germany, with an MFP3D (Asylum research) with a homemade setup for CO_2 addition during measurement (5% of CO2). The attachment protocol previously established on MDCK and fibroblast cells [195] was validated on bladder cells, both T24 and RT. Due to the short range of the z-piezo at University of Bremen, like in most of AFM, ~15µm, we were not able to fully detach the cells, inducing incomplete detection of jumps and tethers as well as underestimation of the total work (**Figure 41B**).

We thus decided to pursue the experiment with Prof. C. Franz at NanoLSI, University of Kanazawa, Japan with the CellHesion system on the Nanowizard II (JPK) as shown in **Figure 15**. Indeed, while our protocol of attachment of the cells developed was also confirmed we benefited from the higher piezo range of this instrumental setup to have full detachment of the cells, as presented in **Figure 42A** in comparison to **Figure 41B**.

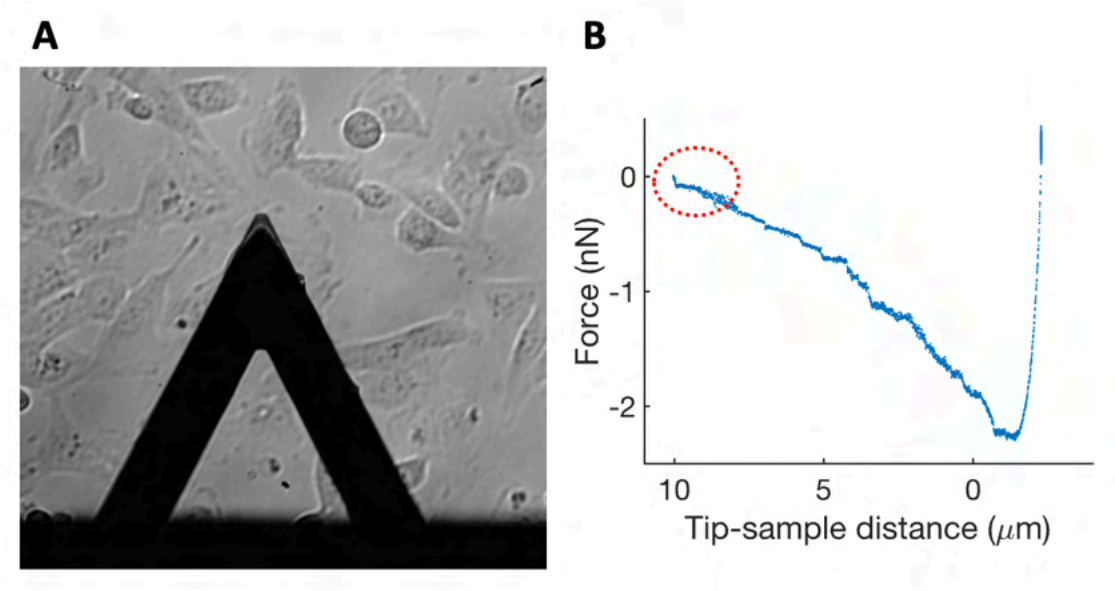

Figure 41. Image of the cell-cantilever on top of T24 cells, rounded cells are the suspended ones used for the creation of the cell-cantilever (A). Representative retracting FC of the detachment of the T24 cell during homotypic contact at 120s. Highlighted in red, the unfinished recorded of an event (B). Image taken at Institute of Biophysics, University of Bremen, Germany.

While data curation for mechanical measurement is quite similar in all labs with the Hertz model [131,132], cell-cell adhesion force spectroscopy data analysis is not yet standardized[113,195]. The main difference arises from the detection of events and their interpretation. While in the University of Kanazawa the AFM software of JPK implemented a direct option for events detection (**Figure 42**), at the University of Bremen this was implemented through a custom code written in Igor (wave metrics, Lake Oswego, OR, USA) [195] for step detection and identification of tethers and jumps, developed by Prof. M. Radmacher.

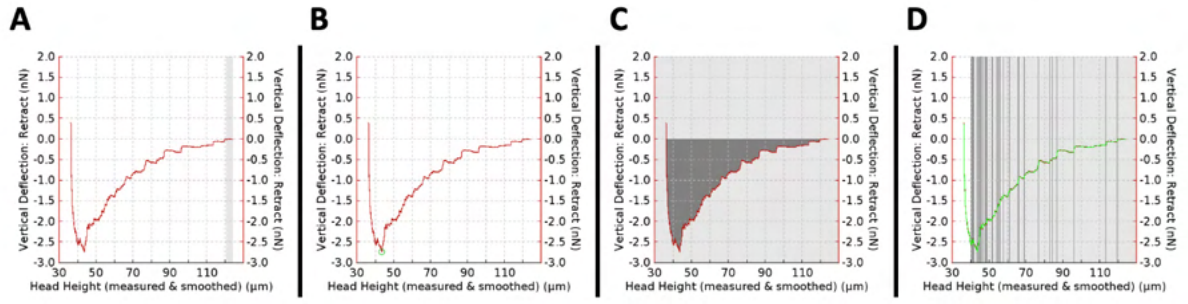

Figure 42. Data processing at NanoLSI, University of Kanazawa, Japan of the force spectroscopy measurements. (A) The selection of the baseline followed by the detection of (B) maximum adhesion force, (C) work and (D) number of events.

The preliminary experiment was performed with T24 cells (**Figure 43**) on three consecutive days at four different contact time (1,20,60 and 120 s). We extracted three main parameters:

the mean work W , the mean adhesion F_a and the mean number of events N_{tot} [113,135]. Errors were calculated as presented in general material and methods. We observe the increase of both work and adhesion force with the contact time (**Figure 43A, B**), both in accordance day to day up to 120s contact time. The number of events (both jumps and tethers) reported in contrary show no variations at contact time higher than 20s (**Figure 43C**).

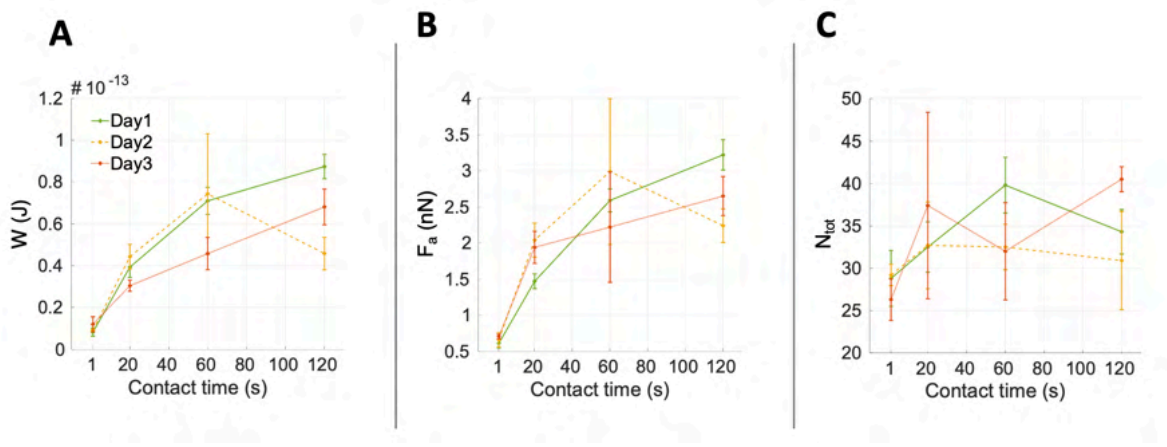

Figure 43. Results of preliminary cell-cell experiments on T24 cells on three consecutive days at four different contact time (1, 20,60 and 120 seconds): The mean work W, the mean adhesion F_a and the mean number of events N_{tot} are reported.

8.3. Conclusions

While the cell-cell force spectroscopy experiments performed so far are preliminary and not conclusive, they gave us the opportunity to evaluate the main issues of the cell-cell force spectroscopy techniques and offered the possibility to study other cell-microenvironment interaction configurations.

Automatic distinction between jumps and tethers is one of the critical parts of the force spectroscopy analysis; the implementation of a robust, automatic, and in general standardized data analysis of the force spectroscopy experiments is challenging.

The complete detachment of cells while in contact requires the use of large z-piezo range stages, which are not available in all setups.

Additional experiments, especially inhibiting of the both E and N-cadherins using Anti-E cadherins antibody and ADH-1 (N-cadherins antagonist) could give an insight of the cell-cell interactions, in hetero and homotypic linkage in the special context of bladder carcinoma.

Acknowledgments

Firstly, and above all I would like to thank my supervisor Prof. Alessandro Podestà, who gave me the incredible opportunity to be part of EU project Phys2BioMed (grant agreements N°812772). His support throughout those 3 years meant a lot to me and I am grateful for the chance I had to work with him. Thank you to Antonia Samorè with her help within Phys2BioMed.

Matteo Chighizola knows already all the gratitude I have for him and his precious advice in every situation, but I hope he'll appreciate me saying it once again: Thank you, a lot. Obviously, Ewelina Lorenc, I am more than happy our path crossed each other and if I managed 3 years of PhD is because I had someone to share my ups and down with. Not happy we shared cells' contamination though…

I thought that the quote from those precise episodes of Big Bang Theory illustrated exactly what I want to say to Chiara Lunardi (S9E1 7:53, replace by your name), Gianlù Martini (S7E6 09:33, without sarcasm) and Matteo Mirigliano (S2E4 17:23). A huge thanks to CIMANIACI: Being in a nice lab is important, being surrounded by amazing people is another level: Anita, Sara, Matteo G., Marco, Lorenzo, Marta, Filippo, Giacomo, Michele, Federica, and Davide.

A special thanks to Dominika and Maria-Leonor for being such wonderful persons.

~

Thank you to all the supervisors, colleagues, and collaborators who, in the context of Phys2BioMed and my PhD supported my work: Prof. Manfred Radmacher, Sandra, Shruti and Nina; Dr. Benjamin Walter, Dr. Marc Faucher, Édouard and VMicro team; Prof. Clemens Franz, You-roung, Tareg and Lucky; Prof. Giuseppe Diaferia, Dr. Massimo Alfano, Prof. A. Moroni, Dr. C. Schulte.

~

This thesis is also the conclusion of 8 years of study, and I have once again to thank the teachers and professors who motivated me to pursue my career in science: Mr. Aurélien Cocheteux (Lycée Saint Rémi), Prof. Normand Beaudouin (Université de Moncton), Prof. Silvain Cristol (Université de Lille), Prof. Michal Wozniakiewicz (Uniwersytet Jagielloński).

~

Ces remerciements seront en français pour que les personnes citées puissent le lire. Je remercie ma famille : Maman, Papa, Cheick et Helin qui m'ont toujours soutenue et qui croient en moi. Je dédie cette thèse cette fois ci plus particulièrement à tous mes grands-parents qui m'ont appris que la vie simple, proche des siens valait plus que tout l'or du monde.

Merci à mes amis, toujours là à me motiver et à me suivre dans mes voyages aux quatre coins du monde : Lisa, Eliot, Noémie, Amina, Cora-lee, Célie, Ornella, Ada et bien évidement le « 100 ».

Remerciement également aux « français de Milan » et plus particulièrement à Alexiane, Kévin et Shiro.

L'histoire s'écrit en tournant les pages.

L’écriture est une histoire de famille, pour papi, Robert Lahens.

Bibliography

1. Alberts, Bruce. *Essential cell biology*. *Molecular Reproduction and Development* vol. 51 (Garland Science Pub., 1998).
2. Frantz, C., Stewart, K. M. & Weaver, V. M. The extracellular matrix at a glance. *J Cell Sci* **123**, 4195–4200 (2010).
3. Schaefer, L. & Schaefer, R. M. Proteoglycans: From structural compounds to signaling molecules. *Cell Tissue Res* **339**, 237–246 (2010).
4. Durbeej, M. Laminins. *Cell Tissue Res* **339**, 259–268 (2010).
5. Timpl, R. *et al.* Laminin - A glycoprotein from basement membranes. *Journal of Biological Chemistry* **254**, 9933–9937 (1979).
6. Theocharis, A. D., Skandalis, S. S., Gialeli, C. & Karamanos, N. K. Extracellular matrix structure. *Adv Drug Deliv Rev* **97**, 4–27 (2016).
7. Gauthier, N. C. & Roca-Cusachs, P. Mechanosensing at integrin-mediated cell–matrix adhesions: from molecular to integrated mechanisms. *Curr Opin Cell Biol* **50**, 20–26 (2018).
8. Huang, J. *et al.* Extracellular matrix and its therapeutic potential for cancer treatment. *Signal Transduct Target Ther* **6**, 153 (2021).
9. Kechagia, J. Z., Ivaska, J. & Roca-Cusachs, P. Integrins as biomechanical sensors of the microenvironment. *Nat Rev Mol Cell Biol* **20**, 457–473 (2019).
10. Hynes, R. O. Integrins: Bidirectional, allosteric signaling machines. *Cell* **110**, 673–687 (2002).
11. Takada, Y., Ye, X. & Simon, S. The integrins. *Genome Biol* **8**, 215 (2007).
12. Seetharaman, S. & Etienne-Manneville, S. Cytoskeletal Crosstalk in Cell Migration. *Trends Cell Biol* **30**, 720–735 (2020).
13. Leckband, D. E. & de Rooij, J. Cadherin adhesion and mechanotransduction. *Annu Rev Cell Dev Biol* **30**, 291–315 (2014).
14. Omidvar, R., Tafazzoli-shadpour, M., Shokrgozar, M. A. & Rostami, M. Atomic force microscope-based single cell force spectroscopy of breast cancer cell lines: An approach for evaluating cellular invasion. *J Biomech* **47**, 3373–3379 (2014).
15. Schulte, C. Mechanotransduction. in *Mechanics of Cells and Tissues in Diseases* (eds. Lekka, M., Navajas, D., Radmacher, M. & Podestà, A.) vol. 1 (DeGruyter, 2023).
16. Chighizola, M. *et al.* Mechanotransduction in neuronal cell development and functioning. *Biophysical Reviews* vol. 11 701–720 Preprint at https://doi.org/10.1007/s12551-019-00587-2 (2019).
17. Jaalouk, D. E. & Lammerding, J. Mechanotransduction gone awry. *Nat Rev Mol Cell Biol* **10**, 63–73 (2009).
18. Hamidi, H., Pietilä, M. & Ivaska, J. The complexity of integrins in cancer and new scopes for therapeutic targeting. *Br J Cancer* **115**, 1017–1023 (2016).

19. Elosegui-Artola, A., Trepat, X. & Roca-Cusachs, P. Control of Mechanotransduction by Molecular Clutch Dynamics. *Trends Cell Biol* **28**, 356–367 (2018).

20. Humphrey, J. D., Dufresne, E. R. & Schwartz, M. A. Mechanotransduction and extracellular matrix homeostasis. *Nat Rev Mol Cell Biol* **15**, 802–812 (2014).

21. Strohmeyer, N., Bharadwaj, M., Costell, M., Fässler, R. & Müller, D. J. Fibronectin-bound α5β1 integrins sense load and signal to reinforce adhesion in less than a second. *Nat Mater* **16**, 1262–1270 (2017).

22. Fu, B. M. & Tarbell, J. M. Mechano-sensing and transduction by endothelial surface glycocalyx: Composition, structure, and function. *Wiley Interdiscip Rev Syst Biol Med* **5**, 381–390 (2013).

23. Paszek, M. J., Boettiger, D., Weaver, V. M. & Hammer, D. A. Integrin Clustering Is Driven by Mechanical Resistance from the Glycocalyx and the Substrate. *PLoS Comput Biol* **5**, e1000604 (2009).

24. Paszek, M. J. *et al.* The cancer glycocalyx mechanically primes integrin-mediated growth and survival. *Nature* **511**, 319–325 (2014).

25. Iyer, S., Gaikwad, R. M., Subba-Rao, V., Woodworth, C. D. & Sokolov, I. Atomic force microscopy detects differences in the surface brush of normal and cancerous cells. *Nat Nanotechnol* **4**, 389–393 (2009).

26. Schmidt, S. *et al.* Glycocalyx-mediated cell adhesion and migration. *bioRxiv* 2020.06.12.149096 (2020) doi:10.1101/2020.06.12.149096.

27. Buffone, A. & Weaver, V. M. Don't sugarcoat it: How glycocalyx composition influences cancer progression. *Journal of Cell Biology* **219**, (2020).

28. van den Berg, B. M., Vink, H. & Spaan, J. A. E. The endothelial glycocalyx protects against myocardial edema. *Circ Res* **92**, 592–594 (2003).

29. Hanahan, D. & Weinberg, R. A. The hallmarks of cancer. *Cell* **100**, 57–70 (2000).

30. Hanahan, D. & Weinberg, R. A. Hallmarks of cancer: The next generation. *Cell* **144**, 646–674 (2011).

31. Rice, A. & del Rio Hernandez, A. Biomechanics of cancer cells. in *Bioengineering Innovative Solutions for Cancer* 327–361 (Elsevier, 2019). doi:10.1016/B978-0-12-813886-1.00014-0.

32. Ferlay, J. *et al.* Cancer statistics for the year 2020: An overview. *Int J Cancer* **149**, 778–789 (2021).

33. Wang, N. *et al.* Directly observing alterations of morphology and mechanical properties of living cancer cells with atomic force microscopy. *Talanta* **191**, 461–468 (2019).

34. Cox, T. R. The matrix in cancer. *Nat Rev Cancer* **21**, 217–238 (2021).

35. Hulit, J. *et al.* N-cadherin signaling potentiates mammary tumor metastasis via enhanced extracellular signal-regulated kinase activation. *Cancer Res* **67**, 3106–3116 (2007).

36. Loh, C. Y. *et al.* The e-cadherin and n-cadherin switch in epithelial-to-mesenchymal transition: Signaling, therapeutic implications, and challenges. *Cells* **8**, 1118 (2019).

37. Mialhe, A. *et al.* Expression of E-, P-, N-cadherins and catenins in human bladder carcinoma cell lines. *Journal of Urology* **164**, 826–835 (2000).

38. Kalluri, R. & Weinberg, R. A. The basics of epithelial-mesenchymal transition. *Journal of Clinical Investigation* vol. 119 1420–1428 Preprint at https://doi.org/10.1172/JCI39104 (2009).

39. Kalluri, R. & Weinberg, R. A. The basics of epithelial-mesenchymal transition. *Journal of Clinical Investigation* **119**, 1420–1428 (2009).

40. Psaila, B. & Lyden, D. The metastatic niche: Adapting the foreign soil. *Nat Rev Cancer* **9**, 285–293 (2009).

41. Kaplan, R. N., Rafii, S. & Lyden, D. Preparing the 'soil': The premetastatic niche. *Cancer Res* **66**, 11089–11093 (2006).

42. Ramos, J. R., Pabijan, J., Garcia, R. & Lekka, M. The softening of human bladder cancer cells happens at an early stage of the malignancy process. *Beilstein Journal of Nanotechnology* **5**, 447–457 (2014).

43. Lekka, M. *et al.* Elasticity of normal and cancerous human bladder cells studied by scanning force microscopy. *European Biophysics Journal* **28**, 312–316 (1999).

44. Lekka, M. Applicability of atomic force microscopy to determine cancer-related changes in cells. *Philosophical Transactions of the Royal Society A: Mathematical, Physical and Engineering Sciences* **380**, (2022).

45. Lekka, M. *et al.* Cancer cell detection in tissue sections using AFM. *Arch Biochem Biophys* **518**, 151–156 (2012).

46. Efremov, Y. M. *et al.* Distinct impact of targeted actin cytoskeleton reorganization on mechanical properties of normal and malignant cells. *Biochim Biophys Acta Mol Cell Res* **1853**, 3117–3125 (2015).

47. Pachenari, M. *et al.* Mechanical properties of cancer cytoskeleton depend on actin filaments to microtubules content: Investigating different grades of colon cancer cell lines. *J Biomech* **47**, 373–379 (2014).

48. Kuo, J. C.-H., Gandhi, J. G., Zia, R. N. & Paszek, M. J. Physical biology of the cancer cell glycocalyx. *Nat Phys* **14**, 658–669 (2018).

49. Tarbell, J. M. & Cancel, L. M. The glycocalyx and its significance in human medicine. *J Intern Med* **280**, 97–113 (2016).

50. Kang, H. *et al.* Cancer cell glycocalyx and its significance in cancer progression. *Int J Mol Sci* **19**, 2484 (2018).

51. Mitchell, M. J. & King, M. R. Physical biology in cancer. 3. The role of cell glycocalyx in vascular transport of circulating tumor cells. *Am J Physiol Cell Physiol* **306**, C89–C97 (2014).

52. Cox, T. R. & Erler, J. T. Molecular pathways: Connecting fibrosis and solid tumor metastasis. *Clinical Cancer Research* **20**, 3637–3643 (2014).

53. Stern, R. Hyaluronidases in Cancer Biology. in *Hyaluronan in Cancer Biology* 207–220 (Elsevier, 2008). doi:10.1016/B978-012374178-3.10012-2.

54. Lu, P., Weaver, V. M. & Werb, Z. The extracellular matrix: A dynamic niche in cancer progression. *Journal of Cell Biology* **196**, 395–406 (2012).

55. Genovese, L. *et al.* Cellular localization, invasion, and turnover are differently influenced by healthy and tumor-derived extracellular matrix. *Tissue Eng Part A* **20**, 2005–2018 (2014).

56. Provenzano, P. P. *et al.* Collagen reorganization at the tumor-stromal interface facilitates local invasion. *BMC Med* **4**, 38 (2006).

57. Deville, S. S. & Cordes, N. The Extracellular, Cellular, and Nuclear Stiffness, a Trinity in the Cancer Resistome—A Review. *Front Oncol* **9**, (2019).

58. Grasset, E. M. *et al.* Matrix Stiffening and EGFR cooperate to promote the collective invasion of cancer cells. *Cancer Res* **78**, 5229–5242 (2018).

59. Acerbi, I. *et al.* Human breast cancer invasion and aggression correlates with ECM stiffening and immune cell infiltration. *Integrative Biology (United Kingdom)* **7**, 1120–1134 (2015).

60. Erler, J. T. *et al.* Hypoxia-Induced Lysyl Oxidase Is a Critical Mediator of Bone Marrow Cell Recruitment to Form the Premetastatic Niche. *Cancer Cell* **15**, 35–44 (2009).

61. Najafi, M., Farhood, B. & Mortezaee, K. Extracellular matrix (ECM) stiffness and degradation as cancer drivers. *J Cell Biochem* **120**, 2782–2790 (2019).

62. Acerbi, I. *et al.* Human breast cancer invasion and aggression correlates with ECM stiffening and immune cell infiltration. *Integrative Biology (United Kingdom)* **7**, 1120–1134 (2015).

63. Plodinec, M. *et al.* The nanomechanical signature of breast cancer. *Nat Nanotechnol* **7**, 757–765 (2012).

64. Nebuloni, M. *et al.* Insight on Colorectal Carcinoma Infiltration by Studying Perilesional Extracellular Matrix. *Sci Rep* **6**, 22522 (2016).

65. Varinelli, L. *et al.* Decellularized Normal and Tumor Extracellular Matrix as Scaffold for Cancer Organoid Cultures of Colorectal Peritoneal Metastases. *bioRxiv* 2021.07.15.452437 (2021) doi:10.1101/2021.07.15.452437.

66. Lorenc, E. *et al.* The nanomechanical fingerprint of colorectal-derived peritoneal metastasis. *Biorvix* (2022).

67. Levental, K. R. *et al.* Matrix Crosslinking Forces Tumor Progression by Enhancing Integrin Signaling. *Cell* **139**, 891–906 (2009).

68. Zhang, J. & Reinhart-King, C. A. Targeting Tissue Stiffness in Metastasis: Mechanomedicine Improves Cancer Therapy. *Cancer Cell* **37**, 754–755 (2020).

69. Ajalloueian, F., Lemon, G., Hilborn, J., Chronakis, I. S. & Fossum, M. Bladder biomechanics and the use of scaffolds for regenerative medicine in the urinary bladder. *Nat Rev Urol* **15**, 155–174 (2018).

70. Knowles, M. A. & Hurst, C. D. Molecular biology of bladder cancer: New insights into pathogenesis and clinical diversity. *Nat Rev Cancer* **15**, 25–41 (2015).

71. Liu, H. *et al.* Biophysical Characterization of Bladder Cancer Cells with Different Metastatic Potential. *Cell Biochem Biophys* **68**, 241–246 (2014).

72. Lekka, M. *et al.* Cancer cell recognition - Mechanical phenotype. *Micron* **43**, 1259–1266 (2012).

73. Lekka, M. Discrimination Between Normal and Cancerous Cells Using AFM. *Bionanoscience* **6**, 65–80 (2016).

74. Nenadic, I. Z. *et al.* Ultrasound bladder vibrometry method for measuring viscoelasticity of the bladder wall. *Phys Med Biol* **58**, 2675–2695 (2013).

75. Alfano, M. *et al.* Linearized texture of three-dimensional extracellular matrix is mandatory for bladder cancer cell invasion. *Sci Rep* **6**, 36128 (2016).

76. Binnig, G., Quate, C. F. & Gerber, C. Atomic force microscope. *Phys Rev Lett* **56**, 930–933 (1986).

77. Eaton, P. & West, P. AFM instrumentation. in *Atomic Force Microscopy* (eds. Lekka, M., Navajas, D., Radmacher, M. & Podestà, A.) vol. 1 9–48 (DeGruyter, 2010).

78. Chighizola, M., Rodriguez-Ramo, J., Rico, F., Manfred, R. & Podestà, A. AFM Calibration Issues. in *Mechanics of Cells and Tissues in Diseases* (eds. Lekka, M., Navajas, D., Radmacher, M. & Podestà, A.) vol. 1 (2023).

79. Putman, C. A. J., de Grooth, B. G., van Hulst, N. F. & Greve, J. *A detailed analysis of the optical beam deflection technique for use in atomic force microscopy*. *Journal of Applied Physics* vol. 72 http://ojps.aip.org/japo/japcr.jsp (1992).

80. Alexander, S. *et al.* An atomic-resolution atomic-force microscope implemented using an optical lever. *J Appl Phys* **65**, 164 (1998).

81. Eaton, P. & West, P. *Atomic Force Microscopy*. *Atomic Force Microscopy* vol. 9780199570 (Oxford University Press, 2010).

82. Lekka, M., Navajas, D., Radmacher, M. & Podestà, A. *Mechanics of Cells and Tissues in Diseases*. vol. 2 (De Gruyter , 2023).

83. Butt, H. J., Cappella, B. & Kappl, M. Force measurements with the atomic force microscope: Technique, interpretation and applications. *Surf Sci Rep* **59**, 1–152 (2005).

84. Adams, G. G. Contact mechanics. in *Handbook of Lubrication and Tribology, Volume II: Theory and Design, Second Edition* (eds. Lekka, M., Navajas, D., Radmacher, M. & Podestà, A.) vol. 1 4-1-4–20 (DeGruyter, 2012).

85. Holuigue, H. *et al.* Force Sensing on Cells and Tissues by Atomic Force Microscopy. *Sensors* **22**, 2197 (2022).

86. Friedrichs, J., Helenius, J. & Muller, D. J. Quantifying cellular adhesion to extracellular matrix components by single-cell force spectroscopy. *Nat Protoc* **5**, 1353–1361 (2010).

87. Neuman, K. C. & Nagy, A. Single-molecule force spectroscopy: Optical tweezers, magnetic tweezers and atomic force microscopy. *Nat Methods* **5**, 491–505 (2008).

88. Benoit, M., Gabriel, D., Gerisch, G. & Gaub, H. E. Discrete interactions in cell adhesion measured by single-molecule force spectroscopy. *Nat Cell Biol* **2**, 313–317 (2000).

89. Alessandrini, A. & Facci, P. AFM: A versatile tool in biophysics. *Meas Sci Technol* **16**, 65–92 (2005).

90. Chièze, L. *et al.* Quantitative characterization of single-cell adhesion properties by atomic force microscopy using protein-functionalized microbeads. *Journal of Molecular Recognition* **32**, e2767 (2019).

91. Helenius, J., Heisenberg, C. P., Gaub, H. E. & Muller, D. J. Single-cell force spectroscopy. *J Cell Sci* **121**, 1785–1791 (2008).

92. Yu, M., Wang, J., Muller, D. J. & Helenius, J. In PC3 prostate cancer cells ephrin receptors crosstalk to β1-integrins to strengthen adhesion to collagen type i. *Sci Rep* **5**, 8206 (2015).

93. Gaub, B. M. & Müller, D. J. Mechanical Stimulation of Piezo1 Receptors Depends on Extracellular Matrix Proteins and Directionality of Force. *Nano Lett* **17**, 2064–2072 (2017).

94. Kienberger, F. *et al.* Static and Dynamical Properties of Single Poly(Ethylene Glycol) Molecules Investigated by Force Spectroscopy. *Single Molecules* **1**, 123–128 (2000).

95. Sumbul, F., Marchesi, A., Takahashi, H., Scheuring, S. & Rico, F. High-speed force spectroscopy for single protein unfolding. in *Methods in Molecular Biology* vol. 1814 243–264 (Humana Press Inc., 2018).

96. Müller, D. J., Helenius, J., Alsteens, D. & Dufrne, Y. F. Force probing surfaces of living cells to molecular resolution. *Nature Chemical Biology* vol. 5 383–390 Preprint at https://doi.org/10.1038/nchembio.181 (2009).

97. Friedrichs, J. *et al.* A practical guide to quantify cell adhesion using single-cell force spectroscopy. *Methods* **60**, 169–178 (2013).

98. Ozkan, A. D. *et al.* Probe microscopy methods and applications in imaging of biological materials. *Semin Cell Dev Biol* **73**, 153–164 (2018).

99. Radmacher, M., Tillmann, R. W., Fritz, M. & Gaub, H. E. From molecules to cells: Imaging soft samples with the atomic force microscope. *Science (1979)* **257**, 1900–1905 (1992).

100. Butt, H.-J. *et al.* Imaging cells with the atomic force microscope. *J Struct Biol* **105**, 54–61 (1990).

101. Graham, H. K. *et al.* Tissue section AFM: In situ ultrastructural imaging of native biomolecules. *Matrix Biology* **29**, 254–260 (2010).

102. Caplan, J., Niethammer, M., Taylor, R. M. & Czymmek, K. J. The power of correlative microscopy: Multi-modal, multi-scale, multi-dimensional. *Curr Opin Struct Biol* **21**, 686–693 (2011).

103. Janel, S., Werkmeister, E., Bongiovanni, A., Lafont, F. & Barois, N. CLAFEM: Correlative light atomic force electron microscopy. in *Methods in Cell Biology* vol. 140 165–185 (2017).

104. Janel, S. *et al.* Stiffness tomography of eukaryotic intracellular compartments by atomic force microscopy. *Nanoscale* **11**, 10320–10328 (2019).

105. Puech, P. H., Poole, K., Knebel, D. & Muller, D. J. A new technical approach to quantify cell-cell adhesion forces by AFM. *Ultramicroscopy* **106**, 637–644 (2006).

106. Franz, C. M. & Müller, D. J. Analyzing focal adhesion structure by atomic force microscopy. *J Cell Sci* **118**, 5315–5323 (2005).

107. Roduit, C. *et al.* Stiffness tomography by atomic force microscopy. *Biophys J* **97**, 674–677 (2009).

108. Abramczyk, H., Imiela, A., Brozek-Pluska, B. & Kopec, M. Advances in Raman imaging combined with AFM and fluorescence microscopy are beneficial for oncology and cancer research. *Nanomedicine* **14**, 1873–1888 (2019).

109. McEwen, G. D., Wu, Y. & Zhou, A. Probing nanostructures of bacterial extracellular polymeric substances versus culture time by Raman microspectroscopy and atomic force microscopy. *Biopolymers* **93**, 171–177 (2010).

110. Dazzi, A. & Prater, C. B. AFM-IR: Technology and applications in nanoscale infrared spectroscopy and chemical imaging. *Chem Rev* **117**, 5146–5173 (2017).

111. Indrieri, M., Podestà, A., Bongiorno, G., Marchesi, D. & Milani, P. Adhesive-free colloidal probes for nanoscale force measurements: Production and characterization. *Review of Scientific Instruments* **82**, 023708 (2011).

112. Chighizola, M., Puricelli, L., Bellon, L. & Podestà, A. Large colloidal probes for atomic force microscopy: Fabrication and calibration issues. *Journal of Molecular Recognition* **34**, e2879 (2021).

113. Chighizola, M. *et al.* Adhesion force spectroscopy with nanostructured colloidal probes reveals nanotopography-dependent early mechanotransductive interactions at the cell membrane level. *Nanoscale* **12**, 14708–14723 (2020).

114. Chaudhuri, O. *et al.* Extracellular matrix stiffness and composition jointly regulate the induction of malignant phenotypes in mammary epithelium. *Nat Mater* **13**, 970–978 (2014).

115. Ebner, A., Wildling, L. & Gruber, H. J. Functionalization of AFM tips and supports for molecular recognition force spectroscopy and recognition imaging. in *Methods in Molecular Biology* vol. 1886 117–151 (Humana Press Inc., 2019).

116. Dimitriadis, E. K., Horkay, F., Maresca, J., Kachar, B. & Chadwick, R. S. Determination of Elastic Moduli of Thin Layers of Soft Material Using the Atomic Force Microscope. *Biophys J* **82**, 2798–2810 (2002).

117. Gavara, N. & Chadwick, R. S. Determination of the elastic moduli of thin samples and adherent cells using conical atomic force microscope tips. *Nat Nanotechnol* **7**, 733–736 (2012).

118. Garcia, P. D. & Garcia, R. Determination of the Elastic Moduli of a Single Cell Cultured on a Rigid Support by Force Microscopy. *Biophys J* **114**, 2923–2932 (2018).

119. Butt, H. J. & Jaschke, M. Calculation of thermal noise in atomic force microscopy. *Nanotechnology* **6**, 1–7 (1995).

120. Hutter, J. L. & Bechhoefer, J. Calibration of atomic-force microscope tips. *Review of Scientific Instruments* **64**, 1868–1873 (1993).

121. Hutter, J. *Calibration of AFM Cantilevers*. http://www.physics.uwo.ca/~hutter/calibration/afmcal.html.

122. Schillers, H. *et al.* Standardized Nanomechanical Atomic Force Microscopy Procedure (SNAP) for Measuring Soft and Biological Samples. *Sci Rep* **7**, 5117 (2017).

123. Sirghi, L., Kylián, O., Gilliland, D., Ceccone, G. & Rossi, F. Cleaning and hydrophilization of atomic force microscopy silicon probes. *Journal of Physical Chemistry B* **110**, 25975–25981 (2006).

124. Holuigue, H. *et al.* Novel native extracellular matrix probes to target patient- and tissue-specific cell-microenvironment interactions by force spectroscopy. *bioRxiv* 2022.12.02.518867 (2022) doi:10.1101/2022.12.02.518867.

125. Vandenberg, E. T. *et al.* Structure of 3-aminopropyl triethoxy silane on silicon oxide. *J Colloid Interface Sci* **147**, 103–118 (1991).

126. Acres, R. G. *et al.* Molecular structure of 3-aminopropyltriethoxysilane layers formed on silanol-terminated silicon surfaces. *Journal of Physical Chemistry C* **116**, 6289–6297 (2012).

127. Fiorilli, S. *et al.* Vapor-phase self-assembled monolayers of aminosilane on plasma-activated silicon substrates. *J Colloid Interface Sci* **321**, 235–241 (2008).

128. Gelmi, A., Higgins, M. J. & Wallace, G. G. Resolving sub-molecular binding and electrical switching mechanisms of single proteins at electroactive conducting polymers. *Small* **9**, 393–401 (2013).

129. Gelmi, A., Higgins, M. J. & Wallace, G. G. Quantifying fibronectin adhesion with nanoscale spatial resolution on glycosaminoglycan doped polypyrrole using Atomic Force Microscopy. *Biochim Biophys Acta Gen Subj* **1830**, 4305–4313 (2013).

130. Nugroho, R. W. N. *et al.* Quantifying the interactions between biomimetic biomaterials – collagen I, collagen IV, laminin 521 and cellulose nanofibrils – by colloidal probe microscopy. *Colloids Surf B Biointerfaces* **173**, 571–580 (2019).

131. Hertz, H. Ueber die Berührung fester elastischer Körper. *Journal fur die Reine und Angewandte Mathematik* **1881**, 156–171 (1881).

132. Kontomaris, S.-V. The Hertz Model in AFM Nanoindentation Experiments: Applications in Biological Samples and Biomaterials. *Micro and Nanosystems* **10**, 11–22 (2018).

133. Gavara, N. A beginner's guide to atomic force microscopy probing for cell mechanics. *Microsc Res Tech* **80**, 75–84 (2017).

134. Puricelli, L., Galluzzi, M., Schulte, C., Podestà, A. & Milani, P. Nanomechanical and topographical imaging of living cells by atomic force microscopy with colloidal probes. *Review of Scientific Instruments* **86**, 33705 (2015).

135. Chighizola, M. *et al.* The glycocalyx affects the mechanotransductive perception of the topographical microenvironment. *J Nanobiotechnology* **20**, 418 (2022).

136. Alfano, M. *et al.* Linearized texture of three-dimensional extracellular matrix is mandatory for bladder cancer cell invasion. *Sci Rep* **6**, 36128 (2016).

137. Sader, J. E., Chon, J. W. M. & Mulvaney, P. Calibration of rectangular atomic force microscope cantilevers. *Review of Scientific Instruments* **70**, 3967–3969 (1999).

138. Heim, L.-O., Rodrigues, T. S. & Bonaccurso, E. Direct thermal noise calibration of colloidal probe cantilevers. *Colloids Surf A Physicochem Eng Asp* **443**, 377–383 (2014).

139. Cleveland, J. P., Manne, S., Bocek, D. & Hansma, P. K. A nondestructive method for determining the spring constant of cantilevers for scanning force microscopy. *Review of Scientific Instruments* **64**, 403–405 (1993).

140. Gates, R. S. & Pratt, J. R. Accurate and precise calibration of AFM cantilever spring constants using laser Doppler vibrometry. *Nanotechnology* **23**, 375702 (2012).

141. Laurent, J., Steinberger, A. & Bellon, L. Functionalized AFM probes for force spectroscopy: Eigenmode shapes and stiffness calibration through thermal noise measurements. *Nanotechnology* **24**, 225504 (2013).

142. Gates, R. S., Osborn, W. A. & Shaw, G. A. Accurate flexural spring constant calibration of colloid probe cantilevers using scanning laser Doppler vibrometry. *Nanotechnology* **26**, 235704 (2015).

143. Kain, L. *et al.* Calibration of colloidal probes with atomic force microscopy for micromechanical assessment. *J Mech Behav Biomed Mater* **85**, 225–236 (2018).

144. Chung, K.-H. H., Shaw, G. A. & Pratt, J. R. Accurate noncontact calibration of colloidal probe sensitivities in atomic force microscopy. *Review of Scientific Instruments* **80**, 065107 (2009).

145. McBride, S. P. & Law, B. M. Improved in situ spring constant calibration for colloidal probe atomic force microscopy. *Review of Scientific Instruments* **81**, 113703 (2010).

146. Witko, T., Baster, Z., Rajfur, Z., Sofińska, K. & Barbasz, J. Increasing AFM colloidal probe accuracy by optical tweezers. *Sci Rep* **11**, 1–10 (2021).

147. Notley, S. M., Biggs, S. & Craig, V. S. J. Calibration of colloid probe cantilevers using the dynamic viscous response of a confined liquid. *Review of Scientific Instruments* **74**, 4026–4032 (2003).

148. Meyer, G. & Amer, N. M. Optical-beam-deflection atomic force microscopy: The NaCl (001) surface. *Appl Phys Lett* **56**, 2100–2101 (1990).

149. Meyer, G. & Amer, N. M. Novel optical approach to atomic force microscopy. *Appl Phys Lett* **53**, 1045–1047 (1988).

150. Higgins, M. J. *et al.* Noninvasive determination of optical lever sensitivity in atomic force microscopy. *Review of Scientific Instruments* **77**, 1–5 (2006).

151. Sader, J. E. *et al.* A virtual instrument to standardise the calibration of atomic force microscope cantilevers. *Review of Scientific Instruments* **87**, 93711 (2016).

152. Burnham, N. A. *et al. Comparison of calibration methods for atomic-force microscopy cantilevers*. *Nanotechnology* vol. 14 (2003).

153. Ohler, B. Cantilever spring constant calibration using laser Doppler vibrometry. *Review of Scientific Instruments* **78**, 63701 (2007).

154. Paolino, P., Aguilar Sandoval, F. A. & Bellon, L. Quadrature phase interferometer for high resolution force spectroscopy. *Review of Scientific Instruments* **84**, 95001 (2013).

155. Sader, J. E., Larson, I., Mulvaney, P. & White, L. R. Method for the calibration of atomic force microscope cantilevers. *Review of Scientific Instruments* **66**, 3789–3798 (1995).

156. Hutter, J. L. *et al.* Atomic force microscopy investigation of the dependence of cellular elastic moduli on glutaraldehyde fixation. *J Microsc* **219**, 61–68 (2005).

157. Cook, S. M. *et al.* Practical implementation of dynamic methods for measuring atomic force microscope cantilever spring constants. *Nanotechnology* **17**, 2135–2145 (2006).

158. Sader, J. E., Lu, J. & Mulvaney, P. Effect of cantilever geometry on the optical lever sensitivities and thermal noise method of the atomic force microscope. *Review of Scientific Instruments* **85**, 113702 (2014).

159. Rodriguez-Ramos, J. & Rico, F. Determination of calibration parameters of cantilevers of arbitrary shape by finite element analysis. *Review of Scientific Instruments* **92**, 045001 (2021).

160. Edwards, S. A., Ducker, W. A. & Sader, J. E. Influence of atomic force microscope cantilever tilt and induced torque on force measurements. *J Appl Phys* **103**, 64513 (2008).

161. Schäffer, T. E. Calculation of thermal noise in an atomic force microscope with a finite optical spot size. *Nanotechnology* **16**, 664–670 (2005).

162. Schäffer, T. E. & Fuchs, H. Optimized detection of normal vibration modes of atomic force microscope cantilevers with the optical beam deflection method. *J Appl Phys* **97**, 83524 (2005).

163. Laurent, J., Steinberger, A. & Bellon, L. Functionalized AFM probes for force spectroscopy: eigenmode shapes and stiffness calibration through thermal noise measurements. *Nanotechnology* **24**, 225504 (2013).

164. Sader, J. E., Pacifico, J., Green, C. P. & Mulvaney, P. General scaling law for stiffness measurement of small bodies with applications to the atomic force microscope. *J Appl Phys* **97**, (2005).

165. Sader, J. E. *et al.* Spring constant calibration of atomic force microscope cantilevers of arbitrary shape. *Review of Scientific Instruments* **83**, 103705 (2012).

166. Sader, J. E. & Friend, J. R. Note: Improved calibration of atomic force microscope cantilevers using multiple reference cantilevers. *Review of Scientific Instruments* **86**, 56106 (2015).

167. Portolés, J. F. *et al.* Accurate velocity measurements of AFM-cantilever vibrations by Doppler interferometry. *J Exp Nanosci* **1**, 51–62 (2006).

168. Gates, R. S., Osborn, W. A. & Pratt, J. R. Experimental determination of mode correction factors for thermal method spring constant calibration of AFM cantilevers using laser Doppler vibrometry. *Nanotechnology* **24**, 255706 (2013).

169. Albrecht, H.-E., Borys, M., Damaschke, N. & Tropea, C. *Laser Doppler and Phase Doppler Measurement Techniques*. *Laser Doppler and Phase Doppler Measurement Techniques* (2003). doi:10.1007/978-3-662-05165-8.

170. Paolino, P., Aguilar Sandoval, F. A. & Bellon, L. Quadrature phase interferometer for high resolution force spectroscopy. *Review of Scientific Instruments* **84**, 95001 (2013).

171. Gates, R. S. *Certification of Standard Reference Material® 3461 Reference Cantilevers for AFM Spring Constant Calibration*. https://doi.org/10.6028/NIST.SP.260-227 (2022) doi:10.6028/NIST.SP.260-227.

172. Pratt, J. R. & Kramar, J. A. SI realization of small forces using an electrostatic force balance. in *18th IMEKO World Congress 2006: Metrology for a Sustainable Development* vol. 1 407–412 (2006).

173. Dohn, S., Svendsen, W., Boisen, A. & Hansen, O. Mass and position determination of attached particles on cantilever based mass sensors. *Review of Scientific Instruments* **78**, 103303 (2007).

174. Warmack, R. J., Zheng, X. Y., Thundat, T. & Allison, D. P. Friction effects in the deflection of atomic force microscope cantilevers. *Review of Scientific Instruments* **65**, 394–399 (1994).

175. Chen, B. Y., Yeh, M. K. & Tai, N. H. Accuracy of the spring constant of atomic force microscopy cantilevers by finite element method. *Anal Chem* **79**, 1333–1338 (2007).

176. Espinoza-Beltrán, F. J. *et al.* Simulation of vibrational resonances of stiff AFM cantilevers by finite element methods. *New J Phys* **11**, (2009).

177. Kueng, W., Silber, E. & Eppenberger, U. Quantification of cells cultured on 96-well plates. *Anal Biochem* **182**, 16–19 (1989).

178. Lityńska, A., Przybyło, M., Pocheć, E. & Laidler, P. Adhesion properties of human bladder cell lines with extracellular matrix components: The role of integrins and glycosylation. *Acta Biochim Pol* **49**, 643–650 (2002).

179. Laidler, P. *et al.* Expression of β1-integrins and N-cadherin in bladder cancer and melanoma cell lines. *Acta Biochim Pol* **47**, 1159–1170 (2000).

180. Mierke, C. T., Frey, B., Fellner, M., Herrmann, M. & Fabry, B. Integrin α5β1 facilitates cancer cell invasion through enhanced contractile forces. *J Cell Sci* **124**, 369–383 (2011).

181. Abidine, Y., Laurent, V. M., Michel, R., Duperray, A. & Verdier, C. Local mechanical properties of bladder cancer cells measured by AFM as a signature of metastatic potential. *Eur Phys J Plus* **130**, 202 (2015).

182. Taubenberger, A. *et al.* Revealing early steps of α2β1 integrin-mediated adhesion to collagen type I by using single-cell force spectroscopy. *Mol Biol Cell* **18**, 1634–1644 (2007).

183. Attieh, Y. *et al.* Cancer-associated fibroblasts lead tumor invasion through integrin-β3–dependent fibronectin assembly. *Journal of Cell Biology* **216**, 3509–3520 (2017).

184. Erdogan, B. *et al.* Cancer-associated fibroblasts promote directional cancer cell migration by aligning fibronectin. *Journal of Cell Biology* **216**, 3799–3816 (2017).

185. Mould, A. P., Akiyama, S. K. & Humphries, M. J. Regulation of integrin α5β1-fibronectin interactions by divalent cations. Evidence for distinct classes of binding sites for Mn2+, Mg2+,and Ca2+. *Journal of Biological Chemistry* **270**, 26270–26277 (1995).

186. Hynes, R. O. The extracellular matrix: Not just pretty fibrils. *Science (1979)* **326**, 1216–1219 (2009).

187. Engvall, E. & Perlmann, P. Enzyme-linked immunosorbent assay (ELISA) quantitative assay of immunoglobulin G. *Immunochemistry* **8**, 871–874 (1971).

188. Pan, S. *et al.* Mass spectrometry based targeted protein quantification: Methods and applications. *J Proteome Res* **8**, 787–797 (2009).

189. Ackermann, B. L. & Berna, M. J. Coupling immunoaffinity techniques with MS for quantitative analysis of low-abundance protein biomarkers. *Expert Rev Proteomics* **4**, 175–186 (2007).

190. Radmacher, M., Fritz, M., Kacher, C. M., Cleveland, J. P. & Hansma, P. K. Measuring the viscoelastic properties of human platelets with the atomic force microscope. *Biophys J* **70**, 556–567 (1996).

191. Carl, P. & Schillers, H. Elasticity measurement of living cells with an atomic force microscope: Data acquisition and processing. *Pflugers Arch* **457**, 551–559 (2008).

192. M, L. *et al.* Standardisation of AFM-based elasticity measurements on living cells - In preparation.

193. Leckband, D. & Israelachvili, J. Intermolecular forces in biology. *Q Rev Biophys* **34**, 105–267 (2001).

194. Giroldi, L. A., Bringuier, P.-P., Shimazui, T., Jansen, K. & Schalken, J. A. Changes in cadherins-catenin complexes in the progression of human bladder carcinoma. *J. Cancer* **82**, 70–76 (1999).

195. Viji Babu, P. K., Mirastschijski, U., Belge, G. & Radmacher, M. Homophilic and heterophilic cadherin bond rupture forces in homo- or hetero-cellular systems measured by AFM-based single-cell force spectroscopy. *European Biophysics Journal* **1**, 3 (2021).

196. Baumgartner, W. *et al.* Cadherin interaction probed by atomic force microscopy. *Proc Natl Acad Sci U S A* **97**, 4005–4010 (2000).